NUMERICAL INVESTIGATION OF COMBUSTION AND OXIDATION IN A STEEL REHEAT FURNACE

by

Bethany M. L. Worl

A Thesis

Submitted to the Faculty of Purdue University

In Partial Fulfillment of the Requirements for the degree of

Master of Science in Mechanical Engineering

Department of Mechanical and Civil Engineering

Hammond, Indiana

December 2019

THE PURDUE UNIVERSITY GRADUATE SCHOOL
STATEMENT OF COMMITTEE APPROVAL

Dr. Chenn Q. Zhou, Chair

Department of Mechanical and Civil Engineering

Dr. Harvey Abramowitz

Department of Mechanical and Civil Engineering

Dr. Xiuling Wang

Department of Mechanical and Civil Engineering

Approved by:

Dr. Chenn Q. Zhou

To my grandmother and grandfather

ACKNOWLEDGMENTS

I would like to acknowledge the Center for Innovation through Visualization and Simulation (CIVS) and the Steel Manufacturing Simulation and Visualization Consortium (SMSVC) for the opportunities and the knowledge provided throughout my work done in collaboration with both groups.

I would also like to thank my committee members for their guidance and feedback that allowed my thesis to develop into that which you see before you. Professors Chenn Zhou, Harvey Abramowitz, and Xiuling Wang were invaluable in putting all of this work together in a concise fashion.

I am very grateful for many of my colleagues at CIVS that provided their own form of guidance and motivation to finish this thesis. Wenjie Lui, Matthew Moore, Xiang Lui, Josh Vandenoever, Armin Silaen, Haibo Ma, Tyamo Okosun, Yuchao Chen, Nick Walla, Xipeng Guo, Rongjia Zhu, and many others.

I would also like to acknowledge the project technical committee that helped to guide the project in the direction it has taken. Kelly Tian from Praxair and Kurt Johnson from ArcelorMittal R&D were invaluable allies in this endeavor and allowed for an industrial perspective in a strongly academic environment.

TABLE OF CONTENTS

LIST OF TABLES

LIST OF FIGURES

NOMENCLATURE

A	Unit area [cm^2]
a	Absorption coefficient [1/m]
a_o'	Oxygen activity at the alloy/scale boundary
a_o''	Oxygen activity at the scale/oxidant boundary
a_s	Characteristic strain rate [1/s]
C_{O_2}	Molar concentration of oxygen [mol/cm^3]
c_p	Specific heat with constant pressure [J/kg-K]
D	Representative diffusion coefficient [cm^2/s]
$D_{Fe^{2+}}^*$	Iron self-diffusion coefficient [cm^2/s]
D_{O_2}	Binary diffusion coefficient of oxygen [cm^2/s]
D_M	Diffusion coefficient [cm^2/s]
D_M°	Metal diffusion coefficient at a unity partial pressure of oxygen [cm^2/s]
d	Scale thickness [cm]
E	Elastic modulus or Young's modulus [Pa]
E_e	Energy [J]
$erfc^{-1}$	Inverse complementary error function
f	Mixture fraction
$\overline{f'^2}$	Mixture fraction variance
$\Delta G°$	Gibbs free energy [J/mol]
G_b	Generation of turbulence kinetic energy due to buoyancy
G_k	Generation of turbulence kinetic energy from the mean velocity gradients
$\vec{g}$	Gravity of Earth (m/s^2)
H	Total enthalpy [J]
$\overline{H}$	Partial molar quantity for enthalpy of mixing [J/mol]
$\overline{H_d}$	Density-averaged enthalpy [J]
h	Specific enthalpy [J/kg]
I	Unit tensor
I_{rad}	Radiation intensity [W/sr]

$\vec{J}$	Diffusion flux [mol/cm^2-s]
K	Phase boundary reaction rate constants [g/cm^2-s-Pa]
K_p	Equilibrium constant
k_{th}	Thermal conductivity [W/m-K]
k	Turbulent kinetic energy [m^2/s^2]
$k_{c,l}$ or k_l	Linear rate constant [g/cm^2-s or cm/s]
$k_{c,p}$ or k_p	Parabolic rate constant [g^2/cm^4-s or cm^2/s]
l	Effective length [cm]
M	Molecular weight (g/mol)
m	Constant for the charge of the vacancies
Δm	Weight gain [g]
N	Molar fraction
n	Refractive index
p_A or P_A	Partial pressure of composition component A [Pa]
$p(f)$	Probability density function (PDF)
$q_s^{"}$	Surface heat flux [W/m^2 or W]
R	Universal gas constant [J/mol-K]
Re	Reynolds number
r	Thickness fraction of an oxide of a balanced oxide system
$\vec{r}$	Position vector
$\overline{S^{XS}}$	Partial molar excess entropy [J/K-mol]
Sc	Schmidt number
S_h	Radiation source terms
s	Path length or ‘pale length
$\vec{s}$	Direction vector
$\vec{s}'$	Scattering direction vector
T	Temperature [K or °C or °F]
t	Time [s]
Δt	Time step or change in time [s]
u_i	Velocity component in the ith direction
$\vec{v}$	Velocity vector

w	Weight fraction of oxygen in the oxide
X or x	Either weight gain per unit area [g/cm^2] or thickness [cm]
Δx	Change in x [cm or g/cm^2]
Y_M	Contribution of fluctuating dilatation in compressible turbulence to overall dissipation rate
Z	Elemental mass fraction
α	Thermal expansion coefficient [1/K]
γ	Deviation from ideal
γ_{FeO/Fe_3O_4}	Iron ion vacancy concentration at the wustite and magnetite boundary
$\gamma_{Fe/FeO}$	Iron ion vacancy concentration at the iron and wustite boundary
γ_0	Fracture energy of the oxide-metal interface (half) [J]
Δ	Change in a value
δ	Deviation from stoichiometry of an oxide, such as $M_{1-\delta}O$
ε_s	Strain
ε_c^s	Critical strain energy [J]
ϵ	Emissivity
ε	Turbulent energy dissipation rate [m^2/s^3]
κ_ϵ	Emissivity weighting factor of a gray gas
μ_{chem}	Chemical potential [J/kg]
μ°	Standard value of chemical potential at arbitrary standard pressure [J/kg]
μ_t	Turbulent viscosity [kg/m-s]
μ	Molecular viscosity [kg/m-s]
v_s	Stoichiometric coefficient
ν	Poisson's ratio
ρ	Density[kg/m^3]
σ	Stefan-Boltzmann constant [W/m^2-K^4]
$\bar{\bar{\tau}}$	Stress tensor
Φ	Phase function
$\overline{\phi}_\iota$	Density-averaged scalar; also the Favre mean scale
χ	Scalar dissipation rate [1/s]
$\Delta\chi$	Defined scalar dissipation step

$\overline{\Omega_{ij}}$	Mean rate-of-rotation tensor
Ω'	Solid Angle
ω_k	Angular velocity of mean rate-of-rotation tensor
$\nabla \cdot$	Divergence
∇	Gradient
∂	Partial derivative
$\sum$	Summation operator

ABSTRACT

The objective of this research was to develop an efficient simulation of an industrial reheating furnace with a flexible scale formation model and to apply the models to study various conditions within an industrial reheating furnace. This work focused on developing a model capable of considering many different key variables that influence scale formation. The scale formation model was incorporated into the computational fluid dynamics (CFD) software ANSYS Fluent © to solve a coupled steady-state and transient simulation. It was also generalized for a low-carbon steel product, so it may not be adequate to cover the effects of alloying metals on the oxidation process. In order to verify the accuracy of these models, baseline cases were simulated and validated against both industrial data and findings from experiments in published literature.

A parametric study with two levels of oxygen enrichment implementation in only the preheat zone was undertaken to study the effects on the heat transfer, scale formation, and fluid flow within the reheat furnace. A medium oxygen enrichment case of 46 vol% oxygen and an oxy-fuel case were used for study. Both oxygen enrichment cases showed largely increased heat transfer to the slab in the preheat zone and increased scale formation. Based on these results, 46 vol% oxygen enrichment is recommended for use in a typical industrial reheat furnace with additional firing rate drawback to reduce scaling and to reduce the chance of overheating the steel slab product.

1. INTRODUCTION

1.1 Reheating Furnaces: Purpose and Background

Steel reheating furnaces are the first step in the process of hot rolling, wherein the steel product (usually slabs) is heated to make the metal more malleable for easier rolling [1]. Higher rolling temperatures require less force to deform the steel but can also lead to equipment damage due to thermal stress. For steel, the temperature used for most grades and furnaces is usually in the range of 1200-1250°C. As shown in Figure 1.1, the iron carbon phase diagram places most of the steel grades of interest within the austenite region, with some higher carbon content steels beginning to liquefy at these temperatures. Reheating also allows alloy precipitates to dissolve back into the bulk of the slab for a more uniform distribution and relieves some casting stresses [1]. The first uses of hot strip mills occurred around 1924, with continuous casting of slabs (the process by which most modern steel is produced) first being accomplished in the 1950s [2].

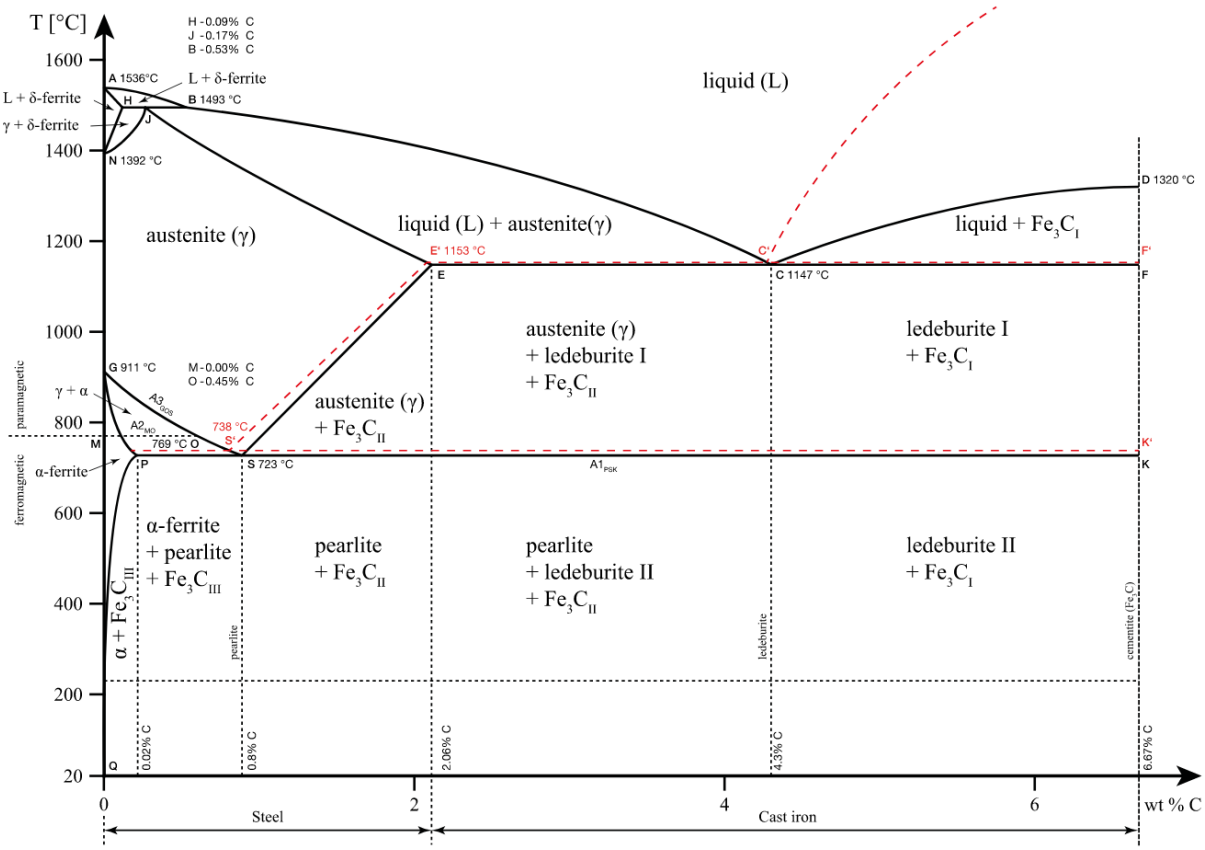

Fig. 1.1 Iron carbon phase diagram [3]

The differing objectives of a given furnace can be at odds with each other. The main goal of the rolling process is to produce a high-quality product, which requires even rolling throughout the hot rolling process. For this to occur, the temperature dependent structural characteristics must be similar throughout the entire slab, which necessitates achieving a nearly homogeneous temperature distribution within the slab. Ancillary goals include minimizing fuel and energy usage and minimizing emissions such as greenhouse gases (GHGs). All of these factors are impacted by the combustion processes, necessitating a closer examination of the mechanisms and phenomena within the reheating furnace.

An example pusher-type reheating furnace configuration is shown in Fig 1.2; fuel is oxidized by air to form a flame which transfers heat to the product through radiation and convection. The walls of the furnace are lined in an insulating material called refractory to minimize heat losses to the environment. Some convection is expected from the hot gases flowing throughout the furnace, but radiative heat transfer is the dominant mode of heat transfer to the product [4-5]. In many furnaces, the combustion products flow counter-current to the direction of slab movement to maximize convective heat transfer. The products of combustion, largely nitrogen, carbon dioxide, and water vapor, leave through the outlet and the charge and discharge doors when they are open. The captured flue gas still contains a lot of energy which is possible to recover.

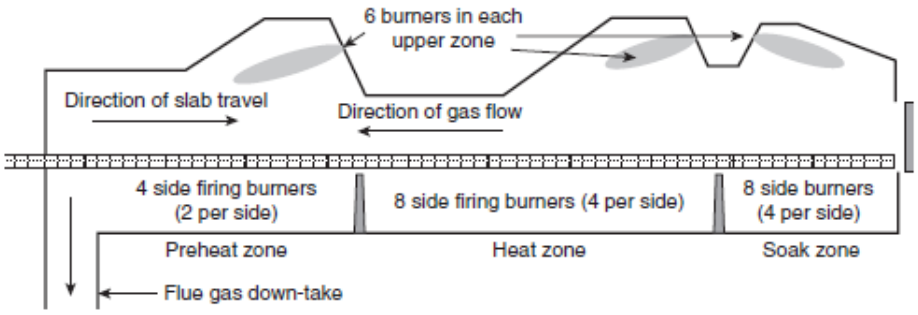

Fig. 1.2 General direct fired furnace configuration [1]

For steel reheating furnaces, two of the most common configurations in use by large rolling mills are classified by the mode of transport for the slab. Pusher-type furnaces move slabs by the semi-continuous charging of subsequent slabs into the furnace [1]. The walking-beam furnace, which is growing in popularity, uses so-called ‘walking-beams’ to lift and advance the slab through the furnace. These walking beams are interspersed with stationary beams, which hold the slabs as

the walking beam resets to its original position. Regardless of the furnace, the slabs are supported by beams or, as they are more commonly known, skids. These skids are typically cooled by internal water flow in order to avoid damage that would require frequent replacement. However, because they are cooled, the skids cause skidmarks on the bottom of the slab due to both conduction heat transfer and via the radiative shielding provided by the skids [4]. This radiative shielding has been found to be the major contributor to the presence of skidmarks [4].

Many furnaces are divided into zones with different purposes [1]. Near the charge door is the preheat zone, wherein the steel product is slowly heated. The heat zone brings the steel product up to the target temperature. The product is then soaked in the soak zone to ensure the target temperature is reached throughout the steel product and achieve the desired temperature uniformity. The slab is then discharged, the primary scale is removed, and the slab is rolled in the rolling mills. The non-firing zone before the preheat zone is sometimes referred to as the convective zone as gases from later zones flow over and begin heat charging slabs. Heat recovery is also possible through recuperative or regenerative processes with the flue gas. The flue gas can be used to raise the temperature of the combustion air in order to increase combustion efficiency and raise the temperature of the flame [1]. This can also realize a fuel savings as higher flame temperatures produce more radiative heat transfer to the product.

The combustion process has many different steps and produces as products carbon monoxide, carbon dioxide, and nitrogen oxides [7]. All of these products are pollutants that must be monitored. Many of these emissions can be controlled by reducing the maximum temperature within the furnace and by ensuring the furnace zones are well-mixed to avoid incomplete combustion. These products also contain oxidants – largely CO_2, H_2O, and excess O_2 – which promote the oxidation of the steel and its alloying elements. This oxidized metal as it is formed in the reheating furnace is called the primary scale and can be several millimeters in thickness, which reduces the total steel yield of the furnace by around 1-2% [8] annually. ‘Mill scale’ and ‘scale’ are also used to refer to the iron oxide formed on steel slabs. Controlling the combustion process is necessary to control both the emissions and the scale formed.

Some common methods of reducing fuel and energy usage for industrial furnaces relate back to the combustion process [1,7]. Increasing the combustion air temperature using recuperative or regenerative processes on the flue gas is one commonly implemented method. Control of the combustion itself is also important; while stoichiometric mixing is the theoretical ideal, turbulent

mixing and dilution requires some excess air, commonly assumed as 10% by industrial rules of thumb [4,9]. Improvement of mixing could reduce the necessary excess air and improve fuel economy. Oxygen enrichment of the combustion air beyond 21 vol% oxygen is also used to improve mixing. In this scenario, the molar fraction of oxygen is increased, replacing nitrogen in the combustion air. Nitrogen can react to form nitrous oxides, but it is simpler to consider a simple combustion reaction:

$$CH_4 + 2(O_2 + 3.76N_2) \rightarrow CO_2 + 2H_2O + 7.52N_2 \quad (1.1)$$

where the nitrogen does not contribute anything to the reaction besides being a diluent. Nitrogen reduces the possibility of oxygen meeting methane and requires energy to be brought from its original temperature to the temperature of the combustion products [10]. As such, any reduction in nitrogen content via oxygen enrichment can increase the flame and gas temperatures within the furnace through basic thermodynamic principles. This is usually accompanied by a reduction in the firing rate of the furnace and an overall fuel savings.

The entire reheating furnace process is quite complex. Implementing operational changes can be costly due to the downtime required and the time required to run any necessary experiments. For example, it can be laborious and expensive to add thermocouples into a slab to study the temperature evolution of slab as they traverse the furnace. As such, many researchers have turned to computational methods to study the reheating furnace and the benefits of various operational changes. While many of the computational methods are simplified models based on empirical work, when adequately validated, these methods can still give an accurate view of the reheating furnace process. Computational methods discretize a given domain into much smaller spatial and temporal elements in order to solve the conservation equations for mass, momentum, and energy, as well as various scalar properties [11]. Computational methods are dependent on the size and resolution of elements in the simulation domain, with finer discretization of the computational domain resulting in a more accurate simulation. The combined sum of these small elements in a given domain are commonly called the mesh.

1.2 Literature Review

Mathematical and numerical modeling of the steel reheating furnace presents multiple advantages over experimental methods, which rely on small-scale trials and large-scale

implementation. A small-scale trial using an experimental furnace cannot always accurately model the effects of the implementation of an operational change in the full furnace. There is also a cost associated with the experiments and implementation that includes material cost, downtime, and testing. The testing phase within the full furnace may require further downtime to remedy any problems and can result in unsatisfactory product. While this downtime may be rolled into regularly scheduled maintenance periods, attempting to make modifications without a full understanding of the potential impacts may result in erroneous implementation and further loss of productivity. For numerical methods, empirical and theoretical knowledge is used to predict the outcome of a given operational change for a given furnace domain. There is an associated cost in the computational demand required to solve multiple 2D or 3D equations simultaneously, but with the inexorable advance of modern computing technology, this computational cost continues to fall [12].

Many of the phenomena within the furnace can now be accurately predicted thanks to a breadth of research on both discrete phenomena, such as turbulence and heat transfer, and modeling of the entire furnace domain. Simplified reactor models such as the well-stirred reactor and the plug-flow reactor have been used to predict the total heat rate and the heat flux to the slabs [6-7,13]. More complex 2D and 3D methods also require the usage of numerical methods to realize the solution of the necessary transport equations in space and in time. While numerical methods, such as computational fluid dynamics (CFD), are more computationally expensive, these methods allow the distribution of all relevant parameters to be solved for.

Hottel et al. modelled the furnace as a well-stirred reactor to study the effect of different radiation models and parameters in 1970 [13]. Under the assumption of the well-stirred reactor model, each zone within the furnace is assumed to have a single, constant temperature and species composition. This method is restrictive in terms of the effect of geometry on mixing, but Hottel et al. was able to confirm that more complex gray-gas radiation models worked quite well compared to simpler radiation models. Li et al. mathematically modelled the reheating furnace with the intention that others would then improve upon it in 1988 [4]. They found that skidmark formation on the bottom of the slab was almost entirely due to the radiative shielding caused by said skids. They recommended variation of skidrail width and height to reduce the skidmark severity. In 1994, Chapman et al. developed a 2D model that utilized more complex turbulence and combustion models than previously used to simulate a reheat furnace [5]. They novelly combined the discrete

ordinates method with the weighted-sum-of-gray-gases method of modeling radiation properties of the furnace gases. Chapman et al. found that 88-93% of the total heat flux to the steel product was from radiative heat transfer, the majority of which came from the hot refractory furnace lining. They also found that most of the energy losses were through flue gases leaving the furnace domain.

A 3D steel reheating furnace was modeled by Kim et al. in 2000 using computational software [6]. This model considered the turbulence, combustion, heat transfer, thermal NOx generation, and three zones within the furnace as a steady-state operation. The furnace was modelled using around 350 thousand cells and a symmetry boundary condition along the axial direction of the furnace. They were also able to study the heat flux to the product in each zone; like the findings from Chapman et al., 94.2% of the total heat transfer into the slab was from radiation. Efficiency was similarly low at 37.7%. Slab heating is a transient phenomenon that requires care in the setup. Yang et al. modelled slab reheating coupled with the 3D flow of gas [14]. The slabs, while all static within the domain, had their temperature information 'jumping' from location to subsequent location until a pseudo-steady state was achieved for the slab temperature distribution. In such a way, they were able to predict the slab temperature distribution throughout the furnace run and at discharge. Huang et al. developed a fully coupled reheat furnace model by considering the movement of the steel as a laminar flow with no reactions or radiation within the furnace [15]. The mesh of the domain used was much larger than that used by Jang et al. at 1.2 million cells.

Notably, the largest differences in computational studies in the 21st century concerns the mesh sizing and the method of coupling the assumed steady furnace phenomena of combustion and fluid flow with the transient slab heating. Mesh sizing is reliant on the size of the domain and on the computational resources available. Various methodologies exist for coupling slab heating with combustion reactions and flow prediction within the furnace. A very direct and correspondingly computationally expensive method is to model the full furnace domain transiently with a dynamic mesh for the slab movement. This dynamic mesh requires remeshing at every time step, which is very costly. Some numerical software has been developed to attempt to address this, such as 'overset' meshing that allows two mesh to coexist in one simulation [16]. These meshing approaches are still relatively new and are relatively unexplored. Some indirect approaches have been discussed above with the review of Yang et al. and of Huang et al. with their information 'jumping' and steel laminar flow approaches respectively [14-15]. Uncoupling the transient slab

heating from the steady furnace model is also possible. Prieler et al. have successfully used this approach along with the common symmetrical furnace domain simplification [17]. 2D furnace simulations and un-coupled 3D simulations are still quite common due to how computationally cheap they both are compared to 3D coupled simulations.

Most of the previous studies on reheating furnaces focused on modeling the combustion between air and a fuel, usually natural gas or coke oven gas. Bisio et al. reviewed the benefits of oxygen enrichment through an exergy analysis and found that there is clear potential for fuel reduction based on the increase in flue temperature and in oxygen enrichment level [18]. They also discussed the economic benefits in relation to oxygen enrichment, such as replacing natural gas with blast furnace or coke oven gas or by increasing the productivity of the furnace. As such, the implementation of oxygen enrichment has been of interest for many researchers. Atreya summarized a report put together for the Department of Energy (DOE) on preheated combustion air systems with oxygen enrichment [19]. The higher temperature flames brought about using oxygen enrichment of the oxidant also increases the NOx thermal generation rate. One objective of this study was to implement oxygen enriched combustion without this increase in NOx formed and with a simultaneous reduction in fuel usage. They attempted this by using various configurations of the oxidant and fuel inlets and differing momentum ratios of the two in order to force entrainment of the furnace gases into the jets before they could meet and fully react. This delayed reaction and elongated reaction zone resulted in homogeneous combustion. The entrainment of furnace gases and the high momentum resulted in efficient mixing and increased the residence time of the NOx formed, allowing it to ‘reburn.’ Lowe et al. also investigated the benefits of ‘oxy-firing’ on carbon capture; removing the nitrogen results in less overall flow leaving the furnace with a much different composition [20]. This composition is largely water vapor, which can be condensed to quickly recover the carbon dioxide in the product gases. Iron oxidation under air-fired combustion and oxygen enriched combustion was experimentally studied by Sobotka et al. [21]. The increase in temperature was also found to increase the predicted scale formation, especially for 100% oxy-fuel combustion. Applying these principles within an industrial environment can prove difficult due to the competing effects in beneficial and detrimental phenomena. To further investigate the implementation of oxygen enrichment, computational fluid dynamics was utilized by various researchers.

Karimi and Saidi modelled oxygen enrichment within a 2D pusher type reheating furnace in 2010 [22]. They found that the furnace efficiency and production increased with the use of oxygen enriched combustion while reducing energy consumption per ton of steel and NOx production rates. This was mainly attributed to the higher flame temperature and corresponding increase in the heat flux to the steel product along with the reduced nitrogen in the product gases. A recommendation of oxygen enriched combustion levels between 21-45 vol% was given by the authors. Alvarez studied the differences in NO_x generation in oxy-coal combustion in an entrained flow reactor simulation with air and O_2/CO_2 environments [23]. Increasing the level of oxygen enrichment was found to consistently predict more NO_x formation than found in scenarios with 21% O_2 by volume. Recently, Mayr et al. investigated the performance increase of using oxy-fuel burners for a pusher type furnace in 2017 [24]. Using oxy-fuel burners instead of air-fuel burners resulted in a productivity increase of 13% and a simultaneous increase in efficiency from 62.9% to 65%.

Jang et al. investigated the impact of scale formation on the slab heating in a walking-beam reheating furnace using an iterative, tridiagonal matrix algorithm (TDMA) model for transient slab reheating [25]. Scale formation was modelled with a parabolic growth rate equation and a parabolic rate constant provided by Chen and Yuen for iron oxidation [26]. They found that scale formation inside of the reheating furnace was low in the preheat zone and thicker on the top than it was on the bottom. Slab heating with and without the scale formation model showed that the scale formation reduced the final slab temperature by 10°C. Schluckner et al. developed a scale formation model based around the experimental work done by Sobotka et al. on scale formation on various steel alloys in air-fired combustion and in oxygen enriched combustion [21,27]. Schluckner et al. used linear and parabolic equations for the mass gain per unit area, $\left(\frac{\Delta m}{A}\right)$ in $\frac{g}{cm^2}$, of scale on steel in the forms of:

$$\left(\frac{\Delta m}{A}\right) = k_{c,l} t [O_2]^a [H_2O]^b \tag{1.2}$$

and

$$\left(\frac{\Delta m}{A}\right)^2 = k_{c,p} t [O_2]^a [H_2O]^b \tag{1.3}$$

respectively. The rate constants, $k_{c,p}$ in $\left(\frac{g}{cm^2}\right)^2 \left(\frac{1}{s}\right)$ and $k_{c,l}$ in $\frac{g}{cm^2}\left(\frac{1}{s}\right)$ were determined empirically via the experimental data provided by Sobotka et al. and through the Arrhenius

function. The constants *a* and *b* were fitted rate exponents to allow for usage in different combustion environments. Landfahrer et al. applied this model to a CFD simulation of an air-fired combustion rotary hearth furnace and found a deviation between measured values and those predicted within the simulation of less than 4% [28]. Scale formation is shown to be consistently quite small at the beginning of the heating cycle, with rate of scale growth increasing substantially in later zones.

1.3 Objectives

The objective of this research was to develop an efficient simulation of an industrial reheating furnace with a flexible scale formation model and to apply the models to study various conditions within an industrial reheating furnace. An efficient simulation pertains to the methodology and the physics models used and their computational cost. Keeping computational cost down without sacrificing accuracy is a key goal for quickly generating results that are applicable to real-world problems. As previously discussed in the literature review, there are various combinations of modeling assumptions that impact the simulation, such as the coupling of transient slab heating and of the steady fluid flow and combustion, and the specific sub-models chosen for phenomena such as turbulence and combustion. Computational cost is usually a function of the size of the mesh and the number of equations which need to be solved for each iteration, the latter of which is itself dependent on the choice of models such as the species transport or combustion model.

A flexible scale formation model aims to combine theoretical oxidation work with the wealth of information generated by numerical analysis. This work focused on developing a model capable of considering many different key variables that influence scale formation, unlike other scale formation models which are often limited to dependence on temperature only. In this vein, an in-depth review of scale formation theory is presented in Chapter 2, alongside the methodology and development of the scale formation model applied in this research.

In order to verify the accuracy of these models, baseline cases were simulated and validated against both industrial data and findings from experiments in published literature. These two models (the steady state fluid flow, combustion, & heat transfer model and the scale formation model) have been integrated to study the impact of oxygen enrichment at mid-level enrichment

(46 vol% O_2) and during oxy-fuel operation (100 vol% O_2) on the combustion phenomena, flow patterns, slab heating, and scale formation inside an industrial reheating furnace.

2. SCALE FORMATION MODELING

Slabs in the furnace are heated up to around 1250°C for long durations of time (1-2 hours). The scale formed here results in a total volume loss of 1-2% of the total steel yield [8,30]. Furthermore, it may spall off within the furnace and require downtime to be cleared out. As such, analysis and prediction of oxidation for various metals, alloys, and environments has continued to be an area of interest for researchers. Most operating hot strip mills are covered in a fine layer of iron oxide powder. After the heated steel slab leaves the furnace, it is subjected to a multi-step process that will substantially decrease its thickness and expose it to atmospheric air [8,26,29]. The first of these steps is a water de-scaler that ruptures the primary scale from the reheat furnace by quenching it and forcing it off. After the water de-scaler, the slab runs through the roughing mill, which decreases the slab size. After each of the roughing rolls, the slab is also de-scaled from the secondary scale formed. After running through the finishing mill, the now very thin 'slab' is coiled and set to cool. The coil will then form tertiary scale. The largest scaling occurs in the reheat furnace, so the largest loss of steel yield due to scaling occurs in the reheating furnace.

Oxidation is a very complex metallurgical phenomenon that has a large impact on high-temperature processes that utilize metals that can be oxidized, such as steel, iron, and nickel. As most of these processes cannot be minutely controlled, there is usually an abundance of oxidizing and carburizing species. As such, metal is consumed in order to form various oxides, which can constitute a loss, and further be detrimental to the efficiency of said high-temperature process. The example in study is that of steel being reheated within a furnace at the beginning of the hot rolling process.

Oxide formation is dependent on various factors, such as substrate composition, gaseous environment, temperature, and type of oxides formed. To study oxidation, thermodynamics and kinetics must be both be considered. Thermodynamics determines what reactions are possible in a given system, whereas kinetics gives information about how fast reactions will proceed. Both alone give access to various insights that have helped to open the veil behind oxidation.

In this chapter, a review of the basic thermodynamic and kinetic principles is explored along with a simplified scale formation model. As oxidation is affected by the composition of the substrate, a review of the effect various alloying materials commonly used in commercial steels is

also undertaken. Finally, stresses induced by the formation of oxides and the heating of the oxide in the furnace are briefly covered.

2.1 Theoretical Analysis

Thermodynamic study of a system of a metal undergoing oxidation can answer many potent questions. The first is of the oxidation reaction itself – will an oxide form in the given environment? Consider a reaction of the following form:

$$M + \frac{1}{2}O_2 = MO \tag{2.1}$$

where *M* is the reacting metal and *MO* is the resulting oxide. At equilibrium in an isobaric, isothermal system, the Gibbs free energy, the measure of the system's stability, will be at a minimum. The Gibbs free energy is a measure of the molar amount of the system components along with the chemical potential of each component. The Gibbs equations shows the necessary condition for equilibrium based on these principles as:

$$\sum_i \mu_{chem,i} v_{s,i} = 0 \tag{2.2}$$

where $v_{s,i}$ refers to the stoichiometric coefficient of a component, $\underline{i}$, in the reaction and $\mu_{chem,i}$ refers to the chemical potential of each component. A derivation up to this point is provided in depth by Young [31], whom also goes into much more depth into the thermodynamic treatment found here. The chemical activity can be calculated as a function of temperature, pressure, and composition as:

$$\mu_{chem} = \mu^\circ{}_{chem} + RTln\left(\frac{p_A}{p_A^\circ}\right) \tag{2.3}$$

where the standard value of the chemical potential at an arbitrary value of p_A° is given by $\mu^\circ{}_{chem}$. p_A itself is the partial pressure of composition component *A*. *T* is absolute temperature and *R* is the gas constant. Assuming pure, immiscible solids whose chemical potential do not depend on pressure, the following relation is obtained:

$$\mu_{chem,MO} - \mu_{chem,M} - \frac{1}{2}\mu^\circ_{chem,O_2} - \frac{1}{2}RTlnp_{O_2} = 0 \tag{2.4}$$

or

$$\Delta G^\circ = \mu^\circ_{chem,MO} - \mu^\circ_{chem,M} - \frac{1}{2}\mu^\circ_{chem,O_2} = \frac{1}{2}RTlnp_{O_2} \tag{2.5}$$

where $\Delta G°$is the Gibbs free energy of the reaction. A reaction will proceed to the right for a given reaction if the Gibbs free energy is found to be a negative value. The partial pressure found where the Gibbs free energy is 0 is called the dissociation pressure. In terms of the partial pressures of all the components of the system, an equilibrium constant, K_p, can then be formulated as:

$$K_p = \exp\left(\frac{\Delta G°}{RT}\right) = \frac{p_{MO}}{p_M p_{O_2}^{\frac{1}{2}}} = \frac{1}{p_{O_2}^{\frac{1}{2}}} \tag{2.6}$$

which incorporates the partial pressures of all the components. Due to the assumption of a pure, immiscible solid, we can set the partial pressure of the solids to unity. The Gibbs free energy has long been studied and the values necessary to calculate the equilibrium constant are easily found. A recommended reference for tabulated values of Gibbs free energy and other necessary thermochemical variables used in this study has been compiled by Kubachewski and Alcock [32].

This analysis allows one to determine if an oxide can thermodynamically form. However, even with pure metals, there exists the potential to form multiple oxides. Adding alloying elements complicates the prediction further and can breakdown some of the previous assumptions as the solubility of alloying elements in oxides becomes important. Iron is thermodynamically able to form 3 oxides above 570°C – wüstite (FeO), hematite (Fe_2O_3), and magnetite (Fe_3O_4) [30,32]. In order to determine which oxide will form under a given oxygen partial pressure, a competitive reaction must be thermodynamically analyzed to ascertain the more stable oxide. In the case of alloys, there is also competition between an oxide and a spinel. An example would be chromium, which can oxidize into chromia (Cr_2O_3) and $FeCr_2O_4$, a chromium-rich spinel.

Regarding reactions between multiple solids, the enthalpy and entropy of the mixture need to be considered. Excess functions that describe the deviation from an ideal solution can be used through the derived function:

$$RTln\gamma_i = \overline{H_i} - T\overline{S^{XS}} \tag{2.7}$$

where $\gamma_i$is the deviation from ideality of a component, i, that can be used in Henry's law ($a_i = \gamma_i N_i$) to find the molar fraction of the component, N_i. $\overline{H_i}$ is the partial molar quantity for the enthalpy of mixing and $\overline{S^{XS}}$ is the partial molar excess entropy. These values have also been tabulated by Kubachewski and Alcock for binary alloys [32].

Thermodynamic analysis such as the above can then help to determine the stability of a reaction along with the result of competitive reactions between multiple oxides or an oxide and a

spinel. Through these relations, the required surface values to selectively oxidize a component of an alloy can be calculated. Maintaining these surface values is a matter of diffusion from the bulk of the substrate metal or alloy system and the rate of scaling of the oxide.

Oxidation is largely controlled by diffusion kinetics, which differ greatly from thermodynamics. Consider a Fe-M alloy system where the M metal will preferentially oxidize. If M is consuming all the oxidant, then the iron is not oxidizing. As such, the M will diffuse out of the alloy to form the M oxide. Even if the bulk is large enough to continuously supply the surface with M alloying element, the diffusion from the bulk to the surface may be so slow as to cause the formation of a zone depleted in M and enriched with iron. As such, the thermodynamic analysis only applies at the boundaries between the phases of the multiple oxides, the alloy, and the oxidant. Young split his analysis into alloy-controlled diffusion, wherein this depletion zone occurs and diffusion in the alloy is rate controlling, and scale-controlled diffusion, wherein the diffusion of metal cations through the scale is the rate controlling step [31]. The phrase ‘rate controlling,’ of course, refers to the fact that every process has one reaction step that is the slowest and is thus the limiting, or rate controlling, step in the entire process. These limiting steps can switch depending on numerous factors in the system.

Famously, Wagner developed a treatment for oxidation modeling and prediction through an analysis of lattice diffusion [33]. The lattice diffusion of ions is dependent on the defect or vacancy concentration within the scale. Higher defects or vacancies means there are more spaces for a cation to diffuse to, which increases the rate of oxidation by increasing the supply of the reactants for the oxidation reaction.

Wagner’s theory is subject to many assumptions. For an analysis of diffusion based purely on lattice diffusion, the scale must be dense and contain very few pores and cannot spall off the metal. Grain boundary diffusion must not contribute much to the oxidation process, and dislocations or cracks are also not considered. The two possible lattice diffusion paths are of metal cations outward and of oxygen anions inward. If metal diffuses outward through the existing scale, the scale will grow away from the metal surface; if oxygen diffuses inward, the metal surface will recede and be replaced by oxide.

Wagner derived a form for the growth of scale as related to the diffusive flux through it as [33]:

$$k_p = \int_{a_o''}^{a_o'} \frac{1}{1-\delta} D_M d(ln a_o) = (m+1) D_M^{\circ} P_{O_2}^{\frac{1}{2}(m+1)} \quad (2.8)$$

where k_p is the rate constant for the growth in scale thickness with units of $\frac{g}{cm^2 s}$. The oxygen activity at the boundaries of the oxide is defined by a_o, wherein the ‘ and “ subscripts refer to the alloy/scale and scale/oxidant boundaries respectively. D is the diffusion coefficient, and δ is the deviation from stoichiometry of the oxide, such as for $M_{1-\delta}O$. D_M° is the metal diffusion coefficient at a unity partial pressure of oxygen. The term ‘m’ is determined by the charge of the vacancies (i.e. m=1 for doubly charged vacancies) [34]. Again, this derivation has been covered in full by a few different authors [31-32, 35], as well as in the original paper by Wagner [33].

Diffusion is only the limiting step of the oxidation process if the alloy/oxide and oxide/oxidant boundaries are at equilibrium. If the oxidant is restricted, then gas phase transport is in control of the oxidation process. The phase boundary reactions between the various phases may also be the rate limiting step. In these cases, the rate constant is very much dependent on the atmospheric composition of the system. Additionally, grain boundary diffusion may also be important for various possible alloy oxides.

These diffusion processes are commonly described by simplified rate equations with the system defined by a singular constant k_x. At high temperatures for isothermal experiments, these constants are usually found to follow a parabolic or a linear rate law. Parabolic rate laws are associated with diffusion processes, while linear rates are associated with gas phase transport and boundary reactions [31, 36-37]. For oxidation, these rate laws can be described by weight gain per unit area via a Pilling-Bedworth-type equation or by the scale thickness via the Tammann-type equation [8, 38-40]. For linear and parabolic oxidation respectively, there is:

$$X = k_l t \quad (2.9)$$

and

$$X^2 = k_p t \quad (2.10)$$

where k_l and k_p are the respective linear and parabolic rate constants, t is time, and X can be either weight gain per unit area (W/A) or thickness. In literature, these are easy to distinguish based on the units of the rate constants.

2.2 Literature Review: Iron and Steel Oxidation

The study of oxidation is quite extensive in terms of experimental studies and analytical investigations. The reheat furnace deals with high temperature, oxidizing species in contact with a heated metal substrate, which results in an annual loss of total steel yield of around 1-2% [8,30]. The typical scale formed on a steel product in the reheat furnace has a lower thermal conductivity than the steel product and a different emissivity. This leads to a small reduction in the heat transfer to the product. Some scaling is seen as beneficial as scale may encompass defects or casting slivers, which are then removed during de-scaling [41]. 'Sticky' scale may also form and stick to the slab, which causes uneven hot rolling and may result in damage to the rolls due to the difference in mechanical properties between the scale and the slab [8]. The study of iron scaling and steel scaling is of keen interest to many researchers.

Various oxidation studies focus on the material properties of scale. Païdassi discovered the three-layered structure of iron oxides [42]. The iron oxides were found to have nearly constant volume ratios above 593.3°C of 95:4:1 of wüstite (FeO), magnetite (Fe_3O_4), and hematite (Fe_2O_3) respectively. Akiyama et al. explored the temperature dependency of the thermal conductivity of the three iron oxides, which are all much lower than that of most steel grades [43]. Iron oxidation controlled by gas characteristics, typically modelled as linear rates, was found to be controlled by gas phase mass transport instead of surface reactions [44-45]. Iron oxidation as controlled by solid characteristics, typically modelled as parabolic rates, has found that solid state diffusion through the iron and the scale to control the scaling [45-46]. The gas phase mass transport is independent of the steel substrate, and the solid state diffusion is independent of gas properties. Both are highly dependent on temperature. The rate constant that describes the linear rate has also been found to be a summation of the rate constants for all oxidizing species [36-37,47].

The rate constants needed to predict the scale formation are highly dependent on gas atmosphere, substrate composition, temperature of both the solid and the gas, flow velocity, and the pressure. Most of these are because each variable has on the thermodynamic and kinetic phenomena previously discussed. Interactions between unique steel grades and quaternary atmospheres can prove to be somewhat difficult to predict, especially in an industrial structure such as the reheat furnace. Many researchers have focused on the study of the oxidation of a known grade of steel in a controlled laboratory environment. Selenz and Oeters, Sachs and Tuck, Smeltzer, Païdassi and Abuluwefa et al., among others, have all worked on measuring the kinetics of scale

formation on iron and steel in various environments, both isothermal and anisothermal in nature [36-37,42,44]. These kinetic findings are varied in their presentation and are applicable to a small range of conditions.

There is also a time dependence for the rate constants. As the scale builds up initially due to gas phase mass transport, the oxidant can no longer reach the surface, and solid state diffusion will take over [8]. The gas phase mass transport may become locally dominant again if the scale spalls or cracks off of the steel substrate, but solid state diffusion is commonly cited as the main, long-term rate limiting process for iron and steel oxidation [8, 21, 30].

2.3 Scale Formation Modeling

As previously mentioned, oxidation of iron leads to the formation of 3 oxides – wüstite, hematite, and magnetite. In order to check the stability of each oxide and their order between the oxide/metal and oxide/oxidant boundaries, each partial pressure and Gibbs free energy has been calculated based on the data in Table 2.1 provided by Kubachewski and Alcock [32].

Table 2.1 Iron oxide reactions and Gibbs free energy [32]

Reaction	**Gibbs free energy (J/mol O_2)**
$2Fe + O_2 = 2FeO$	$\Delta G° = -529{,}780 + 129T$
$6FeO + O_2 = 2Fe_3O_4$	$\Delta G° = -624{,}420 + 250.2T$
$4Fe_3O_4 + O_2 = 6Fe_2O_3$	$\Delta G° = -498{,}900 + 281.4T$

The stabilities of each oxide have been plotted as a function of temperature from 500 to 1400°C in Fig. 2.1. In this form, it is typically called an Ellingham diagram. The lower range was chosen to be 570°C as wüstite becomes stable at this temperature while the upper range is slightly higher than typical conditions within industrial furnace processes. The more negative the Gibbs free energy of formation, the more stable the oxide. As such, the order of the iron oxides from most to least stable is wüstite, magnetite, and then hematite.

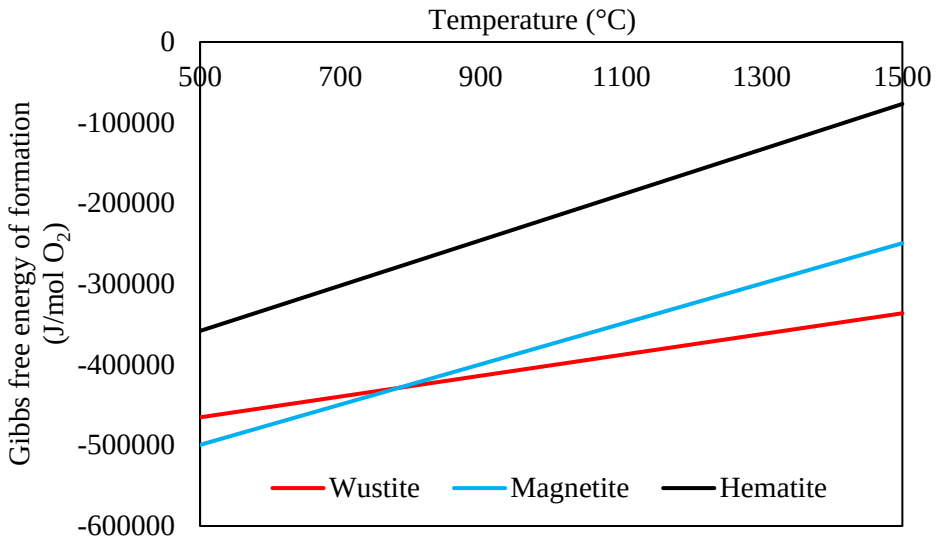

Fig. 2.1 Ellingham diagram of iron oxides in oxygen

When it comes to determining the order of the oxides on the scale, competitive reactions between the various oxides can be used to determine how they might transiently form on the iron surface. The three competitive reactions considered are shown in Table 2.2. Gibbs functions were calculated based on tabulated thermodynamic data for each reaction [32]. The first two reactions consider the case of hematite or magnetite in contact with the surface of the iron. Both Gibbs functions for these reactions give negative values, implies that hematite at the surface would reduce to form magnetite, which would then reduce to form wüstite. This gives the natural conclusion that the order of the oxides from the iron surface is wüstite, magnetite, and then hematite in contact with the gaseous oxidant. The third competitive reaction is a repetition of how hematite is formed in terms of whether magnetite or hematite will equilibrate with the oxygen atmosphere. Again, all values show the reaction will proceed to the right. These results corroborate Païdassi's findings [42].

Table 2.2 Iron oxide competitive reactions and Gibbs functions [32]

Reaction	Gibbs function (J/mol)
$Fe + Fe_3O_4 = 4FeO$	$\Delta G° = -264{,}890 + 65.4T$
$Fe + 4Fe_2O_3 = 3Fe_3O_4$	$\Delta G° = -312{,}210 + 125.1T$
$\frac{2}{3}Fe_3O_4 + \frac{1}{6}O_2 = Fe_2O_3$	$\Delta G° = -83{,}150 + 46.9T$

Looking away from an analytical, thermodynamics approach, the modeling of iron oxidation can be accomplished by considering both the gas phase mass transport and the solid state diffusion phenomena. A serial resistance relation for the linear and parabolic rates can be obtained, which expresses the iron oxidation behavior can be expressed as follows:

$$\frac{1}{k_l}x + \frac{1}{k_p}x^2 = t \tag{2.11}$$

where x is the scale thickness and t is the slab residence time. However, this equation cannot be numerically solved in a transient scenario as the time is discretized into many time steps. The scale thickness should be accumulatively calculated based on the formation in each time step. Therefore, the following method has been derived to solve the previous equation numerically:

$$\frac{\mathrm{dx}}{dt} = \left[\frac{1}{\left(\frac{1}{k_l}\right)^2 + \frac{4t}{k_p}}\right]^{1/2} \tag{2.12a}$$

$$\Delta \mathrm{x} = \frac{\mathrm{dx}}{dt} \cdot \Delta t \tag{2.12b}$$

$$\mathrm{x} = \sum \Delta \mathrm{x} \tag{2.12c}$$

where Δx is the amount of scale formed in each time step, Δt is the time step size, and x is the current scale thickness. These equations are equivalent over a given time.

The rate constants k_p and k_l are based on different properties. The parabolic rate constant formula was derived by Himmel et al. and by Smeltzer and is based mainly on scale properties and phase equilibria [44,48]:

$$k_p = 6\frac{\rho_{FeO}^2 M_O^2}{M_{FeO}^2} \cdot D_{Fe^{2+}}^{*}(\gamma_{FeO/Fe_3O_4} - \gamma_{Fe/FeO}) \tag{2.13}$$

Here, ρ is the density of scale, M is the molecular weight of either oxygen or wüstite, γ signifies the iron ion vacancy concentrations at the boundary specified, and $D^*_{Fe^{2+}}$ is the iron self-diffusion coefficient. Himmel et al. found the iron self-diffusion coefficient to follow the equation $D^*_{Fe^{2+}} = 0.118 \cdot e^{-124{,}300/RT}$ [48]. Deich and Oeters provided tabulated data for iron ion vacancy concentrations at the iron oxidation boundaries [49].

The linear rate constant was derived in three parts using experimental results from Abuluwefa et al., mass transfer principles, and gas properties [36-37]. The linear rate constant is the summation of the rates of all the oxidizing species.

$$k_l = M_o(k_{l,CO_2} + k_{l,H_2O} + k_{l,O_2}) \tag{2.14a}$$

$$k_{l,CO_2} = K_{CO_2}(a^*_O)^{-\frac{2}{3}}(1 - \frac{a^*_O}{a'_O})P_{CO_2} \tag{2.14b}$$

$$k_{l,H_2O} = K_{H_2O}(a^*_O)^{-\frac{2}{3}}(1 - \frac{a^*_O}{a'_O})P_{H_2O} \tag{2.14c}$$

$$k_{l,O_2} = \frac{4}{3}\frac{D_{O_2}}{l} Re^{1/2} Sc^{1/3}(C^G_{O_2} - C^*_{O_2}) \tag{2.14d}$$

Here, M_o is the molecular weight of oxygen, a_o is the oxygen activity of wüstite in equilibrium with iron (a^*_O) and in equilibrium with the gas phase (a'_O), P_i is the partial pressure of the species i, Re is the Reynolds number, Sc is the Schmidt number, D_{O_2} is the binary diffusion coefficient of oxygen, l is the effective length of the sample, C_{O_2} is the molar concentration of oxygen in the gas phase (superscript G) and at the interface (superscript *), and K_{CO_2} and K_{H_2O} are the phase boundary reaction rate constants. Values of the oxygen activity were derived from data tabulated Darken and Gurry [50]. Abuluwefa experimentally found the phase boundary reaction rate constants to be dependent on temperature as $K_{CO_2} = 18{,}490 \cdot e^{-274{,}362/RT}$ and $K_{H_2O} = 28{,}280 \cdot e^{-263{,}555/RT}$ [36].

These formulas will yield rate constants that describe the weight gain per unit area (W/A). In order to convert these from rate of W/A to rate of thickness growth, a conversion factor has been derived by Webler [51]:

$$\frac{\Delta m}{A} = \sum_{i=1}^{n} w_i \rho_i r_i X_i = X_{total} \sum_{i=1}^{n} w_i \rho_i r_i \tag{2.15}$$

where w is the weight fraction of oxygen in the oxide, ρ is the density of the oxide (g/cm^3), r is the thickness fraction of the specific iron oxide out of the entire oxide, and X is the thickness of the oxide in cm. The three properties for the 3 iron oxides are given below in Table 2.3. Due to its high thickness fraction, temperature-dependent properties were used for wüstite for higher accuracy.

Table 2.3 Physical properties for the iron oxides

Iron Oxide	Wüstite	Magnetite	Hematite
Weight Fraction of Oxygen	$\frac{15.999}{15.999 + (((\underbrace{-5E^{-05} * T}_{\text{Average Fe:O ratio in wüstite from [52]}}) + 0.9816) * 55.845)}$	27.64%	30.06%
Density (g/cm^3)	(-0.0001*T) + 5.7467 from [52]	5.18	5.255
Thickness Fraction	95%	4%	1%

2.4 Validation of Scale Formation Model

For details on how the scale formation model was incorporated with the numerical solution from the computational software, see Chapter 3. Validation of the scale formation model requires comparison with experimental work using the same conditions. A transient case was developed to mimic the flow conditions found in the experimental work as most of the key conditions were explicitly given. Some conditions, such as pressure, were assumed. The model was compared against work done by Abuluwefa et al. [36-37]. This work studied low carbon steel under different atmospheres and temperatures; kinetics rate constants were also tabulated. The researchers also studied anisothermal, or nonisothermal, laboratory scaling, which is uncommon in literature. This broad range of data allowed for different types of validation.

The investigation done by Abuluwefa et al. utilized a thermogravimetric analysis (TGA) heated by a tungsten resistor element [36-37]. The furnace was made of a pure alumina tube, which has been simplified for numerical analysis to a cubic domain of edge length 1 meter. The numerical calculation only considers the cells on either side of the surface, so the size of the domain need not be exact with the experimental setup. This domain included an inlet and an outlet wherein hot gases of known composition flowed above a critical velocity.

Based on known operating conditions, four isothermal conditions with different gas temperatures from 1000℃ to 1150℃ were tested to compare the simulation results with experimental results. The scale thickness is represented by scale weight gain per area of sample surface. For each case, the scale weight gain after one hour of heating time is recorded to compare with experimental results, as shown in Figure 16. All cases show good correlation between simulation and experimental results with average errors between 3-5% for the short timescale and conditions prescribed. All rate constants were within the order of magnitude reported in the paper. Care should be taken at lower temperatures when using this model, as lower temperatures may have differing rate controlling steps and thus invalidate many of the assumptions that go into this model.

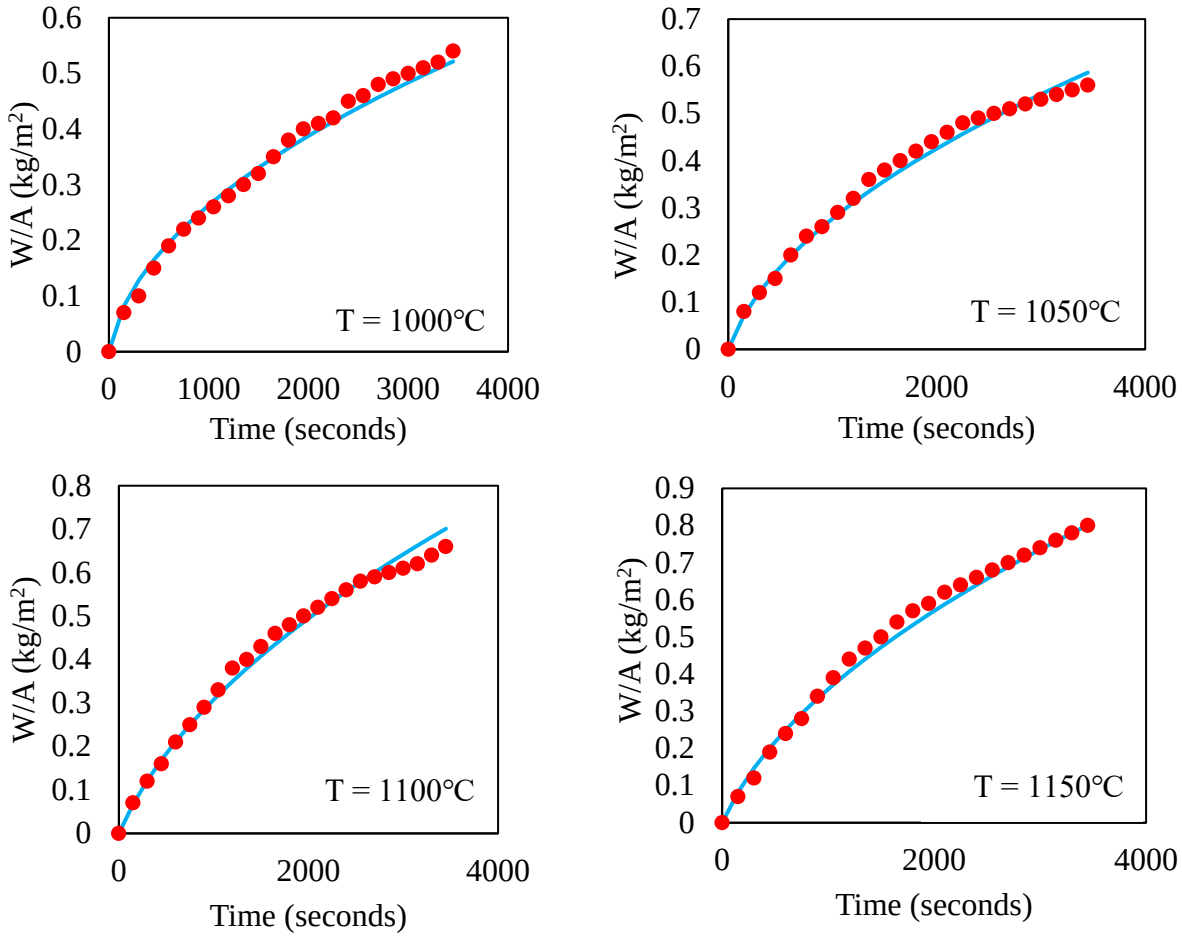

Fig. 2.2 Scale weight gain comparison between simulation (line) and experimental (dots) work for different isothermal gas temperatures as noted.

The effects of CO_2 and H_2O are also investigated and compared with literature for validation purposes. Several cases have been simulated varying CO_2 and H_2O concentrations under an isothermal condition with 1100℃ gas temperature. There is 1% O_2 besides CO_2 or H_2O, and the balance is N_2. The simulation results are compared with experimental results in Fig. 2.3 and 2.4.

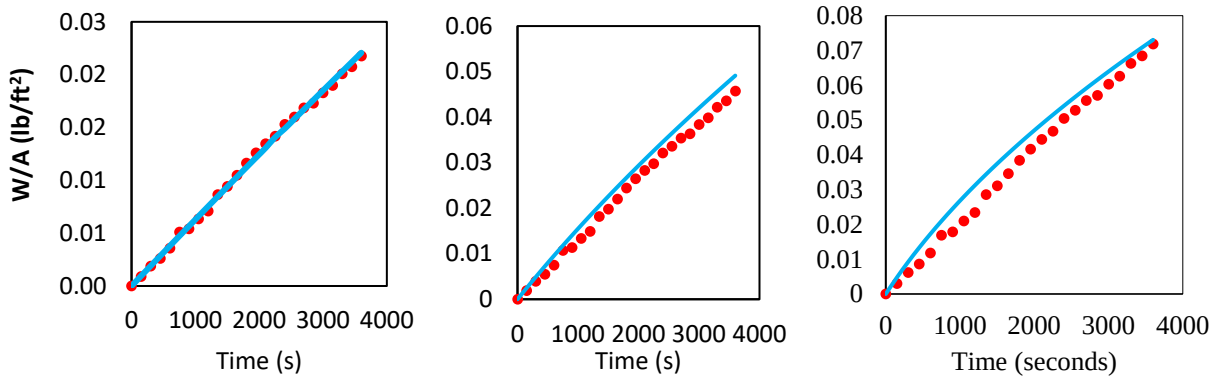

Fig. 2.3 Scale weight gain comparison between simulation (line) and experimental (dots) work for CO_2 concentrations of 7% (left), 10% (middle), and 15% (right).

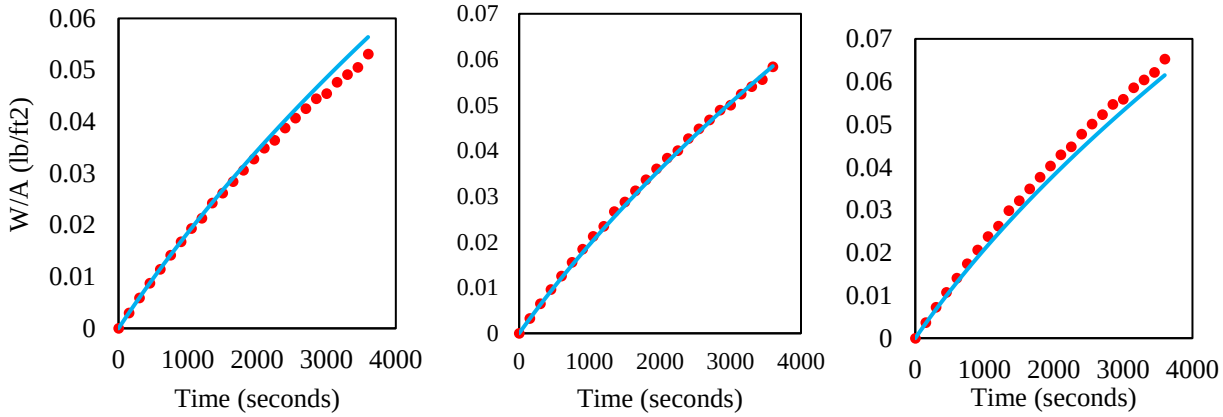

Fig. 2.4 Scale weight gain comparison between simulation (line) and experimental (dots) work for H_2Oconcentrations of 3% (left), 6% (middle), and 10% (right).

The gas composition and temperature vary with position and firing rate within the reheating furnace. Therefore, a comparison between simulation results and real furnace experiments was necessary to validate the scale formation model. According to the real furnace conditions from literature, a case with increasing gas temperature and complex gas atmosphere has been conducted and compared with experimental results. The furnace gas consists of 1% O_2, 10% CO_2, 3% H_2O,

and N_2. Considering both the necessary simplification in simulation and the practical difficulties of measuring all conditions accurately in experimental work, the comparison in Fig. 2.5 shows a fairly acceptable agreement between simulation and experimental results.

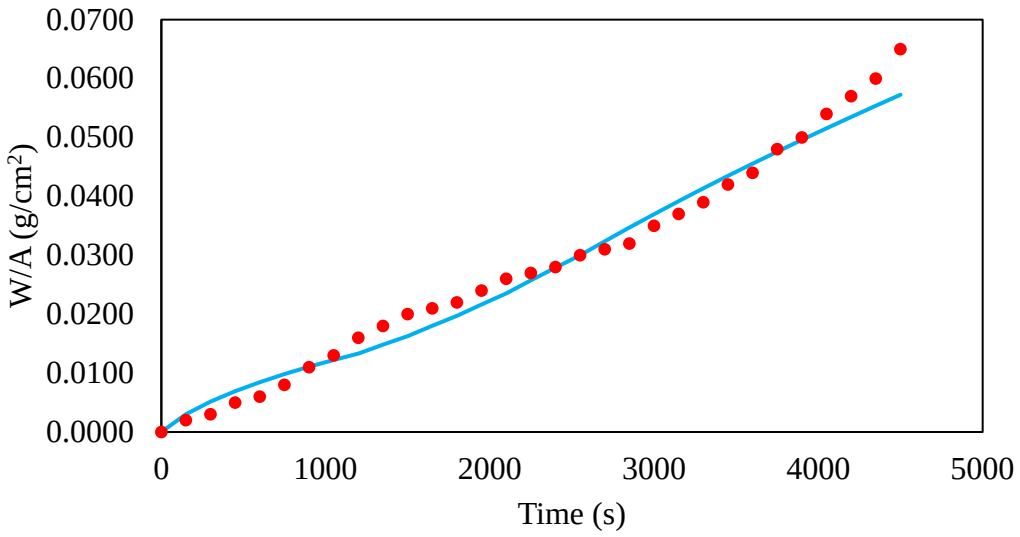

Fig. 2.5. Scale weight gain comparison between simulation (line) and experimental (dots) work under a heating ramp of 9.6°C/min and quaternary atmosphere (1 vol% O_2 – 10 vol% CO_2 – 3 vol% H_2O – N_2 balance)

2.5 Effect of Alloying Components

Many different alloying materials, such as chromium and silicon, can form a protective oxide on the slab surface. This protective oxide inhibits the growth of other oxides and will result in less loss of steel. Other metallurgical phenomena also exist that relates to scale formation, such as copper hot shortness. De-scaling of the slab prior to and throughout hot rolling is also a concern within the steelmaking industry on the finishing end. Binary and ternary phase diagrams give a look into the thermodynamics side of scale formation, but kinetics and diffusion data are also required in order to get the full picture. Most thermodynamics data regarding binary or ternary alloys is referenced from the thermochemical tables of Kubachewski and Alcock [32].

Alloy oxidation prediction requires a complex combination of thermodynamics and kinetics. Protective oxides will cut off the surface from further oxidation and usually have slow kinetics that lead to a relatively small amount of scale growth. Three major alloying elements that react to form protective oxides are silicon, aluminum, and chromium. Each of these elements also

has a spinel oxide form that competes thermodynamically with the protective oxide. Theory allows us to calculate certain critical alloying values that will allow the formation of either the spinel or the oxide depending on the temperature and the atomic fraction of the element [32-33]. The equations for the competitive reaction and the resulting atomic fraction for the main protective oxides are shown in Table 2.4. Necessary thermophysical values were extensively tabulated for binary alloys and oxides by Kubachewski and Alcock [33].

Table 2.4. Competitive reactions and surface atomic fraction

Alloying Element	Competitive Reaction	Surface Alloying Atomic Fraction Needed for Reaction Equilibrium (N_M)	N_M at 1150°C
Chromium (Cr)	$Fe + \frac{4}{3}Cr_2O_3 = FeCr_2O_4 + \frac{2}{3}Cr$	$N_{Cr} = e^{\frac{-110{,}135+31.265 \cdot T}{RT}}$	$3.870 \cdot 10^{-03}$
Silicon (Si)	$2Fe + 2SiO_2 = Fe_2SiO_4 + Si$	$N_{Si} = e^{\frac{-204{,}600+12.19 \cdot T}{RT}}$	$3.059 \cdot 10^{-07}$
Aluminum (Al)	$Fe + \frac{4}{3}Al_2O_3 = FeAl_2O_4 + \frac{2}{3}Al$	$N_{Al} = e^{\frac{-313{,}950+51.645 \cdot T+7.845 \cdot T \cdot \log(T)}{RT}}$	$2.859 \cdot 10^{-08}$

The values for N_M found for 1150°C are quite low. This is attributed to this value only being the *surface* alloying atomic fraction. There is also the concern of diffusion and depletion in the sub-surface region. Formation of an oxide, protective or otherwise, requires that the element be present within the top layers of the material in order to reach and react with the oxidants. In the case of elements that diffuse slowly through the alloy or react out faster than they can replenish at the subsurface alloy region, depletion may occur. Copper hot shortness is cause by such a depletion at the surface and can be seen in Fig. 2.6 [31]. In this case, the iron reacts out quickly, leaving a zone of almost pure copper at the surface. Copper has a melting point of around 1085°C. As this value is lower than those found in the reheating furnace, the copper layer will melt and infiltrate deeply into the grain boundaries of the metal. In the case of protective oxides, the diffusion of the oxidizing element through the alloyed steel must equal or exceed the diffusion of the same element out into the forming oxide to stay protective. If depletion occurs, the oxide will begin to reduce and other, faster oxides may dominate.

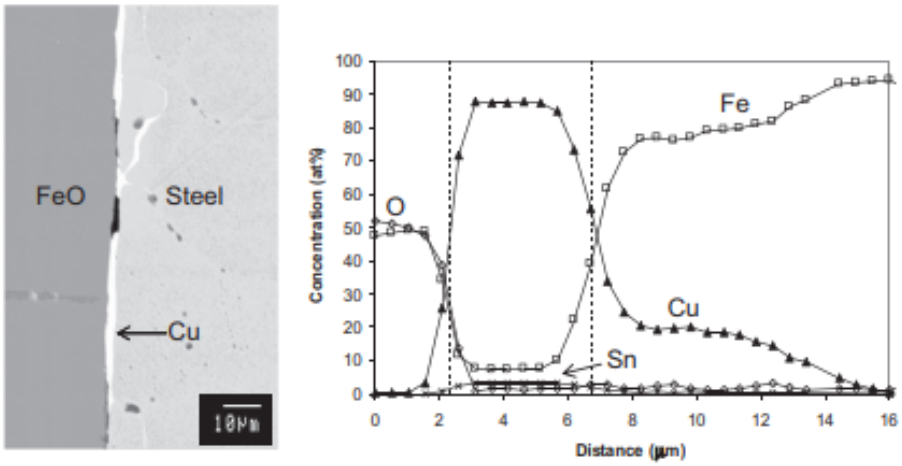

Fig. 2.6. Copper depletion at the alloy surface [31]

Most grades of steel largely consist of the element iron (Fe). Marston et al. reviewed the challenges of modeling oxidation and carburization phenomena [52]; as iron is consumed to form iron oxides, alloying elements incapable of diffusion through the scale may accumulate at the steel/oxide interface. This can change the local thermodynamic and metallurgical properties and even precipitate out pure phases of alloying elements such as copper or nickel. Schütze also mentions that the 'wüstite point,' or the temperature at which wüstite becomes stable can be moved to higher or lower temperatures depending on the dopant used [53]; higher temperatures were found with additions of Mo, Cr, Ni, and V, while lower temperatures were found with additions of Mn.

The most basic 'alloying' element for steel is carbon. Studies have found that for all things constant excluding the amount of carbon, Fe-C alloys scale slower than pure iron alone [56]. Carbon can react with the oxidizing species to form the gaseous carbon monoxide. Carbon monoxide generation in the scale can cause the formation of high-pressure blisters in the scale that can cause both an increase and a decrease in the oxidation rate [8, 26]. If the pressure is great enough, the scale may crack; this would expose the surface of the steel to the oxidizing environment and the local oxidation rate would dramatically increase to 'heal' the crack [8, 53]. If these blisters do not crack, they will then inhibit the diffusion of iron cations through the iron oxide scale and thus decrease the oxidation rate. Carbon, as with many different alloying elements, will also change the defect concentration, which will affect the diffusion. These conclusions, as can be seen in the review done by Chen and Yuen [8] are very situation specific and sometimes misleading.

Nickel is not oxidized at the oxygen partial pressure found at the steel/oxide interface, so enrichment of this element will slow the solid state diffusion of iron cations and then inhibit oxidation. Nickel has also been found to form filaments that bind the scale to the steel and can lead to incomplete descaling [52].

Protective oxides are formed from compact, slow growing scales. Elements used in steel that are known to be able to form protective oxides are chromium, aluminum, and silicon. Silicon can oxidize to silica and then to fayalite, which has a molten, eutectic phase above a temperature of 1177°C, which can act as a fluid barrier or as a bulk flow that promotes mass transfer [52]. Aluminum, along with silicon, are used as deoxidizers for the steel. Aluminum tends to form protective Al_2O_3 scales with increasing aluminum content and with increasing temperature [55]. Both aluminum and chromium are believed to be controlled by grain boundary diffusion processes; growth along the grain boundaries can then lead to lateral cracking and compressive stresses [56-59]. Chromium is commonly used in stainless steels, and quite successfully at that. Cr_2O_3 formed at the surface of the steel may disallow the oxidation of faster growing species of oxides [26, 60].

Copper is of interest due to the molten copper rich phase that occurs when copper is enriched at the surface and subsurface of a steel alloy. As with the fayalite, this phenomenon has potential to increase or decrease the rate of oxidation. When the copper melts, it is referred to as surface hot shortness, or hot short, as previously discussed [51].

Lastly, and most generally, are the elements that give a third element effect or a reactive element effect [31]. The third element is the component of any ternary alloy that may form an oxide with a stability intermediate to the oxides formed by the other two elements. These third elements alter the thermodynamics in the subsurface region of the alloy, even when the element is non-oxidizing. The reactive element effect is when reactive elements help to improve the formation of chromia and alumina and inhibit spallation [31]. These reactive elements enrich at the grain boundaries of the oxide as well as the steel/oxide interface and thus change the transportation properties at those locations [61].

2.6 Oxide Stresses and Spallation

Oxidation causes the formation of oxides on the surface of a metal – these oxides will have different material properties to the steel and will be releasing heat due to the formation and breaking of different molecular bonds. If the oxide is formed due to the transport of cations away

from the metal surface, then the metal substrate may recede from the oxide shell formed. These gaps between the metal and the oxide will eventually cave inward and expose the steel surface to the gas atmosphere anew. As such, various stresses are found within the growing oxide and these can affect the ability of the oxide to stay on the metal. Models and tabulated data pertaining to the breakdown, stress, and spallation of oxide scales were reviewed by Schütze and are reviewed here [53]. Oxide growth stresses can be found through [53]:

$$\sigma_{oxide} = -\frac{E_{oxide}}{1-\nu_{oxide}} \cdot \varepsilon_{s,oxide} \tag{2.16}$$

where E is the elastic modulus, ν is the Poisson's ratio, and ε_s is the strain. Subscripts denote that all these values pertain to the oxide. The strain is a function of the Pilling-Bedworth ratio (PBR) through the equation $\varepsilon_{s,ox} = \omega[(PBR)^{\frac{1}{3}} - 1]$. The PBR is the ratio of the volume of the oxide formed to the volume of the metal consumed. Stresses caused by temperature change are described by [53]:

$$\sigma_{oxide} = \frac{-E_{oxide} \cdot \Delta T \cdot (\alpha_{metal} - \alpha_{oxide})}{\frac{E_{oxide}}{E_{metal}} \cdot \frac{d_{oxide}}{d_{metal}} \cdot (1-\nu_{metal}) + (1-\nu_{oxide})} \cdot \varepsilon_{s,oxide} \tag{2.17}$$

where previous variables hold their values, d is thickness, and α is the thermal expansion coefficient. Subscripts, again, denote whether a property comes from the metal or the oxide.

Oxide spallation is governed by the strain energy; when this energy exceeds the necessary amount for interface fracture, the oxide will spall off the metal. This critical strain energy is described using [53]:

$$\varepsilon_{s,c}^{s} = \sqrt{\frac{2 \cdot \gamma_0}{d \cdot E_{oxide} \cdot (1-\nu)}} \tag{2.18}$$

where $2 \cdot \gamma_0$ is the fracture energy of the oxide-metal interface and d is the scale thickness. Spallation can restart the scale growth process. As the oxidation process is fast during the initial growth of scale, this results in larger amounts of metal lost to scale. This scale will then spall off into the furnace and be carried by the flow until it settles and accumulates at the bottom of the furnace.

Tang et al. studied the flow patterns within the furnace and their relation to the scale accumulation found by industry [62]. Accumulated scale as shown in Fig. 2.7 was found to correspond to regions of reverse flow under the slab. This accumulation was less in regions of

support structures as they disrupted the reverse flow and lessened the scale spallation in these areas. Accumulation also did not occur near the burners due to the high momentum jets that inhibited accumulation.

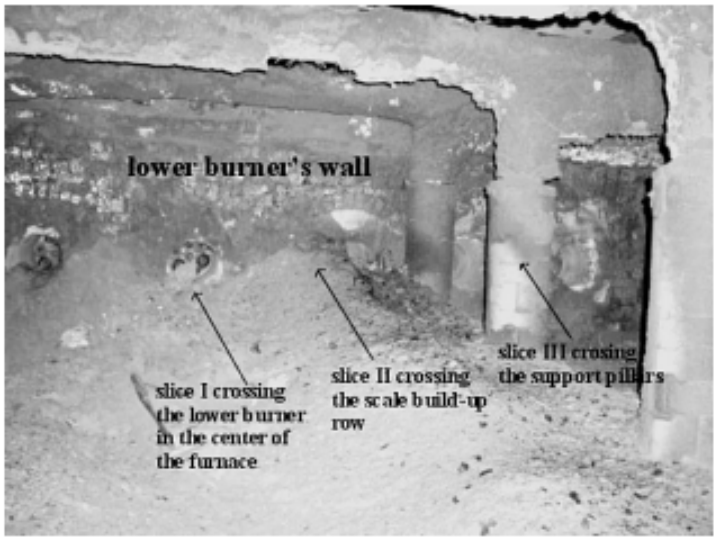

Fig. 2.7. Accumulated scale near the burner outlets of the lower heating zone with support pillars in frame [62]

3. CFD MODELS AND METHODOLOGY

3.1 Methodology

The reheat furnace is modeled here using two coupled simulations following the method detailed by Prieler et al. and now here [17, 24]. These two simulations include a full furnace domain that solves the fluid flow and combustion within the furnace and a single slab domain that solves the transient slab heating. For the former simulation, a slab temperature distribution is assigned. The first iteration of this simulation coupling uses the slab temperature distribution data provided from industrial collaborators. Once this full furnace simulation converges, the heat flux into the slabs can be exported and applied onto the second simulation in order to solve for the transient slab heating. Now, from this simulation, the temperature can be found at each time step and converted back into a function of space to be imported back into the full furnace case as a new boundary condition for slab temperature distribution. As slab heating is largely from radiation, the temperature predicted from the slab heating simulation is relaxed between the initial guess with the predicted value by a factor of 0.5 or more.

In this way, the coupling between a very large furnace case and a small single slab case is accomplished. Each step of this iterative process needs to converge, and the final convergence depends on the temperature profile. Fig. 3.1 details the flow of this methodology. This is an improved methodology compared to the previous methodology used for research purposes.

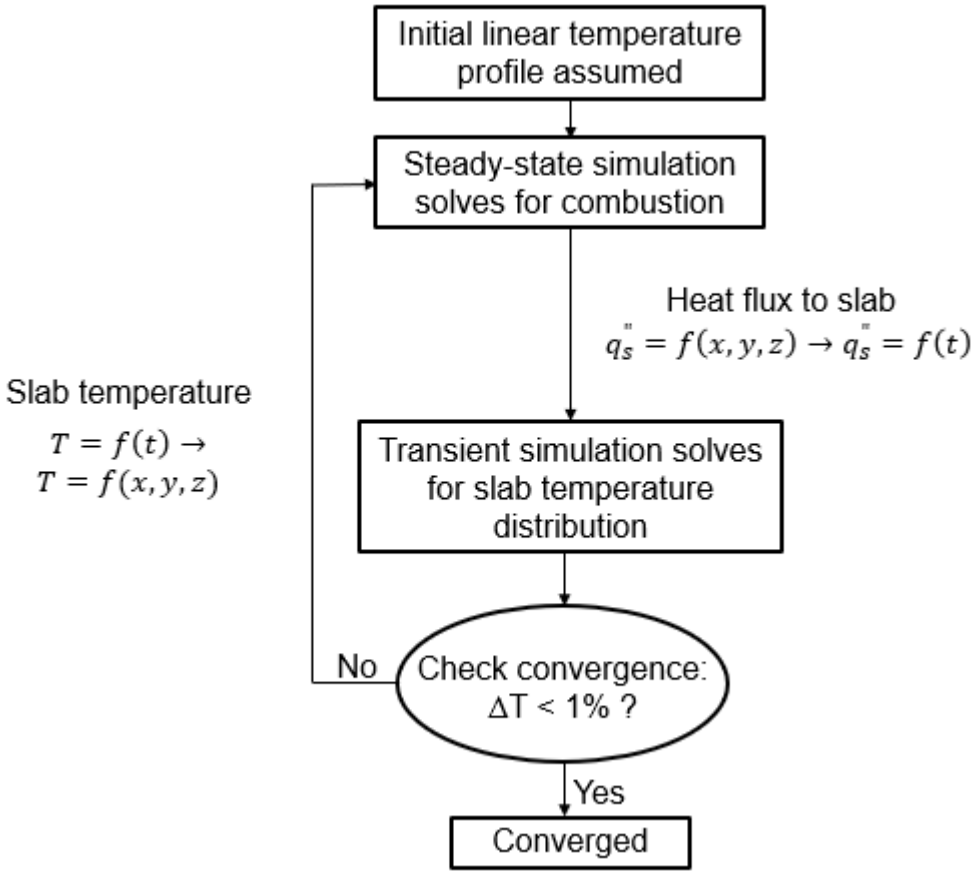

Fig. 3.1 Methodology for a coupled reheat furnace

Previous reheating furnace models utilized by the Center for Innovation through Visualization and Simulation (CIVS) also incorporated a steady-state and a transient simulation setup. However, the steady-state solution was used as an initial condition for the transient case. The transient case solved for slab heating in a transient manner using a dynamic mesh along with the transient flow and combustion. Not only is the dynamic mesh very computationally heavy as it needs to re-mesh at every time step, but the slabs started and ended outside of the furnace. This required a domain extension, which also increased the total number of cells inside the domain. As such, this process was very time and computationally expensive. Solving for the combustion, fluid flow, and heat transfer in the full furnace and solving for the transient slab heating separately requires less computational power than the previous reheating furnace model. It also avoids the usage of a dynamic mesh. Some may argue that the furnace is not a steady-state, continuous process due to delays and transient turbulent structures. However, the steady-state assumption used here uses time-averaged conditions and has been used for analysis successfully in the past [63].

The domain of the current simulation setup was also halved to exploit a symmetry boundary condition. The only change in this choice was the need for a uniform line up of the slabs within the furnace. As only one slab is tracked, this modification from the industrial slab lineup was found acceptable. For the full furnace model, the slab surfaces are modeled to grab the heat flux into said slabs. As such, the assigned boundary condition is the slab surface temperature. These heat fluxes are then applied onto the slab surfaces of the transient heating simulation. Here, the slab slides along the full heat flux profile in mimicry of the movement of the slabs in the actual furnace. Temperature is taken at appropriate intervals and bought back to the full furnace model, again, as a boundary condition.

The scale formation model utilizes conditions from both simulations. Calculations are split between the gas-side of the slab surface boundary and the solid side as there are variables found from both sides. This is accomplished using user-defined scalars and user-defined memory provided within ANSYS Fluent with all calculations described throughout the work occurring within a user-defined function (UDF). As the scale thickness changes during the simulation, the actual geometry of scale is neglected to simplify the problem.

During the reheating process, an oxide layer forms on the free surface of slabs, and this oxide layer has a higher thermal resistance than steel. Due to this higher resistance, there will be a noticeable difference between the temperature of a slab with scale and that of a slab without scale. Since the heat flux from gas to slabs must equal to the conduction heat flux through the surface into the internal part of slabs, the problem can be simplified as a one-dimensional problem. The heat flux from gas to slabs is expressed as the heat flux from the surface to the inner part and is reduced due to the additional thermal resistance of the oxide as follows:

$$q'' = \frac{T_s - T_i}{{L_s}/{k_{th,s}} + {L}/{k_{th}}} \tag{3.1}$$

where T_s is outermost the scale layer temperature, T_i is the slab internal temperature, L_s is the thickness of scale layer, L is the thickness of slab, $k_{th,s}$ is the thermal conductivity of scale, and k_{th} is the thermal conductivity of steel slabs. The term ${L_s}/{k_{th,s}}$ represents the additional thermal resistance caused by the scale. In order to numerically calculate the heat flux when the scale thickness changes throughout the heating process, thermal conductivity in the first cell layer of the slab is adjusted to consider the additional thermal resistance of the scale layer. This is

accomplished using the following relation that has been derived to find said effective thermal conductivity using a thermal resistance network concept:

$$k_{th,eff} = \frac{L_{steel}}{{L_s}/{k_{th,s}} + {L_{steel}}/{k_{th}}} \tag{3.2}$$

where the previous meanings for all variables hold. Of note is that L_{steel} is the thickness of the numerical cell being modified with the effective thermal conductivity by the UDF and is not the entire slab thickness. As the effect of the scale on the heat transfer into the slab is being modeled as such, there is no need to model the scale layer geometry. To account for the heat released by the formation of the dominant iron oxide, wüstite, the relation $\Delta G^0 = -529{,}780 + 129T$ $(\frac{J}{mol})$ is used. This method can simplify the problem while still obtaining precise results.

3.2 Governing Equations

The governing equations determine the solution of the simulation through the solution of the conservation equations for momentum, mass, and energy, along with scalar transport equations. ANSYS Fluent © 18.2 and 19.2 were used to solve the numerical equations. The overall solver is the pressure-based coupled solver (PBCS), and all equations are solved using second order schemes except for the discrete ordinates model. In addition to the PBCS, the pseudo-transient method was utilized. Both solver settings have been found to be more efficient than the alternative – the PBCS can converge as much as 5x as fast as the default SIMPLE solver and the pseudo-transient method can yield 30-50% speedups [64].

3.2.1 Continuity

Conservation of mass is the absolute minimum criterion a simulation should followed. The mass conservation equation is succinctly written as:

$$\frac{\partial \rho}{\partial t} + \nabla \cdot (\rho \vec{v}) = 0 \tag{3.3}$$

where ρ is density, t refers to time, and $\vec{v}$ is the velocity vector.

3.2.2 Momentum

The conservation of momentum is solved through:

$$\frac{\partial}{\partial t}(\rho\vec{v}) + \nabla \cdot (\rho\vec{v}\vec{v}) = -\nabla p + \nabla \cdot (\bar{\bar{\tau}}) + \rho\vec{g} \quad (3.4)$$

where p is the static pressure. $\rho\vec{g}$ is the gravity body force. The stress tensor, $\bar{\bar{\tau}}$, is calculated by:

$$\bar{\bar{\tau}} = \mu[(\nabla\vec{v} + \nabla\vec{v}^{\mathrm{T}}) - \frac{2}{3}\nabla \cdot \vec{v}I] \quad (3.5)$$

where μ is the molecular viscosity and I is the unit tensor.

3.2.3 Turbulence

The turbulence model used is that developed initially by Jones and Launder in 1972 and then improved upon by Shih et al. in 1995 [65-66]. The original model developed by Jones and Launder was the k-ε turbulence model, where k is the turbulent kinetic energy and ε is the turbulent energy dissipation rate. This model replaced the mixing-length hypothesis; the k-ε turbulence model more accurately modelled the turbulence, especially near the boundary, than the mixing-length hypothesis was able to. Shih et al. then modified the k-ε turbulence model from the standard version to the realizable version by changing the formulation for some turbulent parameters. This formulation is realizable as it satisfies mathematical constraints for the Reynolds stresses [67]. For an in-depth explanation, the interested reader is referred to the paper by Shih et al. [66].

The realizable k-ε turbulence model has been found by Kim et al. to be the most accurate out of standard, RNG, and realizable k-ε turbulence models [68], and the only model of the three to capture the flow reversal phenomena. The realizable k-ε turbulence model was chosen for this study as the computational cost in going from standard to realizable is minimal, and the return in accuracy is great. Reynolds-averaged Navier-Stokes (RANS) equations have been used to solve for the turbulence parameters without directly simulating the turbulence.

The realizable k-ε turbulence model is modelled via the transport equations for k and for ε:

$$\frac{\partial}{\partial t}(\rho k) + \frac{\partial}{\partial x_j}(\rho k u_j) = \frac{\partial}{\partial x_j}\left[(\mu + \frac{\mu_t}{\sigma_k})\frac{\partial k}{\partial x_j}\right] + G_k + G_b - \rho\varepsilon - Y_M \quad (3.6)$$

and

$$\frac{\partial}{\partial t}(\rho\varepsilon) + \frac{\partial}{\partial x_j}(\rho\varepsilon u_j) = \frac{\partial}{\partial x_j}\left[\left(\mu + \frac{\mu_t}{\sigma_\varepsilon}\right)\frac{\partial \varepsilon}{\partial x_j}\right] + \rho C_1 S_\varepsilon - \rho C_2\left(\frac{\varepsilon^2}{k+\sqrt{\nu\varepsilon}}\right) + C_{1\varepsilon}\left(\frac{\varepsilon}{k}\right)C_{3\varepsilon}G_b \quad (3.7)$$

where k and ε hold their previous definitions. ρ is the density of the mixture, u is the velocity component, x is the direction component, μ is the molecular viscosity, and μ_t is the turbulent

viscosity. G_k and G_b are the generation of turbulence kinetic energy from the mean velocity gradients and due to buoyancy respectively. Y_M is for the contribution of the fluctuating dilatation in compressible turbulence to the overall dissipation rate. C_2 and $C_{1\varepsilon}$ are constants, as are σ_k and σ_ε. These constants are, in order, 1.9, 1.44, 1.0, and 1.2. *C1* is equal to:

$$C_1 = \max\left[0.43, \left(\frac{(\frac{k}{\varepsilon})\sqrt{2S_{ij}S_{ij}}}{(\frac{k}{\varepsilon})\sqrt{2S_{ij}S_{ij}}+5}\right)\right. \tag{3.8}$$

The eddy viscosity, μ_t, from above is computed through:

$$\mu_t = \rho(\frac{k^2}{\varepsilon})(\frac{1}{A_0+A_s(\frac{k}{\varepsilon})\sqrt{S_{ij}S_{ij}+(\overline{\Omega_{ij}}-\varepsilon_{ijk}\omega_k-2\varepsilon_{ijk}\omega_k)(\overline{\Omega_{ij}}-\varepsilon_{ijk}\omega_k-2\varepsilon_{ijk}\omega_k)}}) \tag{3.9}$$

where $\overline{\Omega_{ij}}$is the mean rate-of-rotation tensor viewed in a rotating reference frame with angular velocity ω_k. A_0 is 4.04 and A_S is found through:

$$A_s = \sqrt{6}\cos\left[\frac{1}{3}\cos^{-1}\left(\sqrt{6}\left(\frac{S_{ij}S_{jk}S_{ki}}{\sqrt{S_{ij}S_{ij}}}\right)\right)\right] \tag{3.10}$$

The term *S* with subscript of *ij*, *jk*, or *ki* can be found from:

$$S_{ij} = \frac{1}{2}(\frac{\partial u_j}{\partial x_i} + \frac{\partial u_i}{\partial x_j}) \tag{3.11}$$

with *i* and *j* replaced by the necessary directional letters for each formulation.

As the realizable k-ε turbulence model is being used, the selection of a wall treatment is needed. Wall treatments represent the flow near the wall, which is usually made up of three layers: the viscous sublayer at the wall, the fully turbulent layer away from the wall, and an interim layer between the two [67]. For the viscous sublayer, the molecular viscosity dominates the flow; for the fully turbulent layer, turbulence dominates. The interim, 'buffer,' layer is equally affected by the molecular viscosity and the turbulence. For this simulation, the standard wall function developed by Launder and Spalding was used, which allows for somewhat coarse mesh near the boundaries [69].

3.2.4 Energy

Heat transfer throughout the domain needs to include conduction, convection, and radiation. Radiation modeling is slightly more complex and requires further modeling efforts that

can be found in detail in the next section. Overall, the general energy balance within the system is calculated with [67]:

$$\frac{\partial}{\partial t}(\rho E_e) + \nabla \cdot \left(\vec{v}(\rho E_e + p)\right) = \nabla \cdot \left(k_{th,eff}\nabla T - \sum_j h_j \overrightarrow{J_j} + \left(\bar{\bar{\tau}}_{eff} \cdot \vec{v}\right)\right) + S_h \qquad (3.12)$$

where k_{eff} is the effective thermal conductivity (different than that defined for scale formation above), $\bar{\bar{\tau}}_{eff}$ is the effective stress tensor, $\overrightarrow{J_j}$ is the diffusion flux of species j, and S_h, here, represents the radiation source terms from the radiation model. Terms previously defined hold their definition. h is the sensible enthalpy, T is the temperature, and E_e is the total energy as defined by:

$$E_e = h - \frac{p}{\rho} + \frac{v^2}{2} \qquad (3.13)$$

For the non-premixed, non-adiabatic combustion model, the total enthalpy can be calculated from:

$$\frac{\partial}{\partial y}(\rho H) + \nabla \cdot (\rho \vec{v} H) = \nabla \cdot \left(\frac{k_{th}}{c_p}\nabla H\right) + S_h \qquad (3.14)$$

where H is the summation of the product of mass fraction and enthalpy for each species. c_p is the specific heat with constant pressure. The above equation for the non-premixed combustion model assumes that the Lewis number is at or close to unity.

3.2.5 Radiation

Radiation, in general, is solved for using the radiative transfer equation (RTE) [70]:

$$\frac{dI(\vec{r},\vec{s})}{ds} + (a + \sigma_s) I_{rad}(\vec{r},\vec{s}) = an^2\left(\frac{\sigma T^4}{\pi}\right) + \frac{\sigma_s}{4\pi}\int_0^{4\pi} I_{rad}(\vec{r},\vec{s}')\Phi(\vec{s}\cdot\vec{s}')d\Omega' \qquad (3.15)$$

where $\vec{r}$ is the position vector, $\vec{s}$ is the direction vector, $\vec{s}'$ is the scattering direction vector, and s is the path length. The absorption coefficient, refractive index, scattering coefficient, and radiation intensity are a, n, σ_s, and I_{rad} respectively. σ is the Stefan-Boltzmann constant, and pi, as per usual, is represented by π. Φ is the phase function and Ω' is the solid angle. This equation considers the incoming and outgoing radiation along with scattering and absorbing phenomena.

The discrete ordinates (DO) model is used in this study as it is more accurate that then P1 model at the cost of some computational resources. The DO model was largely developed by Fiveland and Truelove along with their colleagues in the 1970's and 1980's [71-73]. Further

improvement on this model was realized by Chui and Raithby when they applied radiation modeling using the finite volume method on non-orthogonal grids [74]. Previously, radiation modeling was only used on orthogonal grids, which limits the geometry and extent of the modeling. With this model, the weighted-sum-of-gray-gases model (WSGGM) is also used to calculate the absorption coefficient as a function of the domain's species composition. The discrete ordinates model transforms the RTE into:

$$\boldsymbol{\nabla \cdot (I_{rad}(\vec{r},\vec{s})\vec{s})} + (a+\sigma_s)I_{rad}(\vec{r},\vec{s}) = an^2\left(\frac{\sigma T^4}{\pi}\right) + \frac{\sigma_s}{4\pi}\int_0^{4\pi} I_{rad}(\vec{r},\vec{s}')\Phi(\vec{s}\cdot\vec{s}')d\Omega' \quad (3.16)$$

Note that the major change between the two equations has been bolded.

The WSGGM was used by Hottel et al. as a part of his study of radiation modeling within a furnace [13]. It is a compromise between a very laborious and computationally costly calculation of the absorptivity at every absorption band versus the simpler constant absorptivity. The WSGGM calculates the emissivity and the absorptivity as, respectively:

$$\epsilon = \sum_{i=0}^{I} \kappa_{\epsilon,i}(T)(1 - e^{-a_i p s}) \quad (3.17)$$

and

$$a = -\frac{\ln(1-\epsilon)}{s} \quad (3.18)$$

where, again, a is the absorption coefficient and ϵ is the emissivity. s is the distance over which these values are calculated over, called the 'pale length'. $\kappa_{\epsilon,i}$ is the emissivity weighting factor for the *i*th gray gas, a_i is the absorption coefficient of the *i*th gray gas, and *p* is the sum of the partial pressures of all absorbing gases. Coefficients for the WSGGM to help solve for the unknowns are from two papers, one paper written by Coppalle and Vervisch and another written by Smith et al. [76-77]. They consider H_2O and CO_2, which are both the main radiating species in the product gases. N_2 is not a radiating species.

3.2.6 Species Transport

The combustion phenomena were modelled using the non-premixed combustion models, the steady flamelet model (SFM) and the equilibrium model. A study of the various models in terms of accuracy and efficiency was undertaken to use the model that best balances both, the results of which can be found in the next sub-section.

These models can be used as the oxidant and the fuel enter the furnace in a non-premixed condition. The non-premixed combustion models reduce the thermochemistry to a parameter called the mixture fraction (*f*) and the scalar dissipation rate (χ). The reaction is then driven by mixing and all reactions are assumed to be very fast [78]. The equilibrium model models the combustion as at equilibrium and can handle three distinct flows, whether fuel or oxidant. It only requires the thermodynamics of the system. The steady flamelet model requires both the kinetics and the thermodynamics of the mechanism to model the near chemical equilibrium state. The SFM can only handle a single oxidant and a single fuel and represents a 3D turbulent flame as a combination of multiple, 2D laminar diffusion flamelets [79].

Both of these models, as mentioned earlier, assume a Lewis number of unity, which would necessitate the diffusivities of all species to be the same [79]. The turbulence-chemistry interaction is then modeled by the mixture fraction through an assumed-shape probability density function (PDF). A beta-function shaped PDF is chosen for all cases as it can handle both one and two mixture fractions. Non-adiabatic modeling requires that the thermochemical state is related to both the mixture fraction and the enthalpy. For a single mixture fraction, a 3D look-up table is generated. For two mixture fractions, a 5D look-up table is generated.

The mixture fraction is simply defined as:

$$f = \frac{Z_i - Z_{i,ox}}{Z_{i,fuel} - Z_{i,ox}} \tag{3.19}$$

where Z_i is the elemental mass fraction for element *i* and subscripts are for values at the oxidizer stream inlet (*ox*) and the value at the fuel stream inlet (*fuel*).

The scalar dissipation rate is a measure of how far the reaction is from equilibrium. This parameter can be found through:

$$\chi = 2D|\nabla f|^2 \tag{3.20}$$

and

$$\chi_{st} = \frac{a_s \exp\left(-2\left[erfc^{-1}(2f_{st})\right]^2\right)}{\pi} \tag{3.21}$$

where *D* is the representative diffusion coefficient for the first equation. For the second equation, χ_{st} is the scalar dissipation at the stoichiometric mixture fraction, f_{st} is the stoichiometric mixture

fraction, a_s is the characteristic strain rate, and $erfc^{-1}$ is the inverse complementary error function.

The transport equation for the mixture fraction (*f*) is:

$$\frac{\partial}{\partial t}\left(\rho\bar{f}\right) + \nabla\cdot\left(\rho\vec{v}\bar{f}\right) = \nabla\cdot\left(\frac{\mu_t}{\sigma_t}\nabla\bar{f}\right) \tag{3.22}$$

where the overbar refers to the Favre mean, or density-averaged, mixture fraction. The mixture fraction variance ($\overline{f'^2}$) is also solved for via:

$$\frac{\partial}{\partial t}\left(\rho\overline{f'^2}\right) + \nabla\cdot\left(\rho\vec{v}\overline{f'^2}\right) = \nabla\cdot\left(\frac{\mu_t}{\sigma_t}\nabla\overline{f'^2}\right) + C_g\mu_t\left(\nabla\bar{f}\right)^2 - C_d\rho\left(\frac{\varepsilon}{k}\right)\overline{f'^2} \tag{3.23}$$

where $f' = f - \bar{f}$. Constant values for σ_t, C_g, and C_d are 0.85, 2.86, and 2.0 respectively.

With the composed PDF of f and χ_{st}, mean scalars can be found through the general formula:

$$\bar{\phi}_\iota = \int_0^1 \phi_i(f,\bar{H}_d)p(f)df \tag{3.24}$$

where $\bar{\phi}_\iota$ is the density-averaged scalar. $p(f)$ here is the PDF, and $\bar{H}_d$ is the density-averaged enthalpy.

The SFM requires the generation of a PDF file and a flame file. Flames are generated at scalar dissipation rate values calculated by:

$$\chi_i = \begin{cases} 10\chi_{i-1} & for\ \chi_{i-1}<1s^{-1} \\ \chi_{i-1} + \Delta\chi & for\ \chi_{i-1}\geq 1s^{-1} \end{cases} \tag{3.25}$$

where $\Delta\chi$ is the defined scalar dissipation step and i goes from 1 to the defined maximum number of flamelets.

For the kinetics and thermodynamics, the San Diego Mechanism data files were used [80].

3.3 Combustion Models Study

ANSYS Fluent provides various combustion models. For most reheat furnace burners, the air and the fuel enter in discrete streams and are not premixed. Fluent can model these types of flames through using non-premixed methods or through fine rate formulations. The actual models are the steady flamelet model and the equilibrium model for non-premixed methods and the eddy-

dissipation model and the eddy-dissipation concept model for the finite rate formulations. Each of the models has their benefits and detriments that are explored here.

The SCALING 400 study was undertaken by the International Flame Research Foundation and the Gas Research Institute to find correlations between burners of different scales [81]. Their scaled burner design is shown in Fig. 3.2. For the purposes of this study, a 2D axisymmetrical replica of this burner configuration was made and all combustion conditions from the study for the baseline burner case were applied as conditions. As it is a 2D burner, some simplifications were made that resulted in equivalent mass flow and velocity, such as the replacement of the 24 fuel inlets by a single inlet of equivalent axisymmetrical area. The walls of the furnace were held at constant temperatures and the fuel used was natural gas with 96.5 vol% methane.

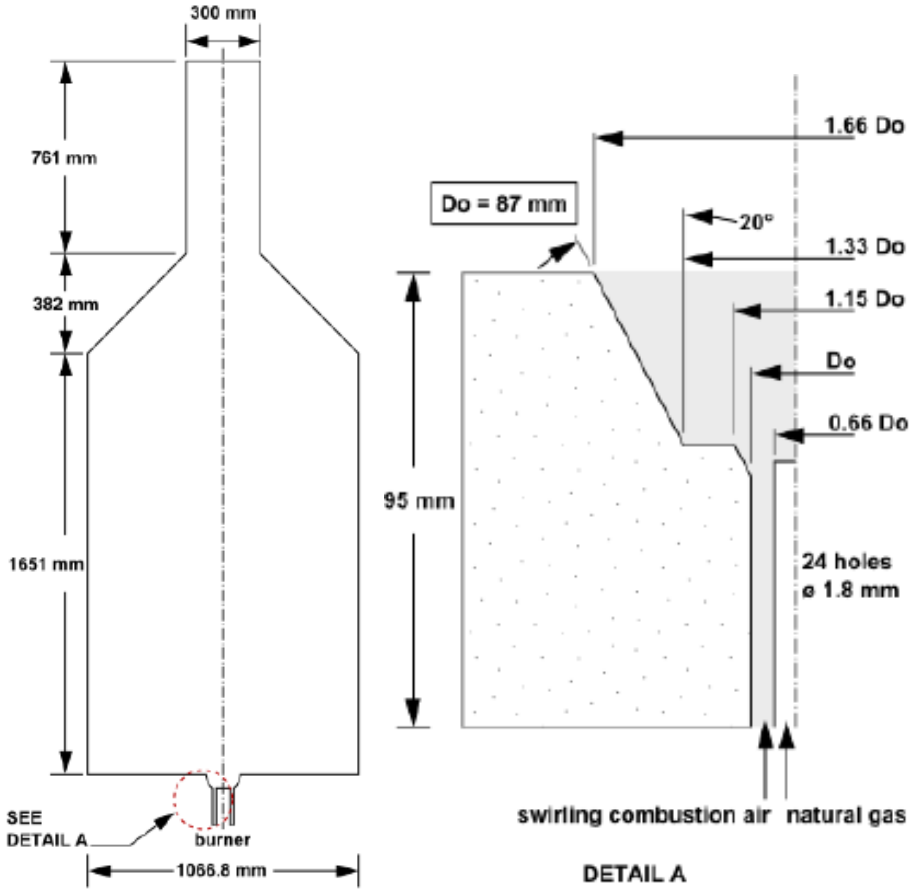

Fig. 3.2 Burner configuration from experimental work [80]

Four comparison cases were run with exact same conditions and mesh. A mesh detail near the inlet (Fig. 3.3) shows the symmetry along with both the fuel and air inlets. This mesh was

generated by adapting the mesh from the solution based on the normalized temperature gradient. The combustion model chosen to adapt the mesh on was the steady flamelet model using the San Diego mechanism This mesh adaptation continued until the solution converged within 200 iterations between the adaption cycles. The final mesh for this study had 13,051 cells in total. All cases were run using an Intel® Xeon® CPU e5-2630 v4 with 1 processor in serial. All previously defined models for turbulence, radiation, and ancillary functions mentioned in preceding sections were also used for this study. The four comparison cases used different combustion models as described above with the exclusion of the eddy-dissipation concept model. For the steady flamelet model, the San Diego Mechanism and the GRI-MECH 3.0 thermodynamics and kinetics mechanism were used [80,82]. The equilibrium model also used the San Diego Mechanism thermodynamics data. For the eddy-dissipation model, the simple Westbrook and Dryer 2-step reaction mechanism was used [83].

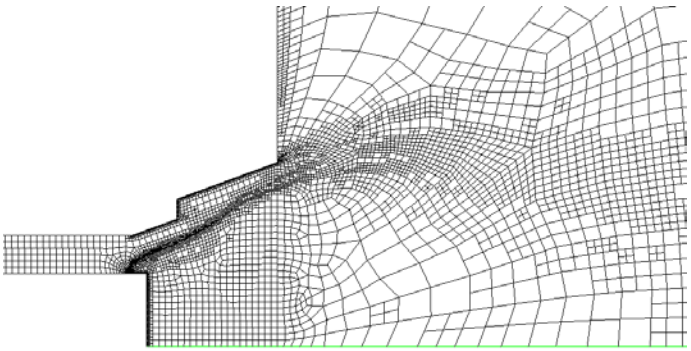

Fig. 3.3 Adapted 2D mesh

Each simulation was run to convergence and the iterations and total time to reach convergence is displayed in Fig 3.4. The largest difference in time to convergence is found between the non-premixed models and the eddy-dissipation model (ED). The eddy-dissipation model case took 6.6 times the amount of time with less reactions and species solved for. To solve the same reactions and species would result in an astronomical increase in computation time for the eddy-dissipation model. This is especially unfortunate compared to how similar all of the non-premixed models are despite their differences.

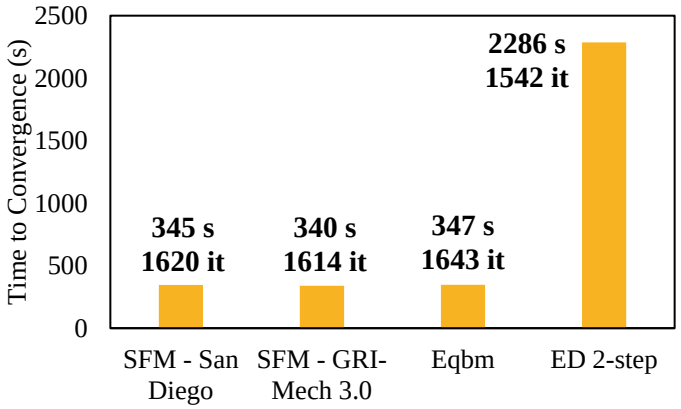

Fig. 3.4 Comparison of solve times for combustion models

While the time savings may be tempting to use as the full reasoning behind the choice of using non-premixed combustion models, accuracy of the solution is of the utmost importance. Comparison of flue temperatures and species compositions are shown in Fig. 3.5. Comparing the models against each other shows very little deviation. Comparing the numerical results against the experimental shows that the numerical results overpredicted the flue temperature, underpredicted the carbon dioxide content in the flue gas, and overpredicted the oxygen content in the same. The average difference in CO_2 was +1.47% and in O_2 was -2.63%. The average difference in temperature was only +4.25%.

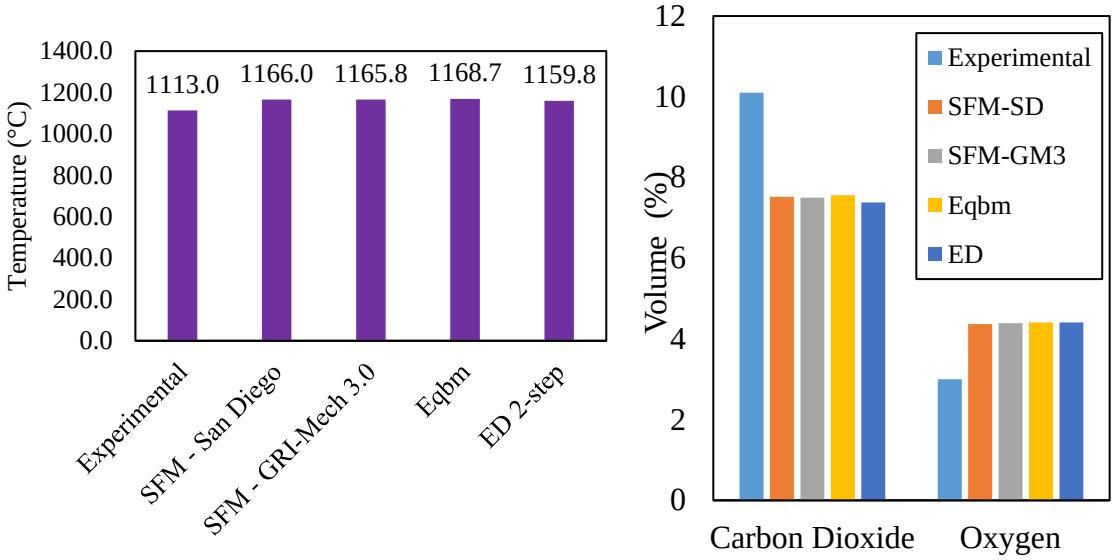

Fig. 3.5 Flue temperature (left) and species comparisons (right)

The SCALING 400 study has tabulated multiple values for temperature and species volume fractions. Fig. 3.6 shows the comparison of radial temperature from two axial locations (27 mm and 432 mm from the burner outlet). For Fig. 3.6a, the shared flame width is marked by an orange dashed line. Further from the centerline of the flame shows how similar each combustion model is in terms of the product temperature. Inside of the flame, however, the differences are much larger because of strain rate and species considered, especially the formation and destruction of radicals. All models compare quite favorably to the experimental measurements at 27 mm, but this favorable comparison does not continue onward at 432 mm. It is believed that this is due to the use of a 2D domain and its effect on the flow and thus the flame length and flame speed.

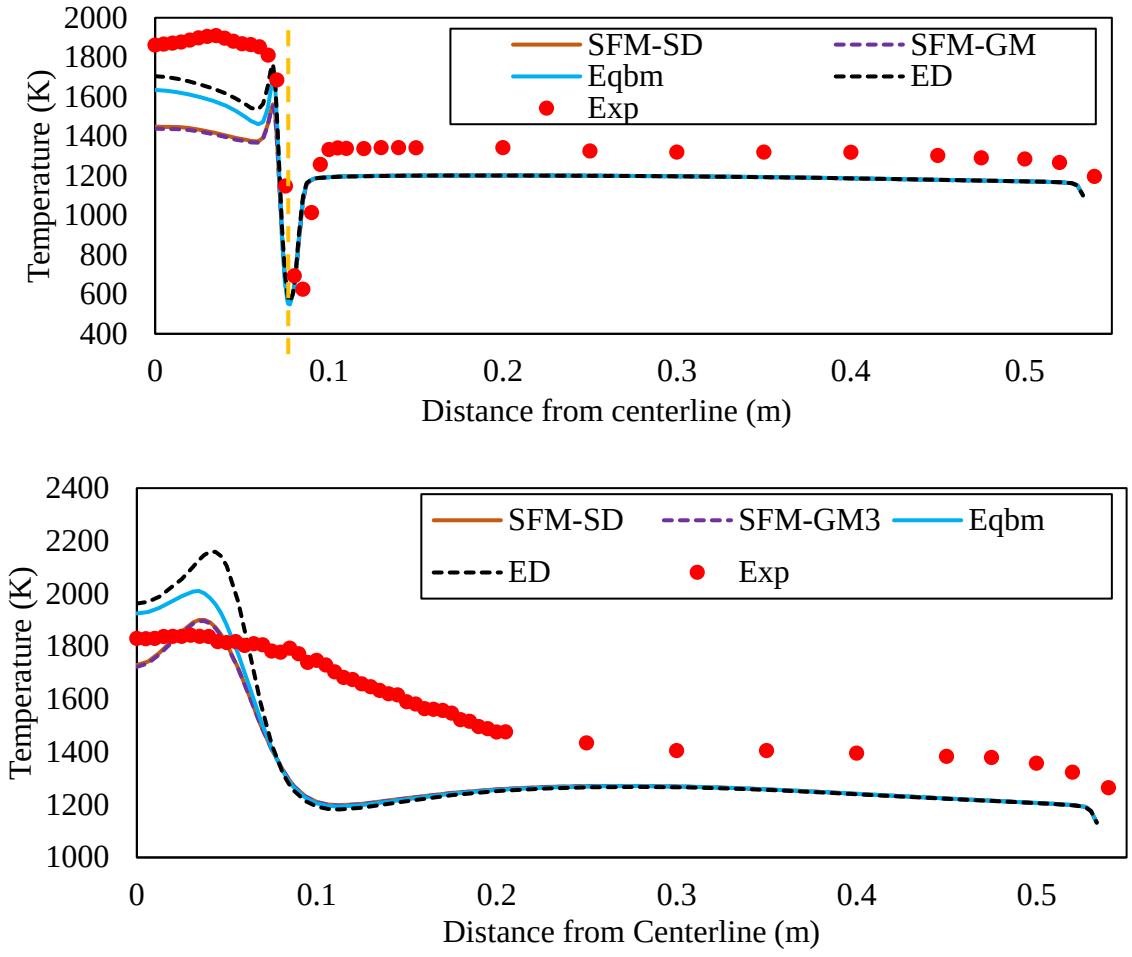

Fig. 3.6 Radial comparisons of temperature at a axial distance from the burner outlet of 27 mm (top) and 432 mm (bottom)

The species were also compared with the flame length noted on each sub-figure of Fig. 3.7. Note that the figures all share the same legend shown in Fig. 3.7a. The flame width is shown on each figure. Like temperature, outside of the flame shows how similar all of the combustion models are, whereas some striking differences are found in the flame. Validation of these models against the experimental method is not necessary due to the wealth of validation previously done for each mechanism, but the trends of growth or reduction around the flame edge are fairly accurate for each model. The largest discrepancies were found in-flame for carbon monoxide prediction.

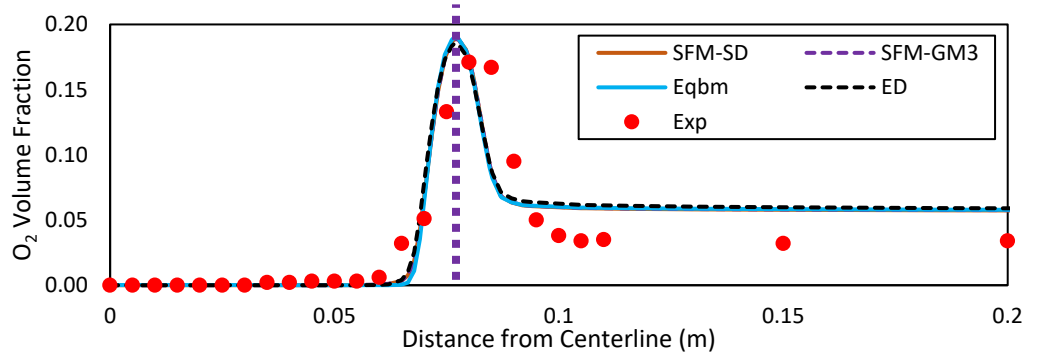

(a)

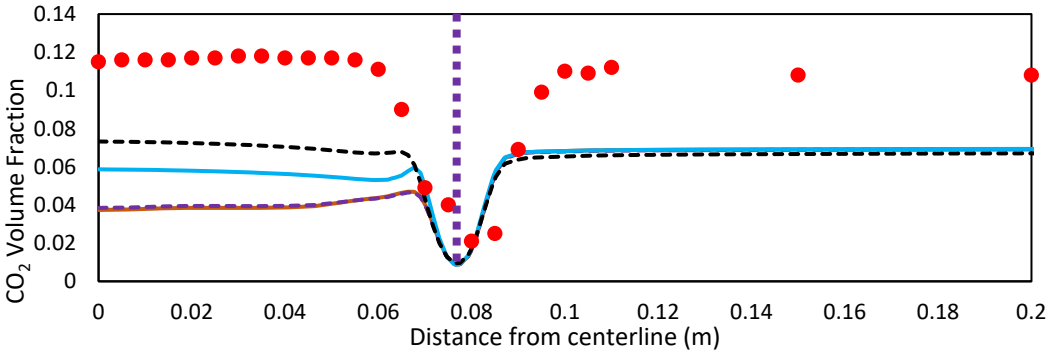

(b)

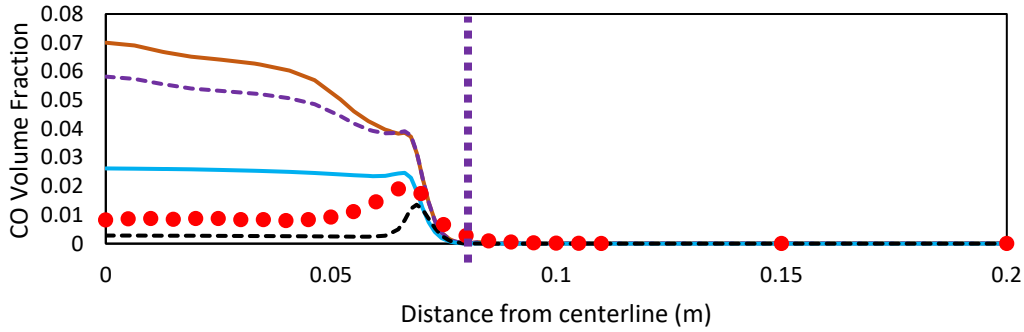

(c)

Fig. 3.7 Volume fraction comparisons at an axial distance of 27 mm for (a) oxygen, (b) carbon dioxide, and (c) carbon monoxide

The overall findings are that the models are nearly identical when predicting temperature and species outside of the flame. Within the flame region, there are much larger differences, with the eddy-dissipation model with the 2-step Westbrook & Dryer mechanism most often the closest to the experimental measurements. In terms of speed, the eddy-dissipation model took 6.6 times the amount of time to converge. Scaling this to a 3D case with a larger mesh could prove to outweigh any benefit given by the eddy-dissipation model. As such, the non-premixed combustion models are recommended over the finite-rate combustion models. The San Diego mechanism is the most up-to-date hydrocarbon combustion mechanism, so it is recommended for use with the steady flamelet model.

3.4 Computational Domain and Mesh

The furnace of study in this work is the ArcelorMittal Burns Harbor location pusher furnace #1. Dimensions and engineering drawings of the furnace were provided by ArcelorMittal. Mentioned previously, the domain is half of the industrial furnace to exploit symmetry in the geometry. This simplified domain allowed for a denser mesh in crucial regions related to areas of mixing and combustion. The slab domain is a rectangular prism and is also halved to match the full furnace domain. Fig. 3.8 shows the domain of the full furnace. The full furnace is 112 feet long, 24 feet tall, and 34 feet wide. The slab domain is modeled after an industrial slab of average dimensions 318” x 55” x 9.9”. It is halved along the largest dimension.

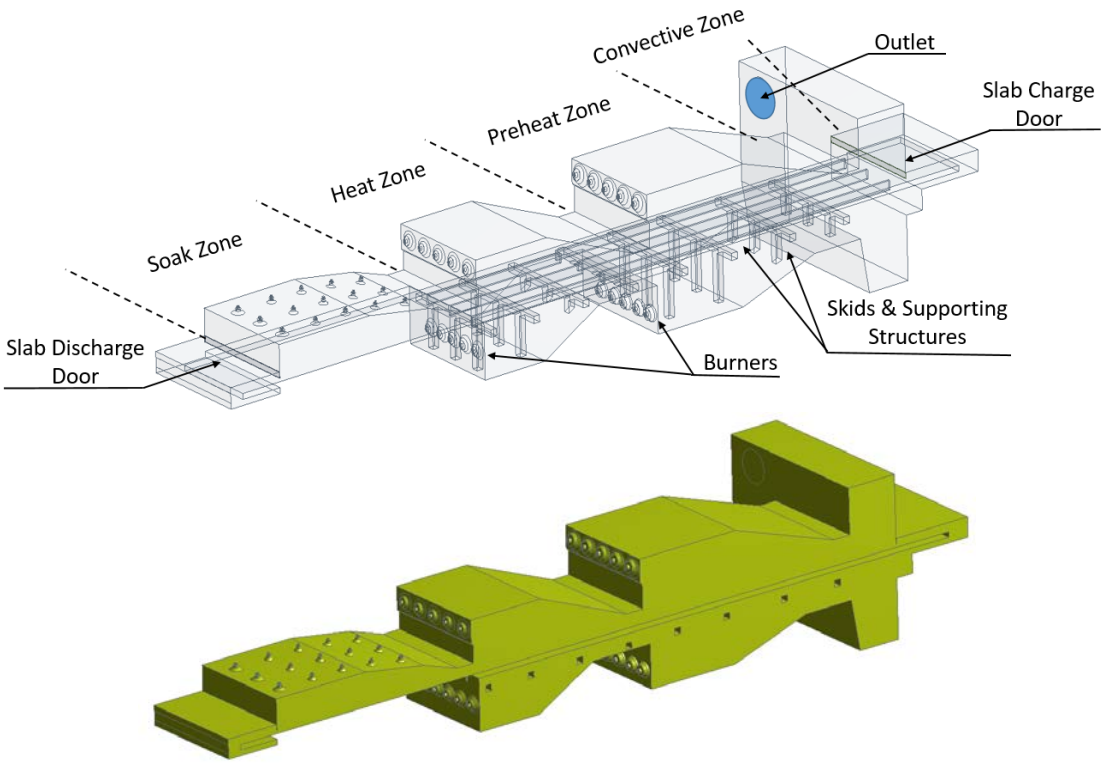

Fig. 3.8 Domain of the full furnace model with transparency (top) and without (bottom)

In the full furnace, there is the preheat, heat, and soak zones. Of the three, only the soak zone does not have bottom burners, but instead a hearth that the slabs are pushed along. As this is a pusher-type furnace, the slabs rest on water-cooled skids. Skids effect the slab heating via radiative shielding [4], so they were modelled as wall boundaries on the bottom of the slabs. Supporting structures were also cut from the domain to model any potential flow obstruction. In this way, the radiative shielding and the flow changes caused by the skid and structural supporting skids was modelled without modeling the conduction or convective heat transfer, which accounts for very little of the skid impact. The outlets consist of the main furnace outlet and the furnace charge and discharge doors, which are modelled as slightly open. The main furnace outlet is above and to either side of the furnace charge door, thus encouraging the flow to travel in the opposite direction to the slabs.

The domain was discretized into a mesh with 16.77 million high-quality cells for the full furnace model. Mesh was finest near the burners to capture mixing phenomena. The mesh is not shown in detail to avoid issues related to confidential information.

3.5 Validation

Industry data has been used to validate the full furnace model. For scale formation model validation, the previous validation provided in the previous chapter of this work suffices. Validation for scale formation against industrial data was not possible during the timeline of this work.

3.5.1 Boundary Conditions

Boundary conditions were largely provided by industrial collaborators at ArcelorMittal. Conditions were monitored throughout a given day and key boundary conditions were tracked. A slab with thermocouples drilled into it was also run through under these conditions. As such, validation is possible through full furnace measurements and through slab temperature evolution with time.

Fuel and air conditions are shown in Table 3.1. Again, only the preheat and heat zones have a top and a bottom section of burners. The soak zone is primarily composed of small burners (Soak Small) with a row of larger burners (Soak Large) near the discharge of the furnace. There is a secondary and primary air due to the staged combustion instigated by the burner setup. The secondary air is 80% of the total air. Of note is that the air temperature is elevated due to recuperative technology already in use at this facility. These values are averaged over hours of tracked data provided by industry and input uniformly for each burner. These conditions are for the total of all burners in each zone; as such, each burner will get the same fraction of this total.

Table 3.1 Fuel and air inlet conditions

Zone	Fuel (kg/s)	Primary Air (kg/s)	Secondary Air (kg/s)	Air Temperature (°F)	Fuel Temperature (°F)
Preheat Top	0.706	2.896	11.583	811.3	80
Preheat Bottom	0.566	2.357	9.428	811.3	80
Heat Top	0.297	1.140	4.559	811.3	80
Heat Bottom	0.208	0.799	3.195	811.3	80
Soak Small	0.193	4.009	N/A	811.3	80
Soak Large	0.093	1.788	N/A	811.3	80

The fuel in question is natural gas with a methane content of 95.98 vol% along with 2.26 vol% ethane and other trace species such as nitrogen, carbon dioxide, and propane. Only those species with more than 0.1 vol% are input into the model.

The initial temperature profile assigned as the boundary condition on the slab walls was derived as a piecewise function from the slab thermocouple temperatures recorded. This temperature evolution and the breakdown of the function per zone is shown in Fig. 3.9. In this graph, a 'recuperative' zone is labeled. This zone, also called the non-firing zone, shows a slight increase in slab temperature due to convective heat transfer from high temperatures gases produced from the subsequent firing zones. This area is near the main outlet of the furnace, so all gas flow passes over these relatively cold slabs. These temperatures only vary in the direction of slab travel and are thus uniform in the axial direction. This is untrue for further slab temperature profiles provided via the iterative methodology described previously.

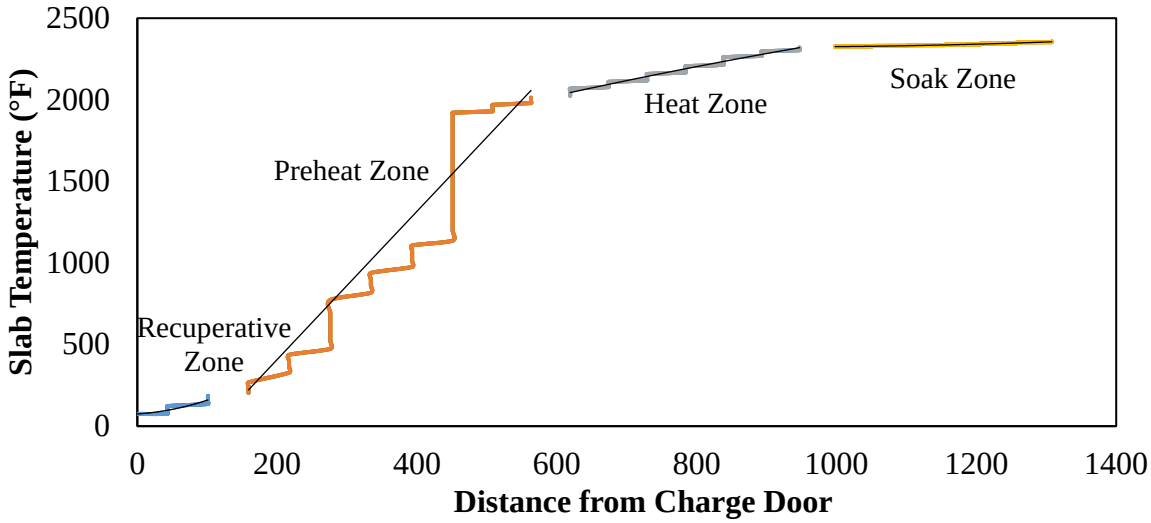

Fig. 3.9 Slab temperature throughout the furnace from thermocouple measurements

Furnace and skid walls are modelled as adiabatic. The emissivity of the slabs is assumed to be a constant 0.75. Slabs travel at a constant velocity to meet the average residence time determined from the tracked data provided by industry. Scale formation was assumed to be nonexistent at furnace charge.

Burner configurations are confidential. However, the complex pipe structures associated with the burners have been simplified and flow is assumed to be fully developed turbulent flow at the burner inlets.

3.5.2 Results and Discussion

This model is a variation on a previously validated model [63]. The largest change in the model is the type of combustion model. As previously discussed in section 3.3, the combustion model differences are largest in the flame. As most of the thermocouples are not found directly in the flame, it is expected that the furnace gas temperatures will be approximately the same. Thermocouple locations were provided by industry and can be found in Fig. 3.10.

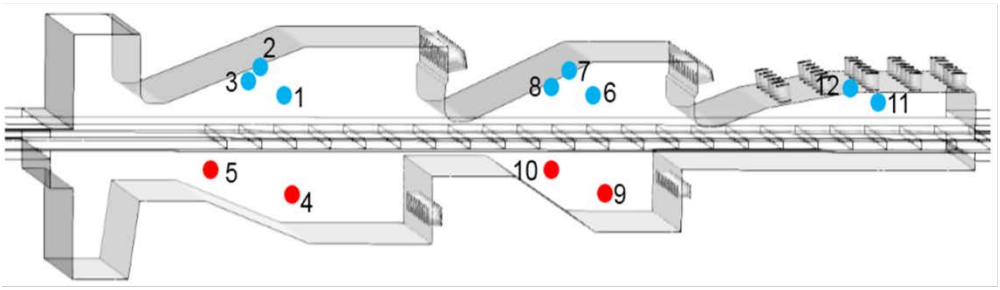

1. Top Preheat Zone West
2. Top Preheat Zone East
3. Top Preheat Zone Middle
4. Bottom Preheat Zone West
5. Bottom Preheat Zone East
6. Top Heat Zone West
7. Top Heat Zone East
8. Top Heat Zone Middle
9. Bottom Heat Zone West
10. Bottom Heat Zone East
11. West Soak Zone
12. East Soak Zone

Fig. 3.10 Thermocouple locations within the furnace

Thermocouple comparisons in Table 3.2 show the largest differences in the top of the furnace, where the flame is closest to the thermocouple. The largest difference was 16.6% in the top preheat zone on the west side. This large difference may be due to the flame structure for this flow condition. The flow conditions are averaged, so it is possible that the flame is closer to the thermocouple location in the simulation than that for the industrial data measurement.

Table 3.2 Gas temperature comparisons

Location	Industrial Data (°F)	Simulation (°F)	Error
TPHZW	2367	2759	16.6%
TPHZE	2409	2728	13.2%
TPHZM	2374	2489	4.8%
BPHZW	2253	2317	2.8%
BPHZE	2311	2407	4.2%
THZW	2493	2764	10.9%
THZE	2480	2728	10.0%
THZM	2479	2574	3.8%
BHZW	2295	2387	4.0%
BHZE	2373	2390	0.7%
SZW	2457	2617	6.6%
SZE	2396	2617	9.2%

After nine iterations of the full methodology, the temperature evolution with time converged. The temperature of the slab at the end of the residence time (160 minutes) was predicted to be 1627 K, or 1353.85°C for an absolute difference of 2.12%. This comparison is done against a level-2 industrial model which has been independently validated by ArcelorMittal. As such, this model was found to acceptably predict the slab temperature distribution with time. The comparison of predicted core temperature by the simulation and by the level-2 model are shown in Fig. 3.11.

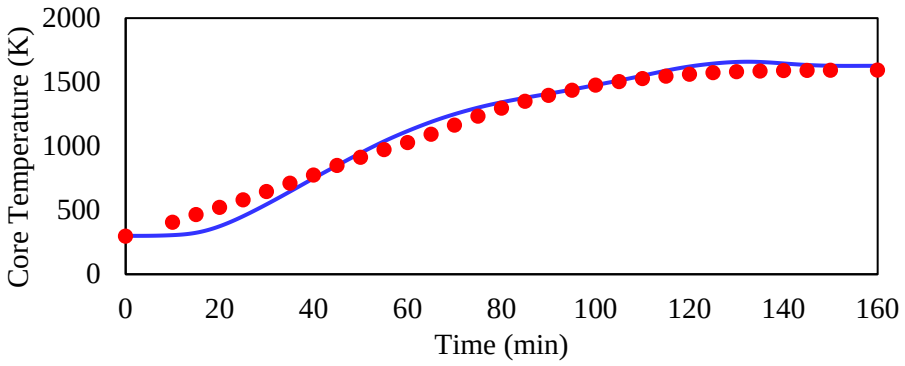

Fig. 3.11 Comparison of level-2 model data (red dots) with simulation prediction (blue line)

4. BASELINE CASE RESULTS

The baseline case reflects the everyday usage of the pusher-type reheat furnace. Boundary conditions have been provided by industrial partners and validated in Chapter 3 previously.

4.1 Operating Conditions and Boundary Conditions

The operating and boundary conditions are those used for validation purposes in Chapter 3. The extents for the domain can also be found in said chapter. Of note is that the conditions given in Table 3.1 are halved for use in the symmetrical domain.

4.2 Velocity Distributions

The gas flow conditions within the furnace are influenced by the momentum of the burner jets, the shape of the furnace, and the distribution of slabs within the furnace. Fig. 4.1 shows pathlines within the furnace as colored by velocity at different locations in the furnace; direction of slab movement is from left to right in these figures. Fig. 4.1a shows the centerline of the burner, where the recirculation zones are the most developed for the top and the bottom for the preheat and heat zones. Moving away from the centerline of the furnace towards the ways shows the recirculation zones changing for both top and bottom. For the bottom, the recirculation zone is disrupted by the presence of the supporting structures and losses coherence. The slabs do not obstruct the flow at the farthest wall burners, which results in larger interaction between the flow of the top and bottom recirculation zones. The recirculating gases from the top zones begin to dip into the bottom zones, which obstructs the flow in the bottom zone. This bottom zone flow is pushed towards the middle of the furnace, which also draws the flames inward. The recirculation zones within the outlet stacks also change as the outlets are not near the centerline.

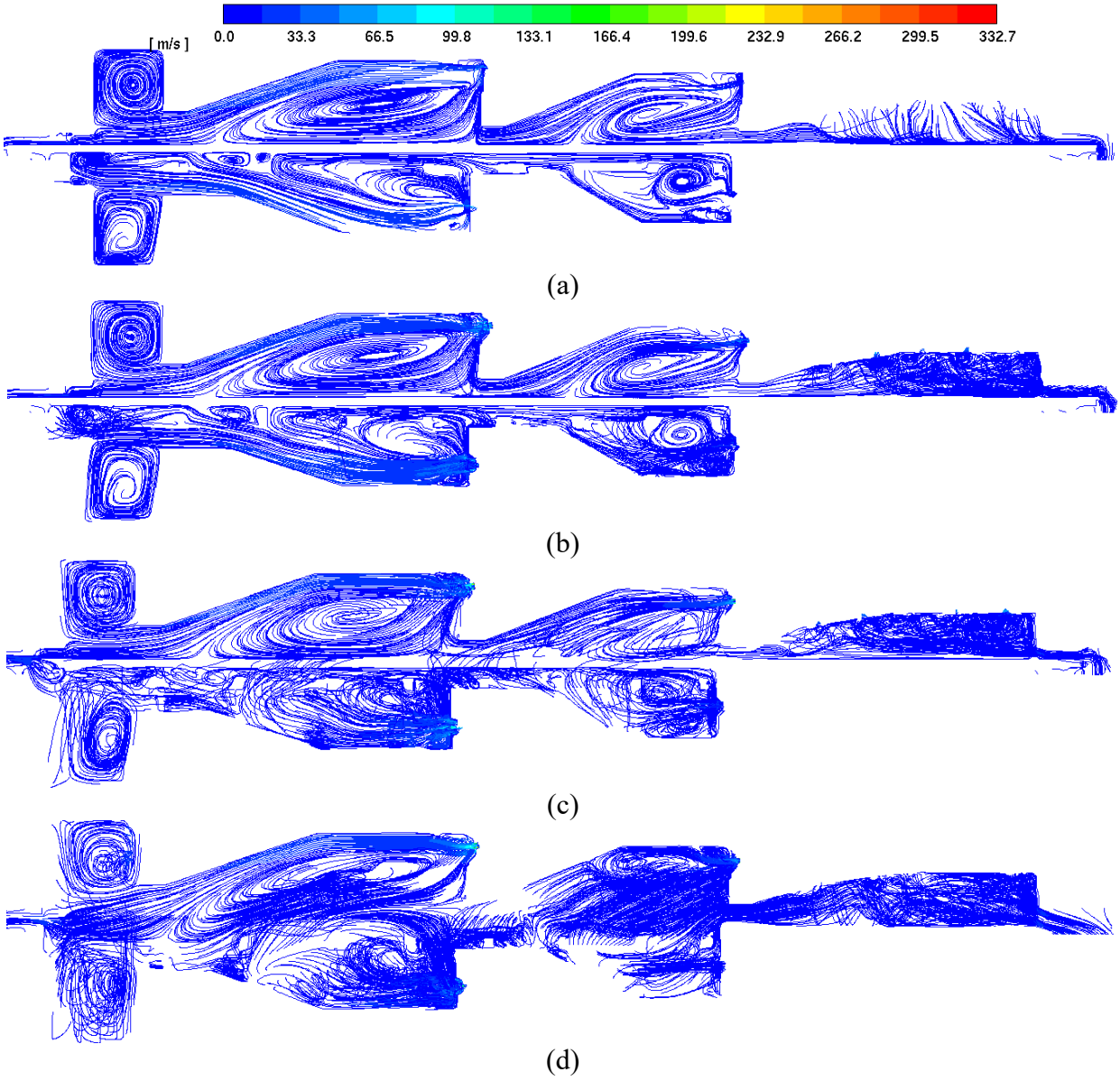

Fig. 4.1 Pathlines colored by velocity at (a) the centerline, (b) the closest top burners, (c) the middlemost top burners, and (d) the furthest top burners. Reference for burner location is from the furnace centerline and along the centerline of the burner.

Overall, these recirculation zones are causes by the high momentum flow from the burners and influenced by flow from later zones. Details for the preheat and heat zone flow are shown in Fig. 4.2. The flow from the burners in the preheat zone at the top first follows the contours of the roof of the furnace before either continuing on in a somewhat straight path to the outlet or being dragged backwards along the top of the slab before incoming flow from the heating forces it

upward and back into the jet of the burner. This also holds true for the heat zone, though flow from the soak zone seems to flow underneath the recirculation zone. The soak zone has top burners which do not promote the formation of recirculation zones to the extent found in the heat and preheat zones.

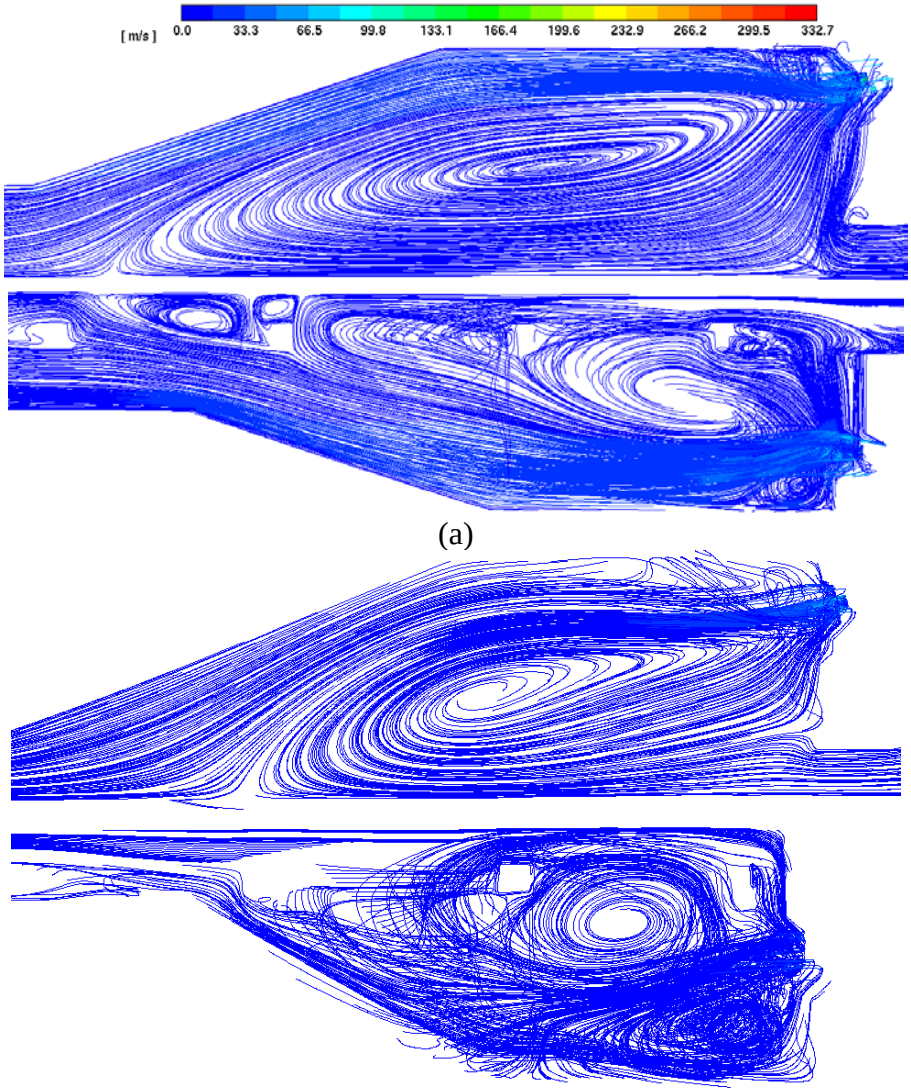

(a)

(b)

Fig. 4.2 Details of pathlines colored by velocity for (a) the preheat and (b) heat zones at the centerline of the top burners closest to the furnace centerline

For the bottom zones, the pattern of recirculation is slightly different due to presence of the supporting structure and the lack of an upstream zone for the bottom heat zone. The bottom heat zone does have a noticeable recirculation area in the middle of the zone with a smaller recirculation

area below the burner. This lower area is most likely due to the impingement of the jet from the burner on the upward slope from the bottom wall of the furnace. Very noticeable in the heat and preheat zones is the presence of the square-shaped supporting structures, which cause disruptions in the formation of larger zones of recirculating gas. The gases are forced to either go between the slab and the supporting structure – note that this is not the skid that the slab rests on – or to impact the supporting structure. As such, the recirculation zones in the bottom zones are much smaller and more varied in shape than those in the top zones. In the preheat zone, the supporting structures cause many different small vortices as the gases head toward the exit of the furnace through the recuperative zone.

Based on the work of Tang et al. on the accumulation of scale formation within reheating furnaces, the gas flow pathlines can be analyzed for likely locations of scale buildup [62]. In their work, they found that scale buildup occurred between the high velocity burner jets underneath reverse flows that struck the slabs. The flow along the slab would promote scale spallation, which would then strike the burner wall and fall down to the furnace bottom. Skid structures were found to reduce the reverse flow on the bottom of the skid, which led to less accumulation of scale around them.

For the furnace of interest in this work, similar reverse flow is apparent. Reverse flow is quite high near the centerline and along the side walls of the furnace. The bottom burners of this furnace are also located higher from the bottom of the furnace than that of the furnace used by Tang et al. This has resulted in the small areas of recirculation underneath the burner jets, which could promote the accumulated of sintered scale immediately below the bottom burners in the preheat and heat zones. This accumulation seems more serious for the heat zone than the preheat zone due to the higher temperatures and larger recirculation zone found below the burners in said zone. The noted phenomena of the top gases interfering with the bottom gases closer to the walls of the furnace will also change the distribution of the scale on the bottom of the furnace. This interaction could push scale sedimentation towards the middle of the furnace as the pieces of fractured scale follow the flow. Sedimentation may then counterintuitively build up on the leftmost side of the supporting structures.

4.3 Temperature Distributions

The temperature distribution for the whole furnace is shown in Fig. 4.3. The contour taken at 180 inches from the furnace centerline shows much more uniform temperatures in each zone. At the centerline, the flames that were forced inward by the top flow at the walls of the furnace is apparent from the high temperature area impinging upon the furnace walls in the preheat zone. The flow of burner products as described in the previous section is readily apparent as well. The flames in the preheat zone are pushed either up or down due to incoming flow from the heat zone. The flames then react and release heat along the top and bottom of the furnace walls. This has potential to reduce the lifespan of the refractory walls but is hard to avoid without changing the entire flow within the furnace.

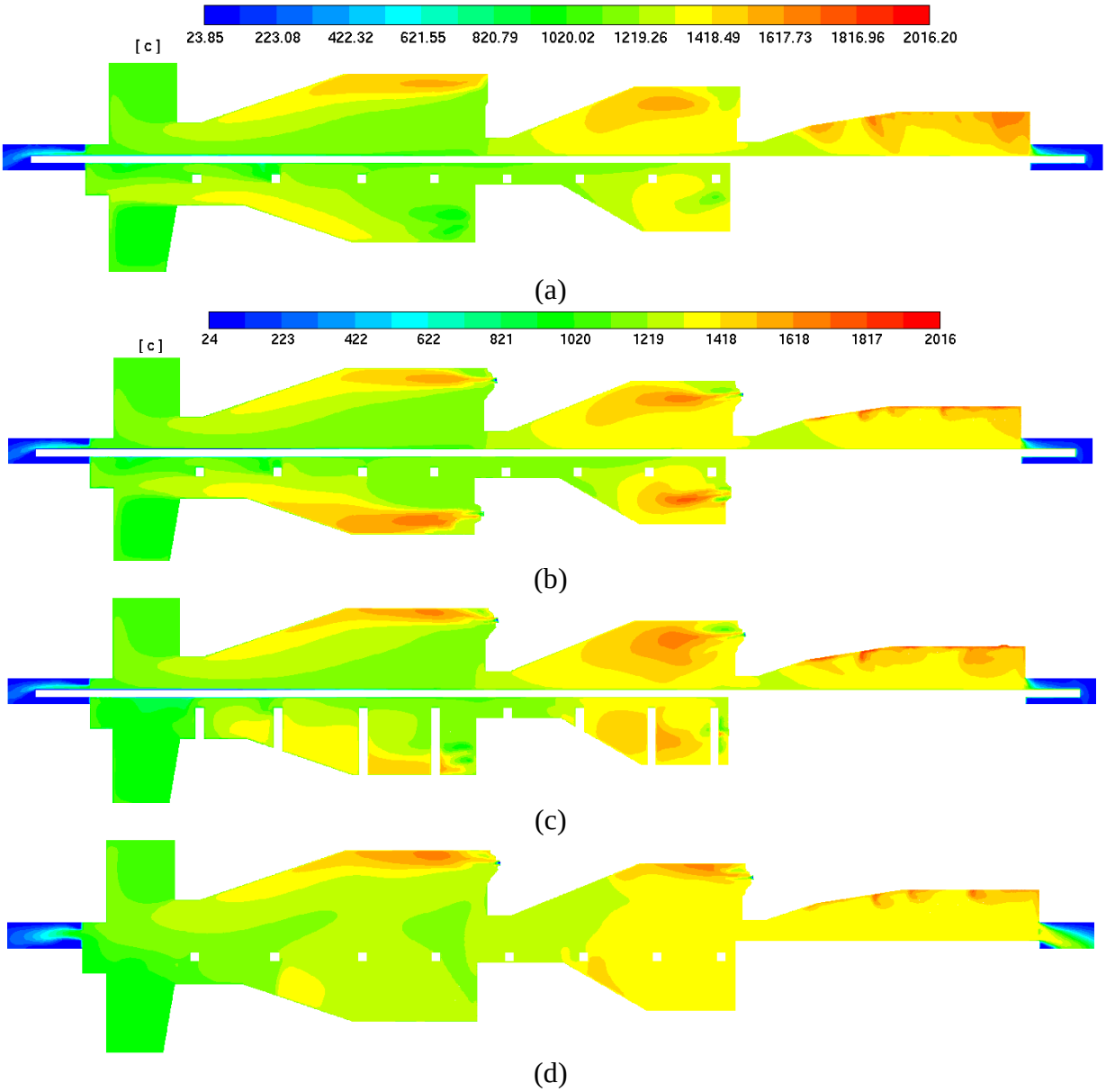

Fig. 4.3 Full furnace temperature contours at (a) the centerline (x = 0), (b) x = 20 in, (c) x = 100 in, and (d) x = 180 in

There are low-temperature areas immediately above or below the burners for the top and bottom respectively due to the recirculation of furnaces gases pulling the flame away from those regions. Fig 4.4 focuses on the temperature distribution along the centerline of the preheat zone burners. High temperature regions are disrupted by the support structure, and the impingement of the bottom flame on the bottom furnace wall is most severe in the middle of the furnace. The high temperature flames for the preheat bottom are closest to the center as well, with further out burners

enable to form similar flame profiles without disruption due to the supporting structures and recirculating air from the top heat zone.

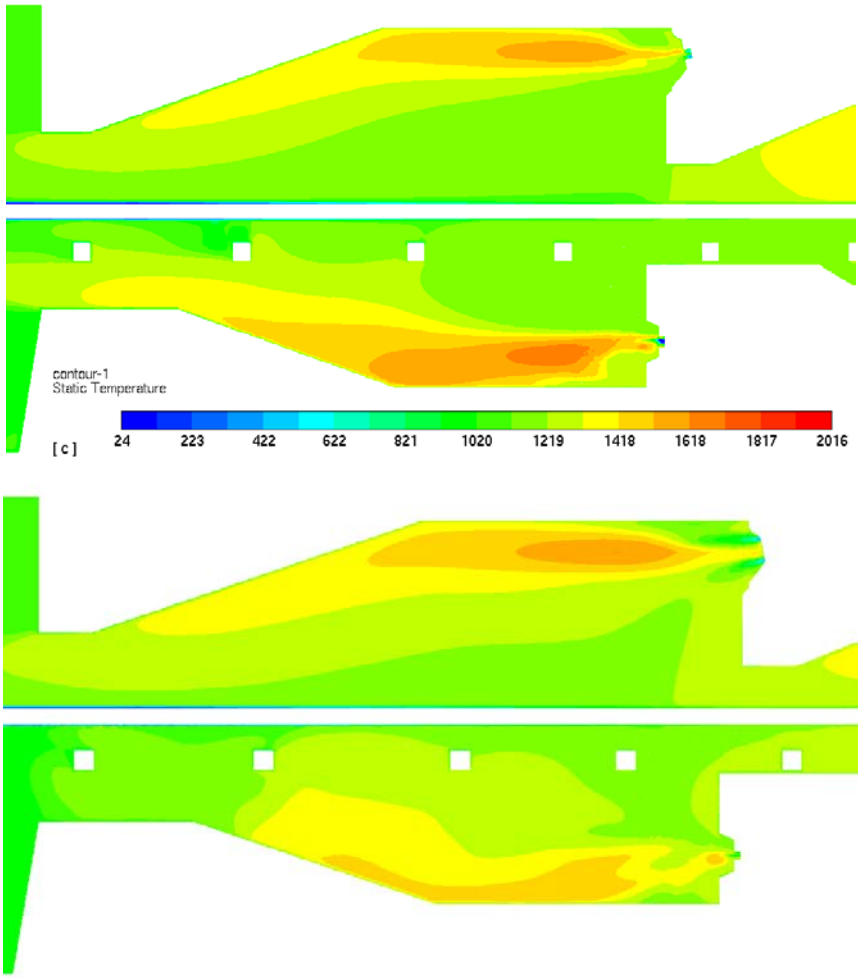

Fig. 4.4 Temperature contour at the middlemost preheat bottom burner (top) and the at the burner closest to the wall (bottom)

For the heat zone bottom burners, there is somewhat unique interaction of the flame with the below burner region as shown in Fig. 4.5. For the middlemost burners, a small recirculation zone seems to have formed below the burner outlet. This has cause the flame to draw downward and part of it to detach from the flame bulk and attach to the furnace wall. The furthestmost burner for this zone, contraire to the preheat zone, can be found to be longer and more fully developed than those flames found in the preheat zone. This may be due to the smaller overall flow in the heat zone compared to the downstream preheat zone. The furthestmost burner also has parts of the flame that are drawn backward along the bottom wall back towards the burner.

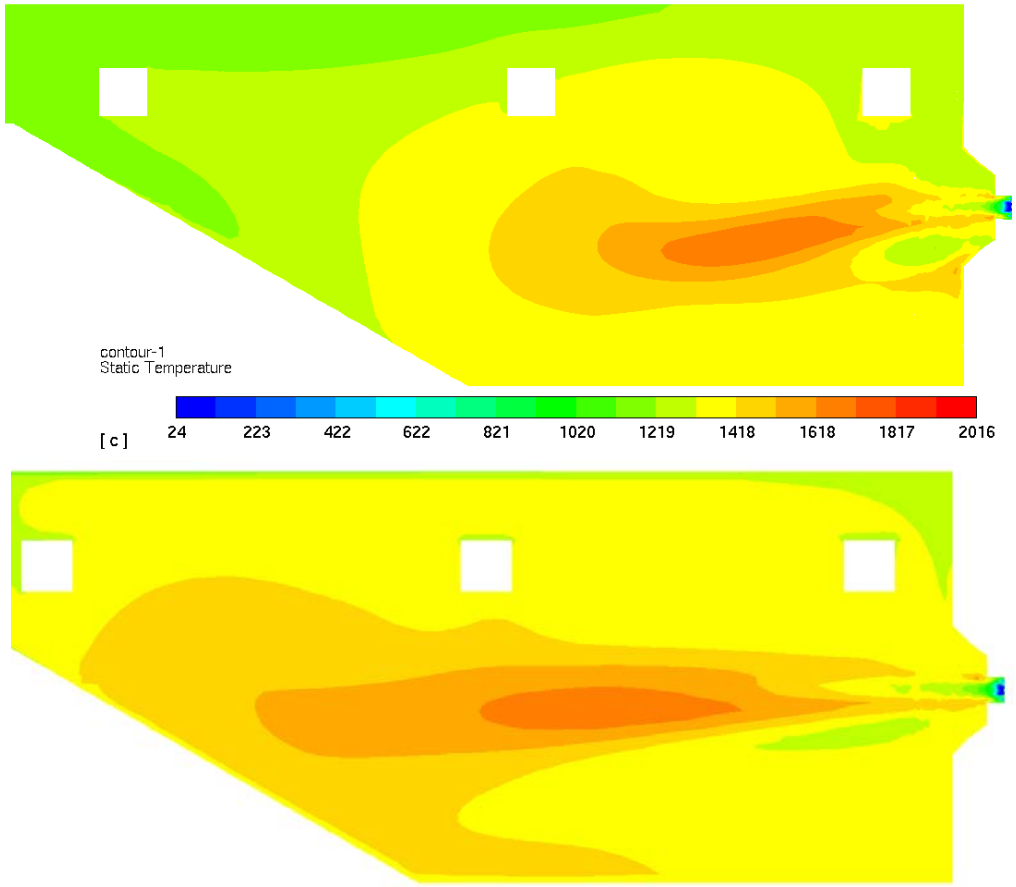

Fig. 4.5 Temperature contour at the middlemost heat bottom burner (top) and the at the burner closest to the wall (bottom)

The soak zone (Fig. 4.6) shows the stereotyical temperature profile of the swirl burner for the large soak burner at the right and for the leftmost small burner. The high-temperature flames hug the top of the furnace walls before impinging down onto the top of the slabs in this zone.

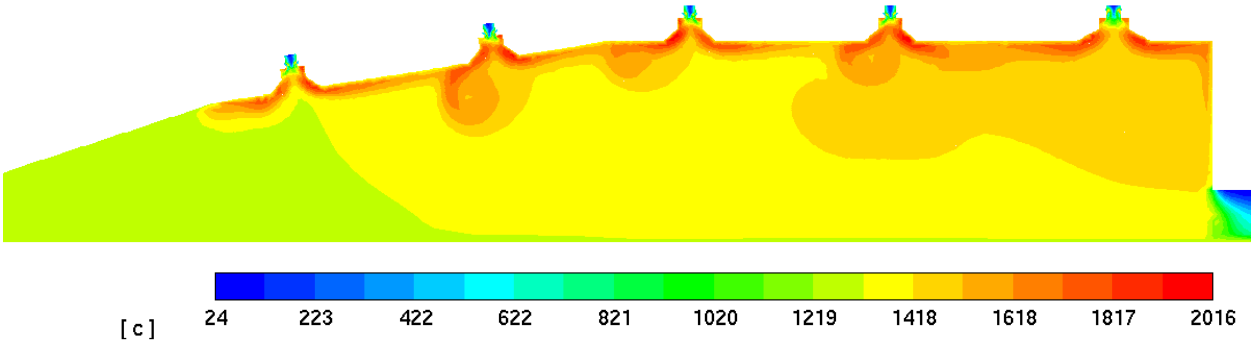

Fig. 4.6 Temperature contour at the middlemost soak zone burners

4.4 Species Distribution

Of interest for these boundary conditions is the amount of excess oxygen in the system. The stoichiometric value of the air/fuel ratio (AFR) by mass is around 17.7, whereas all the zones are running at an AFR around 20. The oxygen mass fraction is shown in Fig. 4.6, which develops in different ways at and away from the centerline. At the centerline, the flame locations in the preheat zone are immediately apparent due to the high oxygen areas that bracket the flames in this zone. Further out, the flames can be tracked from the low oxygen mass fraction regions which are formed due to either fuel (Fig. 4.7b and 4.7c both have good examples of this) or areas of higher combustion efficiency that form regions of relatively high concentrations of water vapor, nitrogen, and carbon dioxide. The latter is prevalent in the soak zone and further away from the centerline. The middle of the furnace near the centerline has a relatively high oxygen content compared to other regions in the furnace. This should result in increased scale formation in these areas.

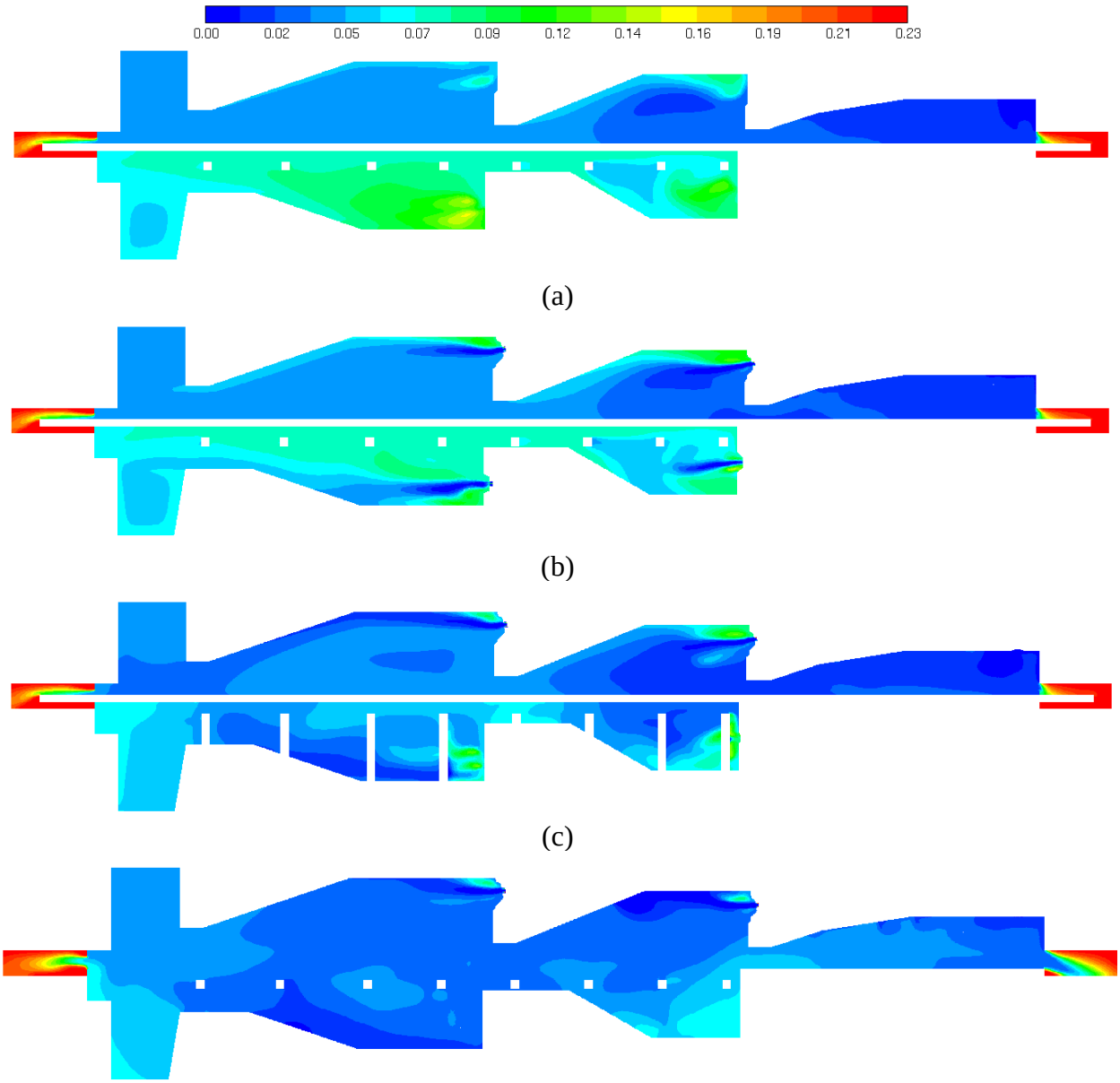

Fig. 4.7 Full furnace oxygen mass fraction contours at (a) the centerline (x = 0), (b) x = 20 in, (c) x = 100 in, and (d) x = 180 in

The flame shape in the preheat zone was visualized as 1% CO mass fraction. The impingement noticed earlier of the flames on the top and bottom of the furnace are further revealed using this visual. Evidently, the furnace gases near the furnace side walls forces the bottom flame up and back. The bottom flames are also more distorted and less predictable than the top preheat flames due to the supporting structures interspersed throughout that region.

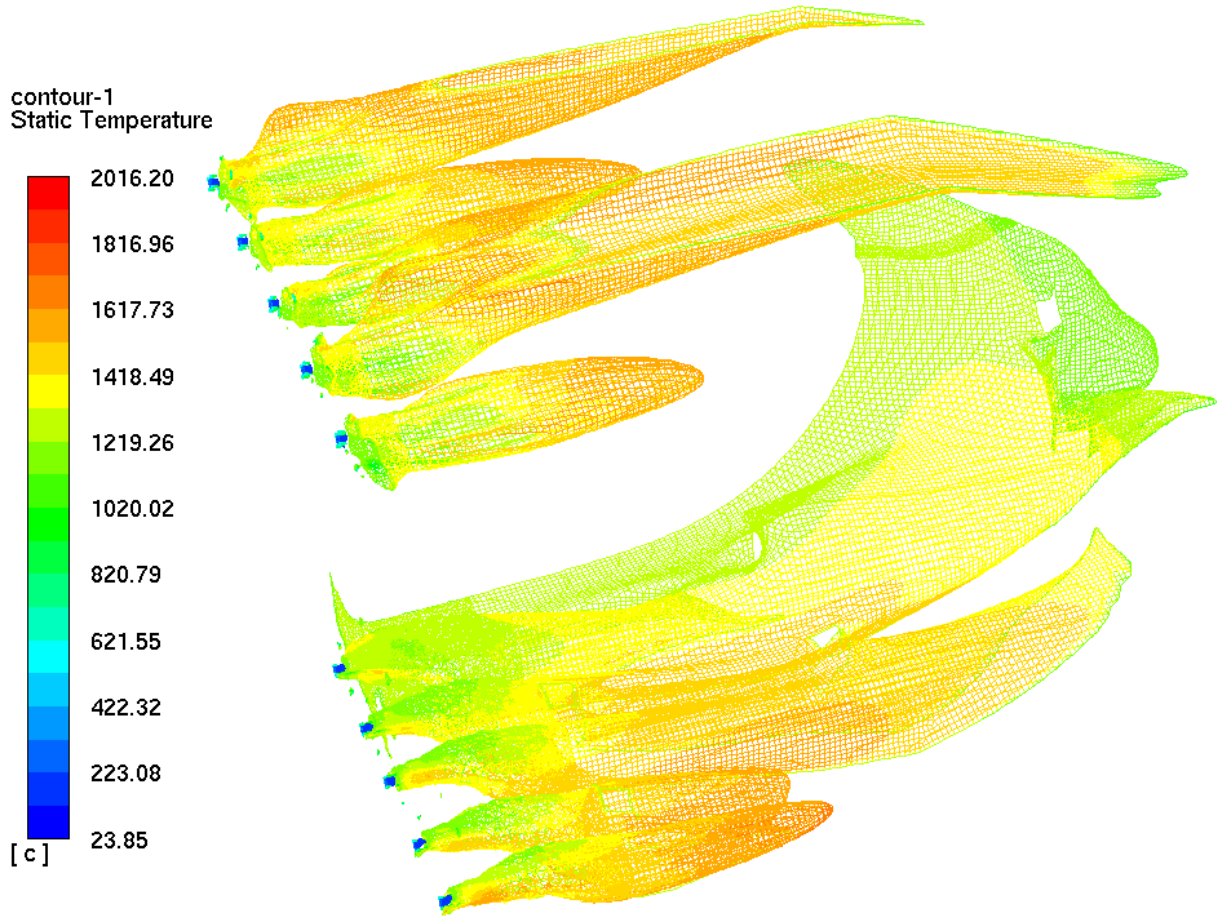

Fig. 4.8 Base case preheat zone flame shapes from center (closest) outward

4.5 Slab Heating Conditions

Fig. 4.7 shows the distribution of heat flux into the flame over the residence time of the slab in the furnace. The slab charge is at the rightmost side and the slab moves from right to left; the centerline of the furnace is marked as such. As such, the highest heat fluxes are found at the top and bottom of the preheat zone. The area between zones where the furnace top wall is lowered causes a small decrease just before each zone, most likely from the top wall of the furnace coming down and reducing the view factor of the radiation. The skidmarks are readily apparent in this figure, as is their shift from the preheat zone to the heat zone. The temperature distribution around the skidmarks is further distorted due to the additional radiative shielding of the supporting structures running from the center of the furnace to the side walls. These structures do not directly touch the slabs, so they only block parts of the incoming radiation. The highest heat flux in the

preheating zone on the top is on the edge of the slab nearest to the wall; for the bottom preheat zone, the highest heat flux is bracketed by supporting structures slightly upstream of the highest slab top heat flux. The top slab may be heated more on the edge furthest from the centerline due to the previously noted phenomena of top zone recirculating flow infiltrating downward into the bottom of the preheat zone. This would pull some of the higher flame shapes lower and increase the convective heat flux in this region. Fig. 4.3d shows the temperature is larger near the slab location nearest to the wall of the furnace due to this infiltration, which supports this explanation.

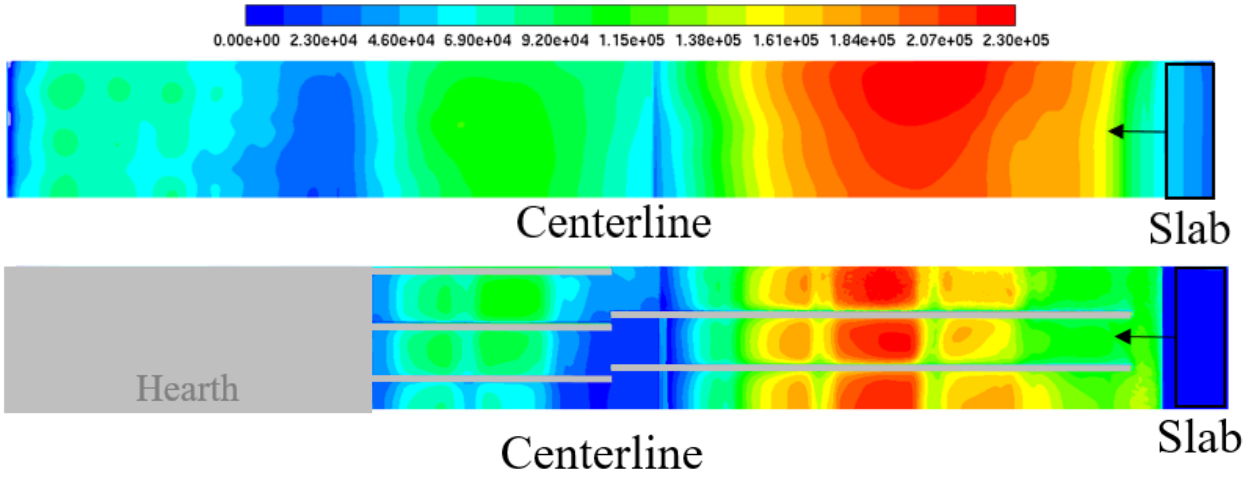

Fig. 4.9 Baseline heat fluxes into the slab for top (top) and bottom (bottom) in W/m^2

The heat zone has a similar heating pattern to that of the preheat zone. The heating is more uniform on the top, however, which may be due to the lack of an upstream zone for the bottom heat zone, which allows for less interferance in the recirculating air there. The bottom heat zone, however, seems to have less heating in the middle of the slab, which may be due to the interference of the skids with the flow development there. The skid shift may have drawn the skids close enough that the radiation is slightly shielded in this region as compared with the preheat zone.

The soak zone has the lowest overall heat flux into the slab. The highesr areas of heat flux clearly show the location of the down-facing top burners. Immediately upon exiting, the heat flux goes less than zero watts per area, which implies heat loss upon the door opening and the heated slab leaving the furnace is immediate and severe.

Looking at Table 4.1, it is obvious yet again that the highest amount of heating occurs in the preheat zone (>50%). The preheat zone has been split into the preheat and recuperative zones

to attempt to reflect the impact of convection on the earliest slab heating. If they were to be combined, then the slab will have received over 70% of the total heating as it reaches the heat zone. The amount of heat transfer from radiation increases throughout the furnace from the recuperative zone to the soak zone, resulting in an overall radiation heat transfer amount of the total heat transfer to be 91.5%.

Table 4.1 Baseline heat transfer into the slabs by zone

Zone	Zone Heat Transfer (W)	Radiation Heat Transfer (W)	Radiation HT of Zone	Zone HT of Total
Recuperative	5.10E+06	4.32E+06	84.7%	20.2%
Preheat	1.26E+07	1.15E+07	91.0%	50.2%
Heat	5.07E+06	4.89E+06	96.5%	20.1%
Soak	2.39E+06	2.36E+06	98.6%	9.5%
Total	2.52E+07	2.31E+07	91.5%	--

4.6 Scale Formation

Parameters used by the scale formation model have been tabulated for each zone in Table 4.2. These values were taken from the cells immediately adjacent to the slab walls. There is an interesting trend of increasing water vapor as the slab travels through the furnace. The pressure also drops from the recuperative zone to the soak zone. The velocity is highest in the preheat zone, which may be due to having the highest input flow from subsequent sections as well as from the burners overall. As is the intention of the reheat furnace, the gas temperatures near the slab in each zone increase by 100-200°C for each zone.

Table 4.2 Baseline scale formation parameters per zone

Parameters	Recup.	Preheat	Heat	Soak
Temperature (°C)	986.01	1106.16	1294.29	1338.62
Velocity (m/s)	3.925	6.360	3.315	3.235
O_2 vol%	3.922	3.965	3.080	2.166
H_2O vol%	14.392	14.897	15.647	16.423
CO_2 vol%	7.507	7.489	7.692	7.909
Pressure (Pa)	93.69	72.16	65.76	60.72
Density (kg/m^3)	0.27472	0.24774	0.21598	0.20882
Viscosity (kg/m-s)	1.72E-05			

Looking at the kinetic parameters listed in Table 4.3, there is a clear increase in the parabolic rate constant with time. The parabolic rate constant is entirely dependent on temperature, so this makes perfect sense. The linear rate constant is related to the gas phase parameters. It decreases throughout the furnace, only increasing from the recuperative zone to the preheating zone. Of note is that the contributions of the linear rates constants from water vapor and carbon dioxide were minimal until the soak zone.

Table 4.3 Baseline scale formation kinetics per zone

Zone	**k_p (cm^2/s)**	**k_l (cm/s)**
Recup.	1.87E-06	4.32E-05
Preheat	5.42E-06	5.71E-05
Heat	1.97E-05	3.3E-05
Soak	2.53E-05	2.31E-05

In Fig. 4.10, the average slab scale thickness with time is shown. The growth almost seems linear, with small dips between the various zones. Overall, the scale thickness was 0.22 cm at 160 min. This is roughly equivalent to 0.087 inches, which is 1.76% of the thickness of the steel slab in this reheat furnace. This number falls within the given range of 1-2% of steel yield lost to scaling given earlier [8].

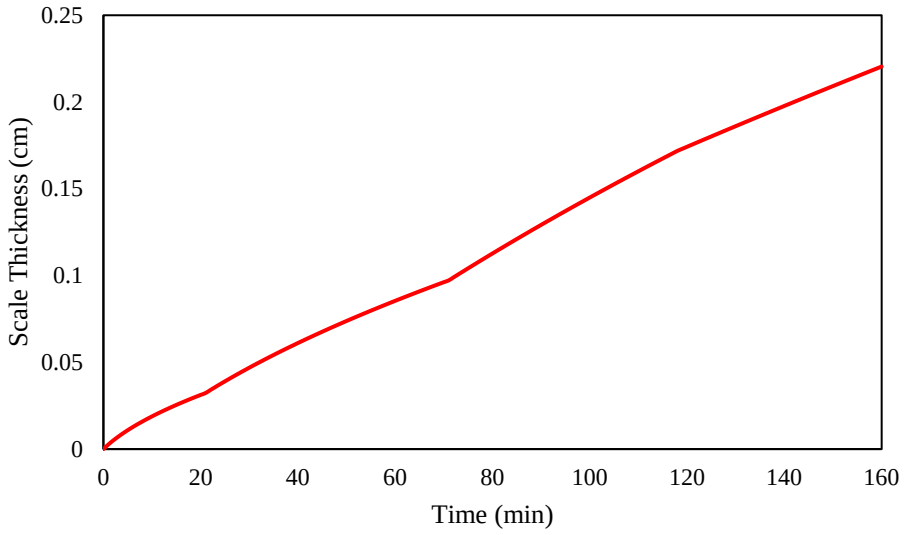

Fig. 4.10 Scale formation with time for the baseline case

5. INVESTIGATION OF APPLICATION OF OXYGEN ENRICHED COMBUSTION

5.1 Oxygen Enriched Combustion

Oxygen enrichment, or oxygen enriched combustion (OEC), as previously discussed, is realized through the reduction of nitrogen from air until the desired oxygen content is acquired. Fig. 5.1 shows the immediately apparent benefit of higher levels of oxygen enrichment by showing the stoichiometric analytical volume composition of methane and an oxidant. As the molar oxygen increases, the nitrogen steadily decreases towards zero. With this, the product gases are two thirds water vapor and one third carbon dioxide. The water vapor can then be condensed out and all carbon dioxide collected and stored. Water vapor and carbon dioxide are also radiating species whereas nitrogen is not.

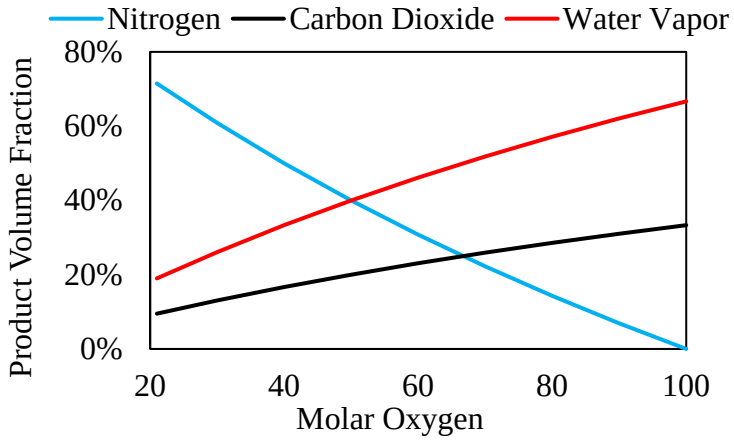

Fig. 5.1 Effects on oxygen enrichment on species compositions

Another benefit of oxygen enrichment is also directly due to the reduction of nitrogen. Energy that would have gone to heat the relatively inert nitrogen up to the temperature of the product gases is now able to continue to heat said product gases. In terms of adibatic flame temperature, much higher flame temperatures can be reached. With the higher flame temperatures and higher concentrations of radiating species, the radiation heat transfer is highly enhanced.

The largest issue for oxygen enrichment is then directly related to this higher flame temperature. The higher the temperatures goes, the more NO_x will be formed. In order to avoid NO_x formation while still utilizing the benfits of oxygen enrichment, the reaction must be delayed.

A delayed reaction will release less heat in one area at a given time. Usually this delayed reaction is accomplished through higher momentum jets to promote the entrainment of furnace gases as shown in Fig. 5.2. Alternatively, staged combustion is also possible, where the oxidant is fed to the fuel in stages.

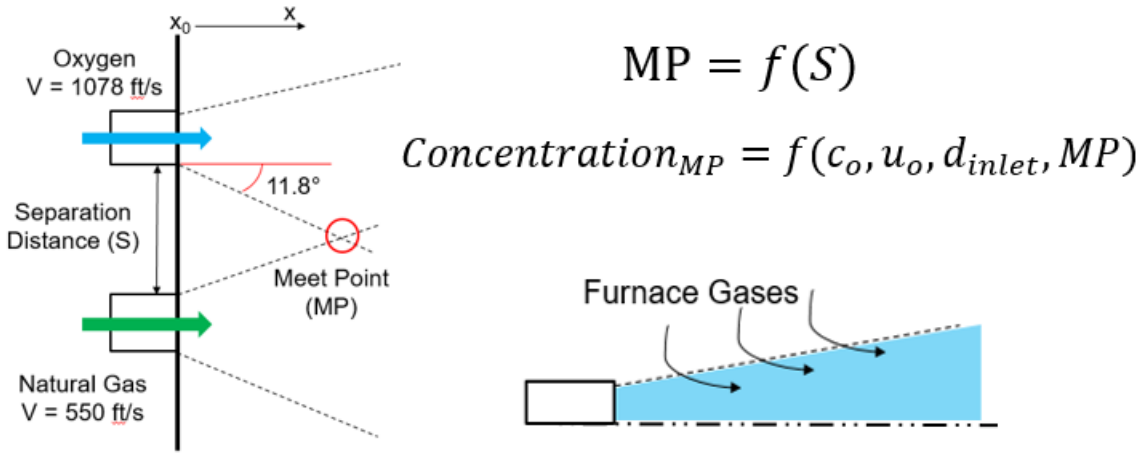

Fig. 5.2 Method of delaying high-temperature reaction for reduced NO_x formation

In Fig. 5.2, the formulae shown are for the meeting point of the two jets shown, which is a function of the distance separating said jets. The concentration at the meeting point is a function of the inlet concentration, c_o, the inlet velocity, u_o, the inlet diameter, d_{inlet}, and the meeting point distance. The entrainment of furnace gases dilutes the flow to decrease the concentration of reacting species in order to lower the mixing efficiency of said species.

5.2 Boundary Conditions

The oxygen enrichment in this study is only applied in the preheat zone. There are a few reasons why that pertain back to the combustion and to the scale formation. Scale formation is typically quite small in the preheating zone, so the higher concentrations of oxidizing species in this zone is less of a concern. This zone also uses the most fuel, so a reduction in fuel usage realized in this zone would be the best outcome. Finally, the flow from the soak and heat zones will further dilute the unique atmosphere found in the preheat zone due to the application of oxygen enrichment.

After discussion with industrial collaborators from Praxair, the case parameters were developed as shown in Table 5.1. The oxygen contents discussed in this work are a medium oxygen

enrichment of 46 vol% oxygen and a 100% oxygen oxy-fuel case. For these cases, higher momentum was required for the oxidant as well as the fuel for the oxy-fuel case. The total amount of oxygen and fuel going into the preheat zone is unchanged; only the nitrogen is removed.

Table 5.1 Baseline heat transfer into the slabs by zone

Case	Oxygen Content (%)	Oxygen/Fuel Ratio	Velocity (ft/s)			
			Prim. Air	Sec. Air	O_2	Fuel
1	21%	2.51	430	270	--	120
2	46%		130	80	1080	120
3	100%		--	--	1080	550

For the burner configurations, there were some changes necessary to reach the desired velocities and dilutions for each type of oxygen enrichment. For the medium oxygen enrichment case, the oxygen is added to the zone through lances between the normal air-fired burners. This will result in a drastic change in the flow between the burners, especially at the bottom. For the oxy-fuel, the entire burner face was replaced by an oxygen and a fuel inlet port at a distance of 5 inches to promote entrainment before ignition. The oxygen port is closer to the closest wall than the fuel port, which will always be closer to the center of the furnace than the oxygen port.

5.3 Effects on Velocity Distribution

The oxygen enrichment was only applied in the preheat zone, which is downstream of the rest of the domain. As such, only the changes in the preheat zone are discussed here.

For the preheat zone in the medium oxygen enrichment case, the largest difference from the baseline case is the lack of a large recirculation zone in the top preheat zone (see Fig. 5.3). Instead, there is a much smaller zone immediately where the flow from the subsequent heat zone comes in. This is most likely due to the very high momentum oxygen jets that are interspersed between the air-fired combustion burners. At the centerline for the top figure in Fig. 5.3, these oxygen lances can be seen in both the top and bottom preheat zones due to the very high velocities. Unlike the top preheat zone, the bottom preheat zone has developed a much larger recirculation zone than the base case. It seems to be a combination of two recirculation zones from the base line case.

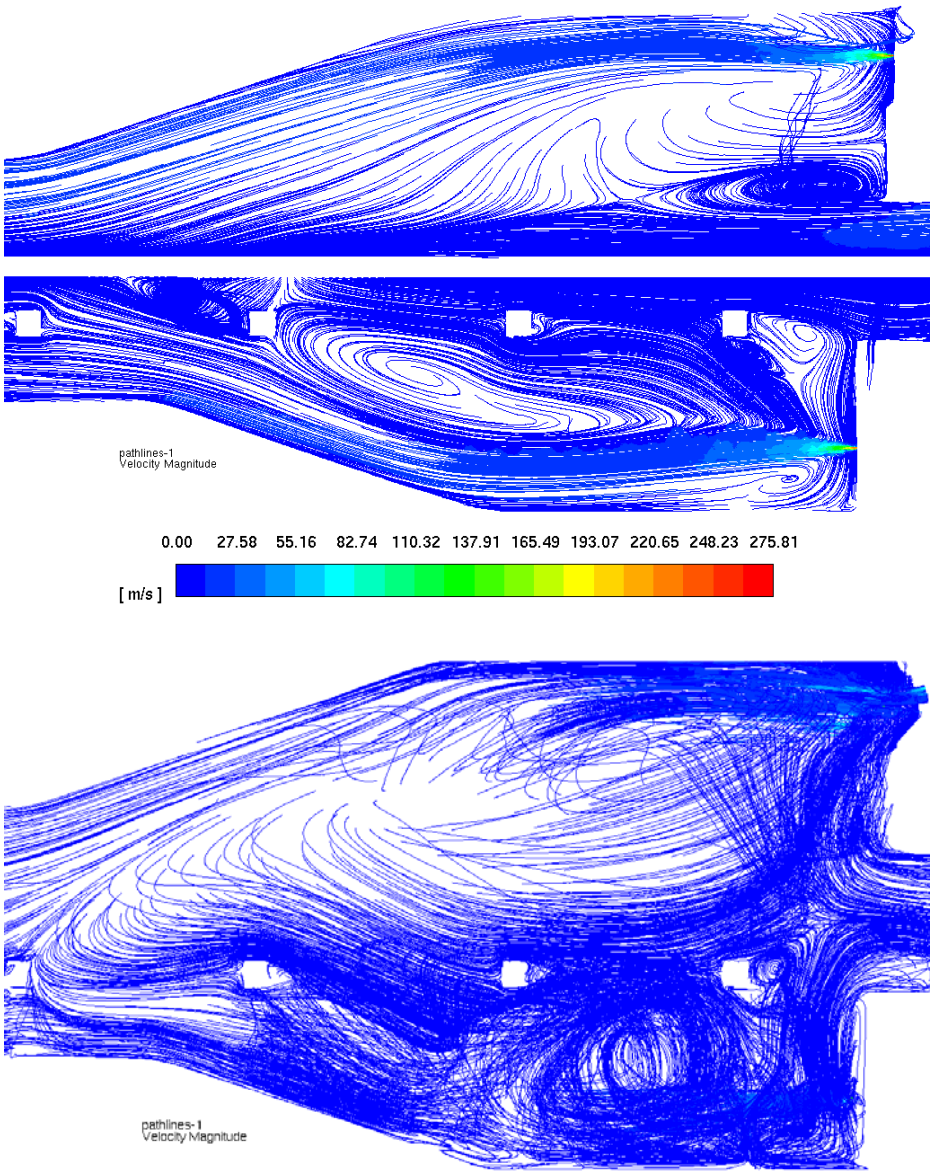

Fig. 5.3 Pathlines colored by velocity at the centerline (top) and at the furthest from center top burner (bottom)

Away from the centerline, shown in the bottom figure of Fig. 5.3, the flow is quite different than that from the baseline case. The top preheat zone seems to have developed a very large zone of recirculating air that dips down into the bottom preheat zone sooner than in the base case. The supporting structures within the furnace seem to buffet the flow around them. Compared to the centerline of the medium oxygen enrichment case, this flow is much more disordered.

Looking now at the oxy-fuel case, somewhat similar trends are seen near the centerline (see top in Fig. 5.4). There is a small recirculation zone below the burner and above the slab in the

top preheat zone, whereas the bottom preheat zone has a somewhat askew recirculation zone. However, unlike the medium oxygen enrichment case, moving further from the centerline yields a very strong upper recirculation zone that is nearly fully merged with that found in the bottom zone. Leaving these highly recirculating flows seems to be a matter of hitting one of the furnace walls or supporting structures, or of moving inward toward the center of the furnace.

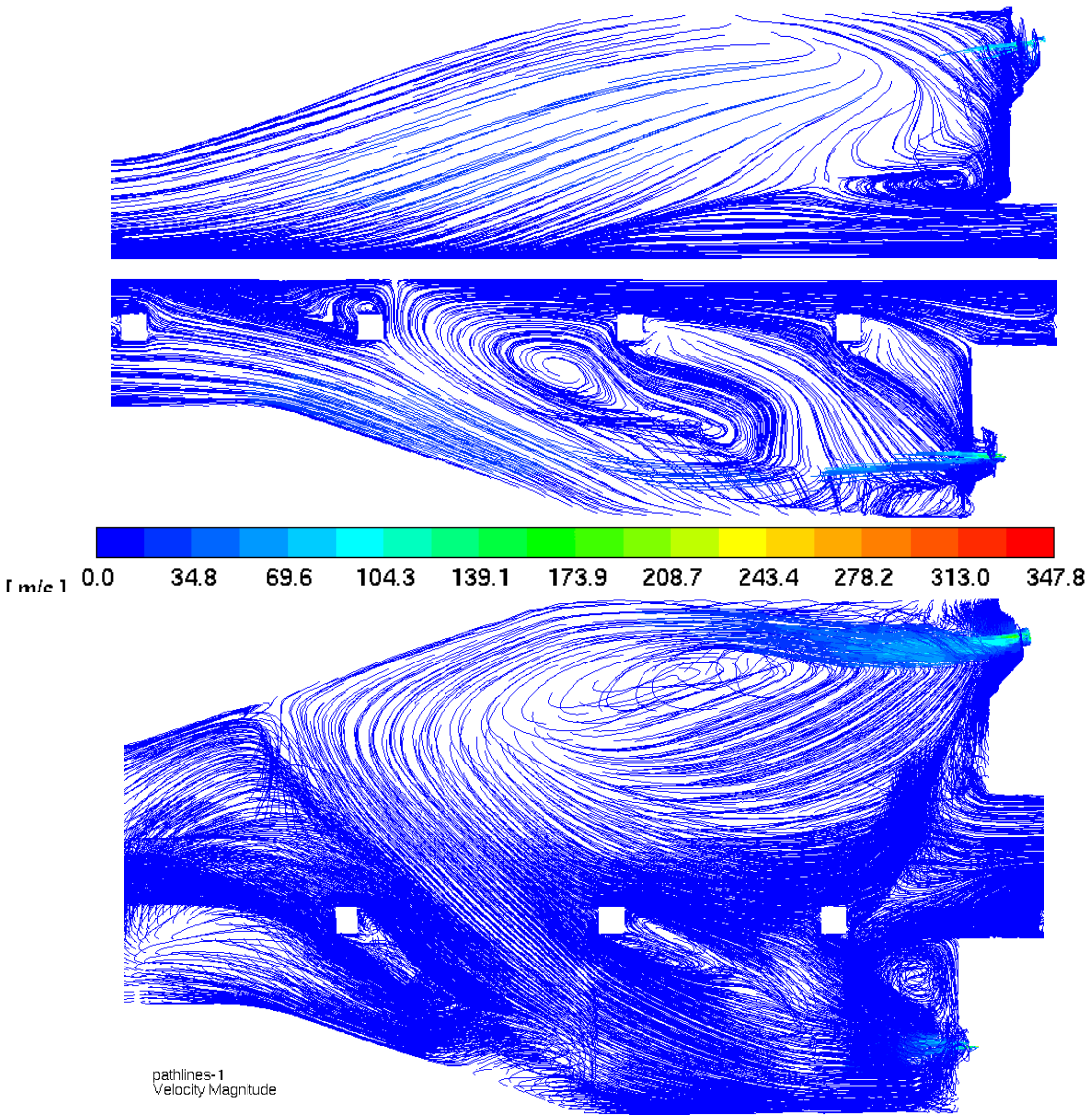

Fig. 5.4 Pathlines colored by velocity at the centerline (top) and at the furthest from center top burner (bottom)

In terms of possible scale accumulation, these flows would distribute the spalled-off scale in somewhat different locations. Scale falling near the outer edges of the medium oxygen

enrichment burners would be pushed inward and may accumulate either between supporting structures organized in the direction of slab movement or along the burner axial direction due to the high momentum jets now interspersed between each burner. For the oxy-fuel case, scale accumulation may continue to occur immediately below the burners and between burners due to the lack of jets in these regions. Accumulation on the bottom of the reheat furnace where the bottom wall begins to incline upward is very likely due to the changes in flow found here, especially further from the centerline of the furnace.

5.4 Effects on Temperature Distributions

The temperature distribution for both the medium oxygen enrichment and oxy-fuel cases are very different than the baseline case due to the higher level of oxygen in the reactants and in the change in momentum throughout the preheat zone.

For the preheat zone in the medium oxygen enrichment case, the centerline temperature distribution is shown in Fig. 5.5. Compared to the baseline case, the maximum temperature is 373.2°C higher. The flames are much longer and wider on both the bottom and the top. This is more noticeable for the bottom compared to the base case. The high-temperature, reacting flow is pushed upward in the top preheat zone and may cause more damage then found in the base case. The bottom flow, however, only impinges on the bottom of the furnace once the furnace floor begins to incline upward.

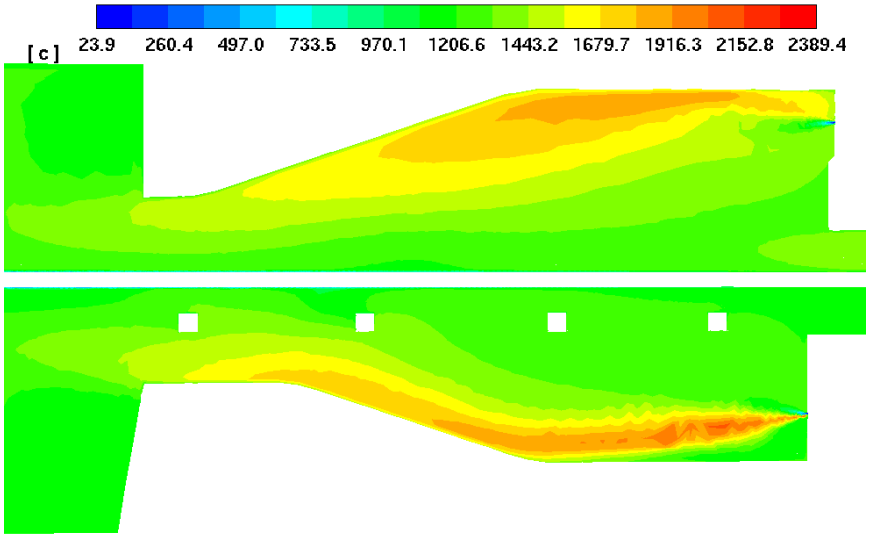

Fig. 5.5 Full furnace temperature contour at the centerline for medium OEC

Following the top preheat zone as we move from the burner closest to the centerline outward in Fig. 5.6, we can see that the high temperature area in these regions starts to shrink and drawback. As these contours are in line with the centerline of the burner instead of the high velocity oxygen jets between each burner, then this makes a lot of sense. The high temperature area should be found between the burner and the oxygen jet and is no longer centered on the direction of the face of the burners.

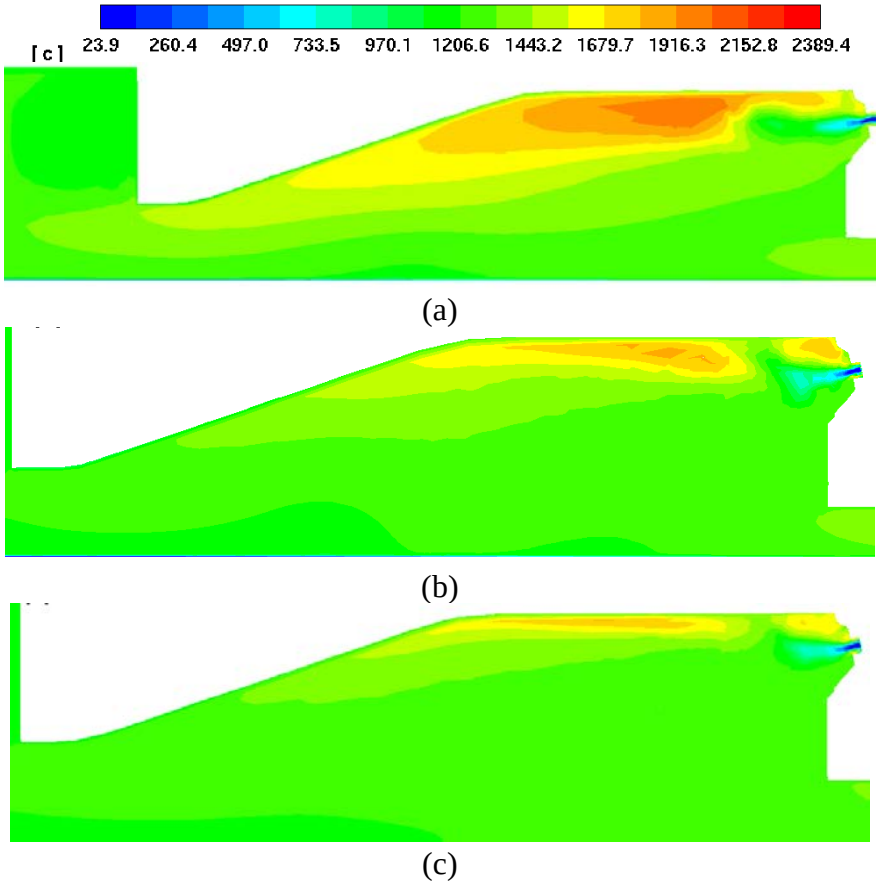

(a)

(b)

(c)

Fig. 5.6 Top preheat zone temperature contours for medium OEC at (a) the closest burner to the centerline, (b) the middlemost burner from the centerline, and (c) the furthest from center burner

The temperature distribution of the preheat zone bottom tells a similar story, with the high temperature zone almost interrupted or nonexistent until the fuel and air from the burner mixes with that of the oxygen from the oxygen lance. See fig. 5.7 for details.

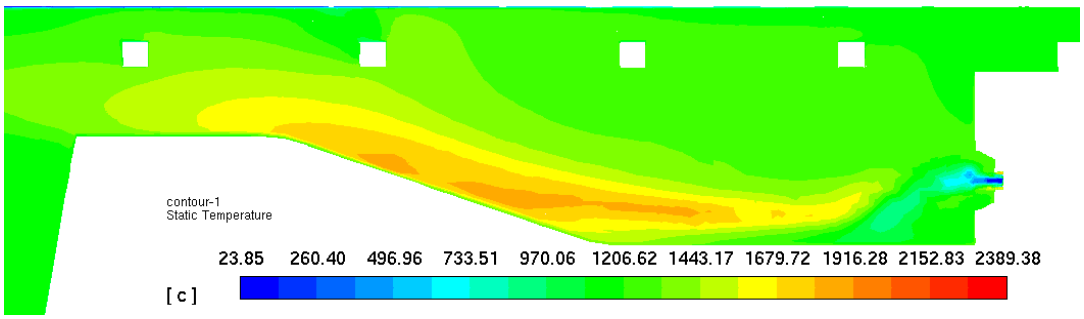

(a)

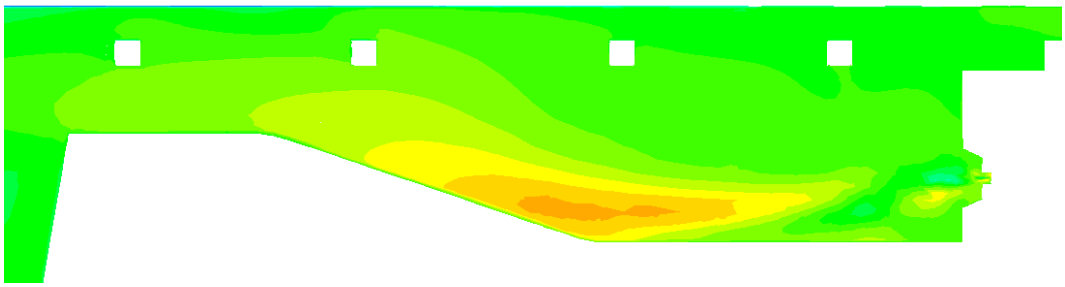

(b)

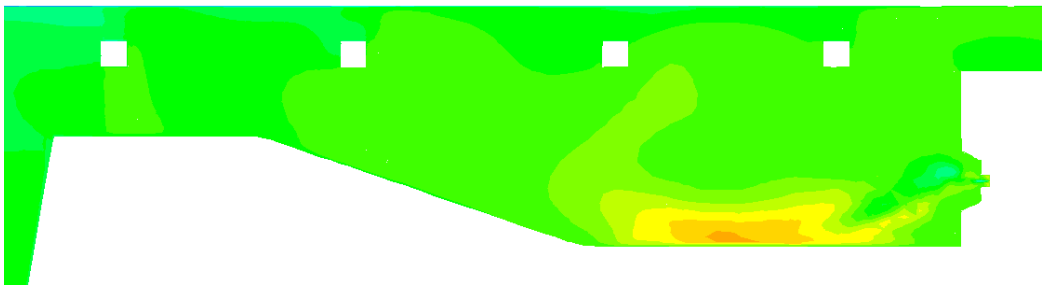

(c)

Fig. 5.7 Top preheat zone temperature contours for medium OEC at (a) the closest burner to the centerline, (b) the middlemost burner from the centerline, and (c) the furthest from center burner

For the preheat zone of the oxy-fuel case, the centerline temperature distribution is seen in Fig. 5.8. The maximum temperature is now 588°C higher than the base case. Compared to the baseline case, the high-temperature area no longer hugs the top of the furnace, but instead is pushed to the middle of the zone. As the fuel and the oxygen are at much higher velocities in this case, the momentum is high enough to overcome the incoming flow from subsequent zones. Even the bottom preheat zone does not fully hug the bottom of the furnace.

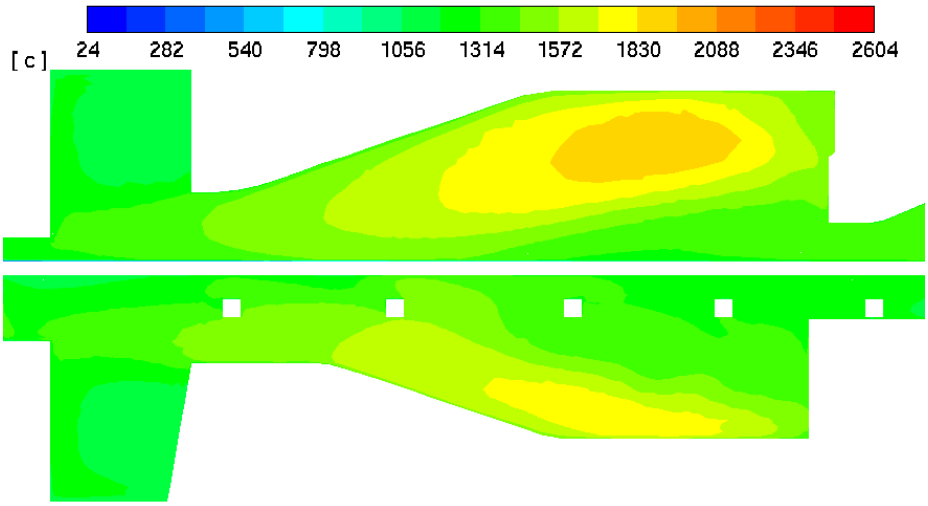

Fig. 5.8 Full furnace temperature contour at the centerline for oxy-fuel conditions

Along the burner centerlines, shown in Fig. 5.9, this trend of a lower high-temperature area than the base case continues from the centerline outward. The outermost top burner does eventually hit the top of the furnace, but the length of the flame touching the top is still much smaller than found in the base case at this same location. The bottom preheat zone shows similar trends due to the increased momentum for both zones.

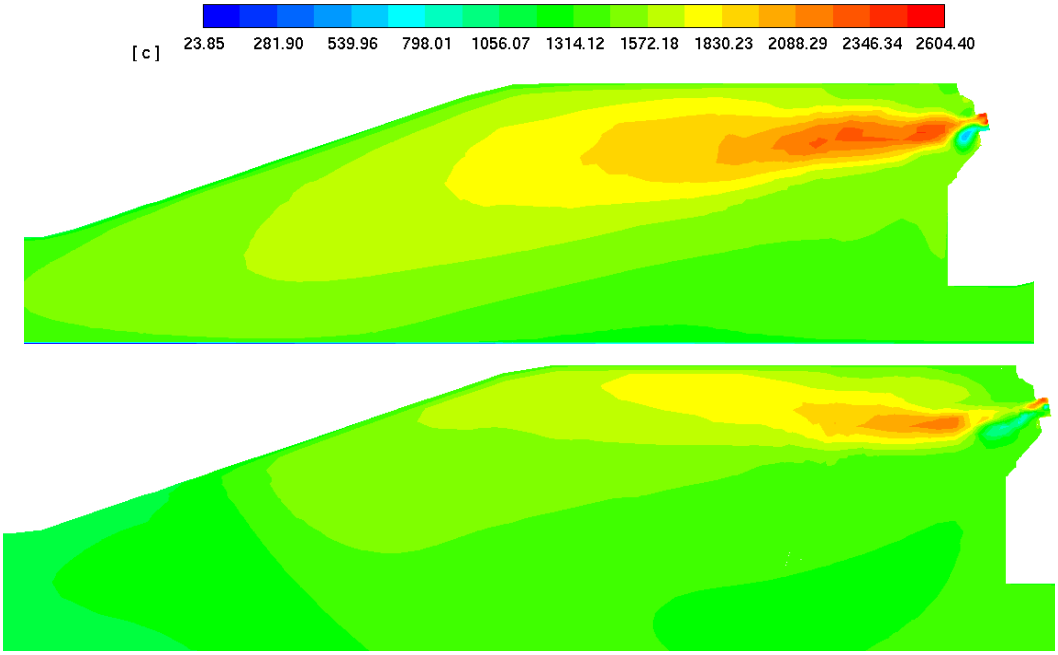

Fig. 5.9 Top preheat zone temperature contours for medium OEC at the closest burner to the centerline (top) the furthest from center burner (bottom)

Comparing temperature distributions of the base case with the medium oxygen enrichment case and the oxy-fuel case necessitates the same end points for the coloring of the contour. Constraining these end points by the minimum and the maximum temperatures found in the baseline case shows how different the temperature distributions at the centerline really are, exemplified in Fig. 5.10. The higher temperatures in the medium oxygen enrichment case and the oxy-fuel case could lead to higher levels of NO_x production or cause the life of parts of the furnace to be lowered.

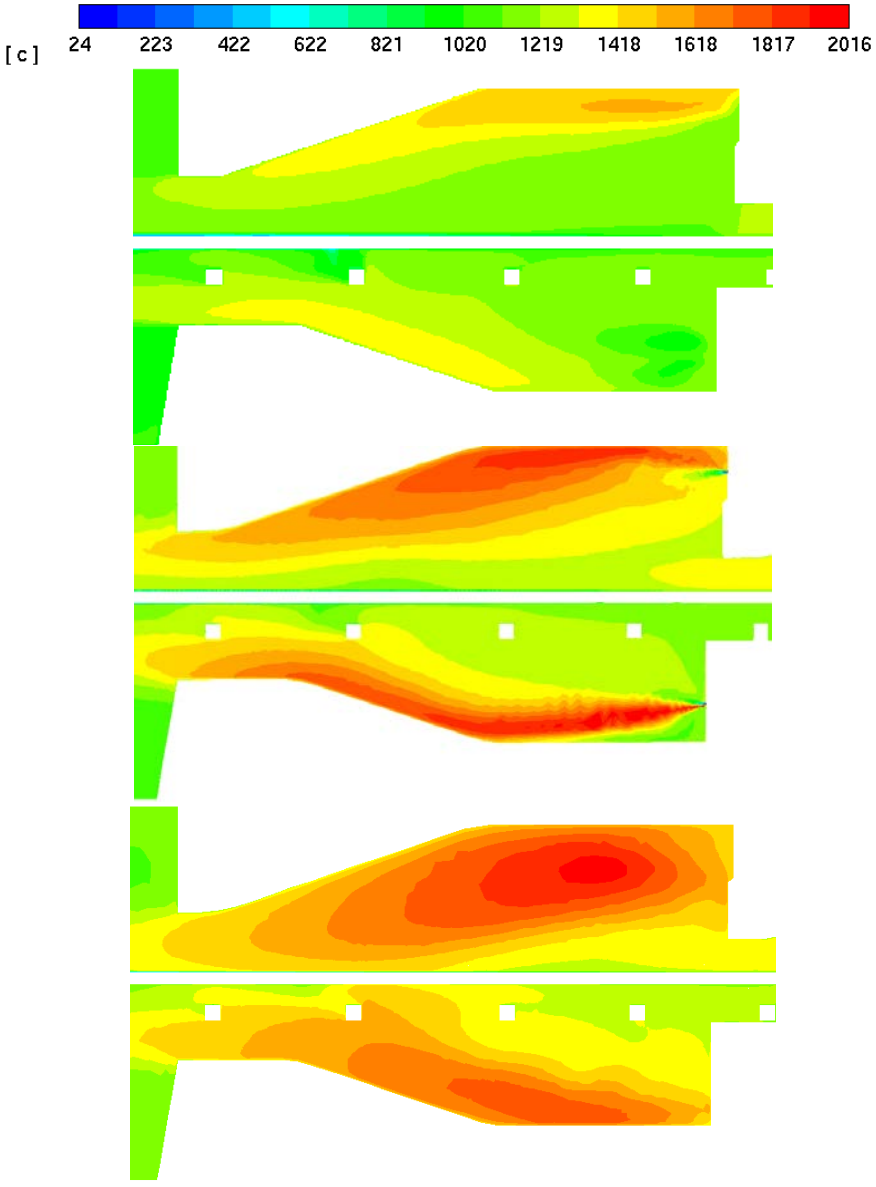

Fig. 5.10 Preheat zone centerline temperature contours for the base case (top), medium oxygen enrichment case (middle), and the oxy-fuel case (bottom)

5.5 Effects on Species Distributions

Looking at the oxygen mass fraction distribution for the medium oxygen enrichment case in Fig. 5.11 (top), we can see the oxygen lances immediately. Again, these contours have been bracketed by the limits of oxygen mass fraction found in the base case. Compared to the baseline case, both of these contours show higher levels of oxygen mass fraction – a large part of which is due to the reduction of nitrogen in the preheat zone. There are some differences that cannot be attributed to the lack of nitrogen, however. For the medium oxygen enrichment case, a clear band of nearly no oxygen is apparent at the top and bottom walls of the furnace. This may be due to the effect of the different momentum given by the burners and oxygen lances on the flow. For the oxy-fuel case, the bottom preheat zone has another area with nearly no oxygen in it. For both of this cases, the recirculating flow in the bottom preheat zone may cause these areas to become dearth of oxygen.

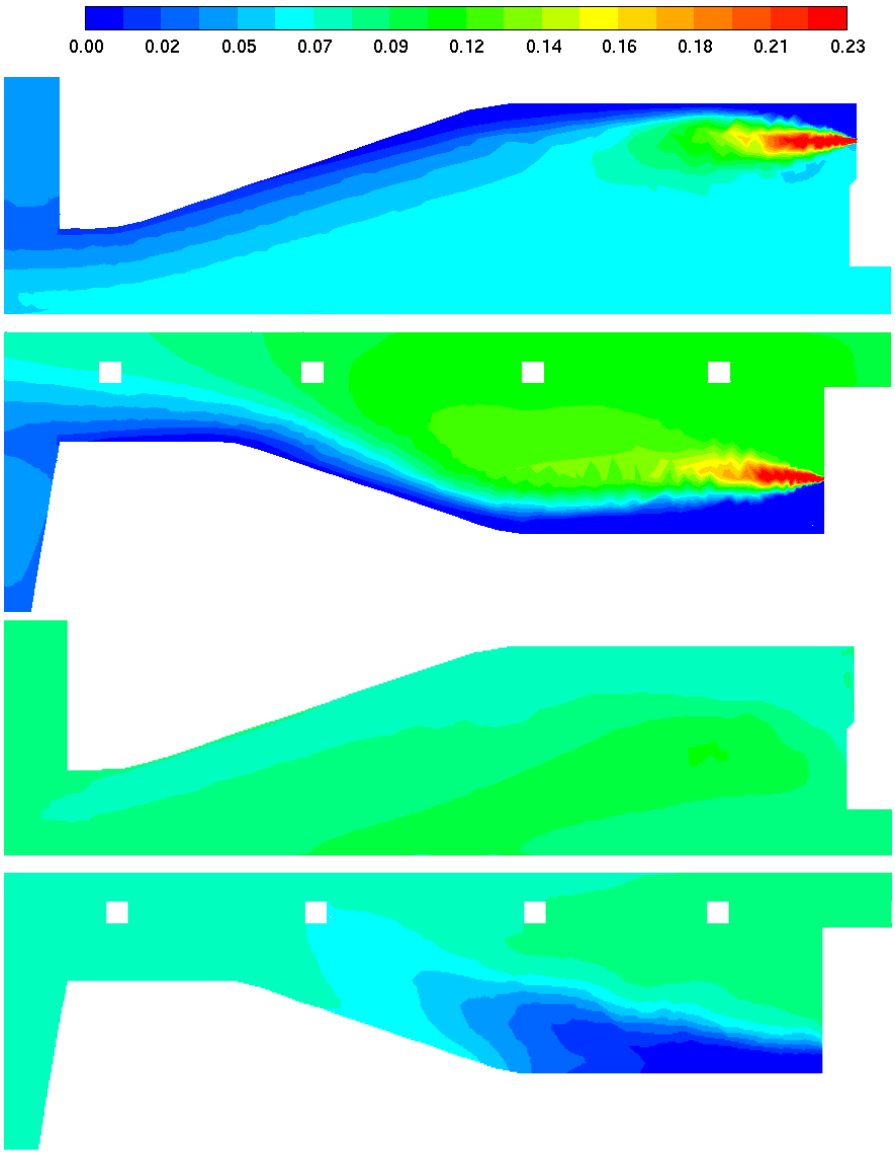

Fig. 5.11 Preheat zone oxygen mass fraction contours at the centerline of the furnace for medium oxygen enrichment (top) and oxy-fuel (bottom) cases

The flame shapes for the medium oxygen enrichment case and the oxy-fuel case are shown in Fig. 5.12 and 5.13 respectively. These flames, as before, are shown via a 1% CO mass fraction iso-surface and colored by temperature. The baseline case was found to have the longest flames on the bottom be near the edges of the preheat zone, and at different areas in the top preheat zone. For the medium oxygen enrichment case, the flames in the top and bottom zones are much more uniform and attached to each other due to the oxygen lances between burners. The top zone has a similar trend of slightly longer flames in two locations as the baseline case, but they are still much

shorter than those found in said baseline case. The bottom preheat zone has a reverse trend than the baseline case with the longest flame near the centerline of the burner and getting smaller as it travels outward. These flames are also more connected, but supporting structures still seem to disrupt the flow.

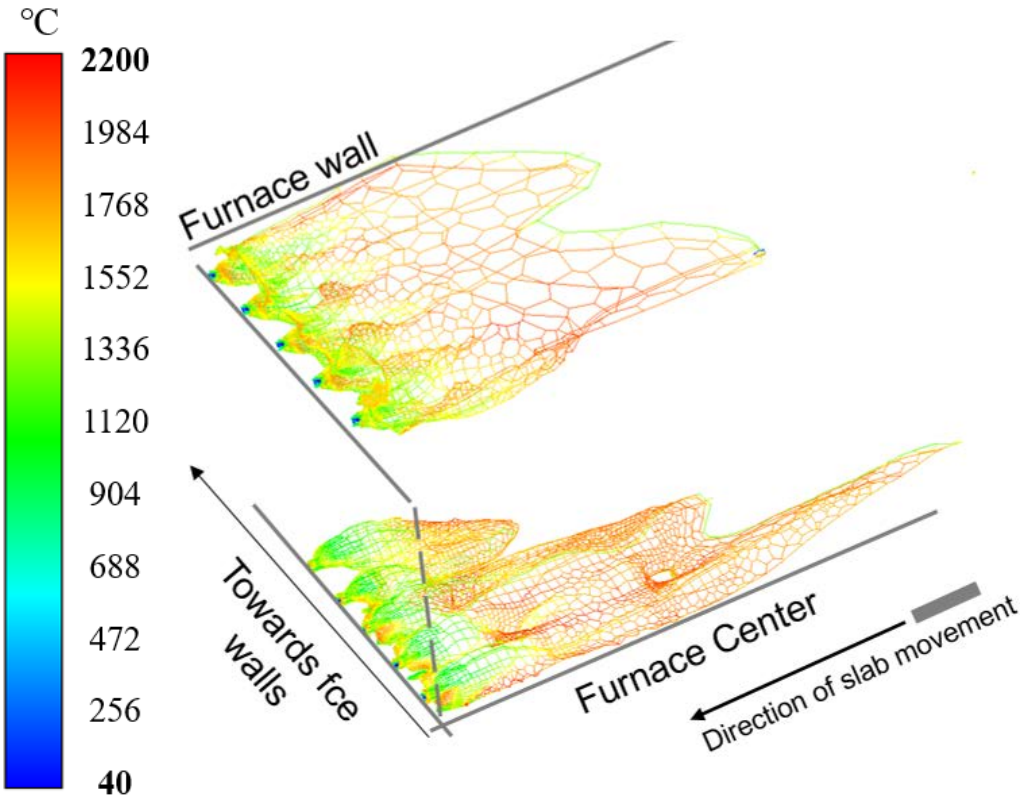

Fig. 5.12 Medium oxygen enrichment case preheat zone flame shapes from center (closest) outward

The oxy-fuel case shows much shorter flames than both the baseline and the medium oxygen enrichment case (See Fig. 5.13). The flames found in the oxy-fuel case are almost all not attached to the top and bottom of the furnace, and seem to have a more uniform shape distribution when compared flame-to-flame.

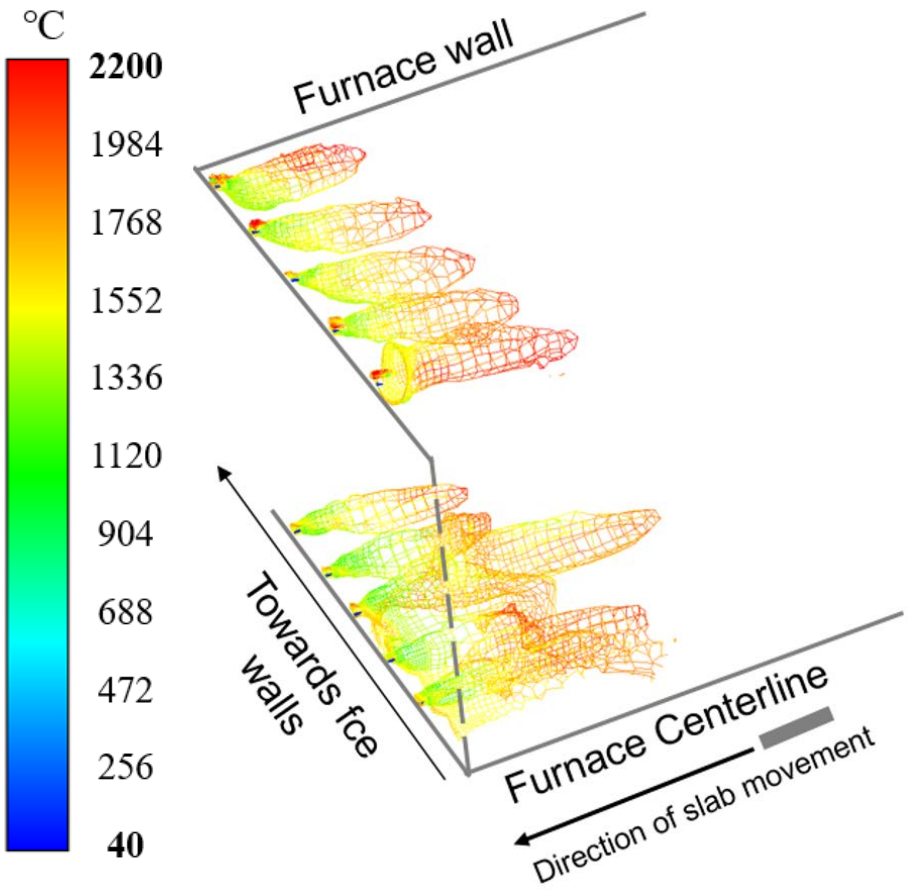

Fig. 5.13 Oxy-fuel case preheat zone flame shapes from center (closest) outward

5.6 Effects on Slab Heating Conditions

Looking at the slab heating characteristics, the heating in the preheat zone is much more intense. Fig. 5.14 shows the distribution of the heating on the slab surfaces. Contrary to the baseline case, the most intense heating is near the middle for both the top and bottom of the slab surfaces. For the medium oxygen enrichment preheat zone bottom, we can see the flames are longer near the centerline of the furnace, which would lead to a more intense hot spot there. For both top and bottom heating, there is no longer flow and flame interaction at the edges of the furnace. This allows the flames to be straighter and for the flow hot flow not impact the edges of the slab furthest from the centerline. Without this impingement and enhanced convective heat transfer, the spot of highest heating lies in the middle of the slabs.

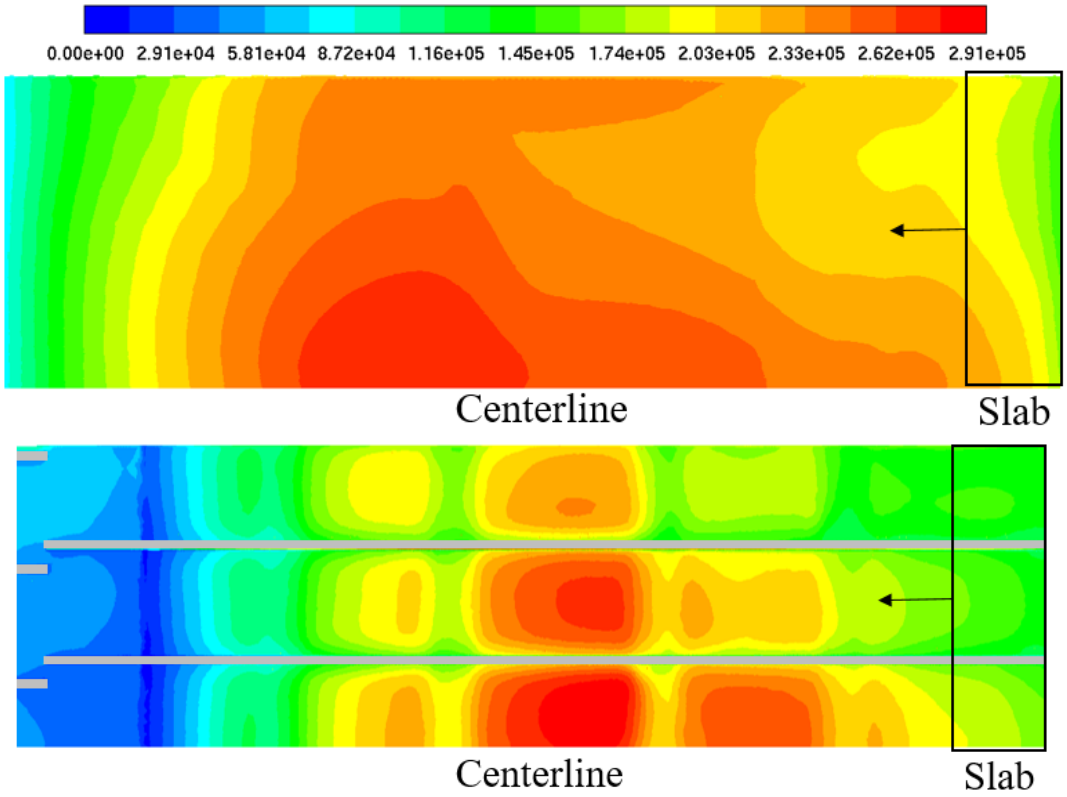

Fig. 5.14 Medium OEC heat fluxes into the slab for top (top) and bottom (bottom) in W/m^2

The overall heat transfer in this zone is displayed in Table 5.2. The total heat transfer has increased by 70% from the baseline case, and the overall heat transfer due to radiation has gone up from 89.3% in the base case to 94.3% in this case. This is mainly from the higher flame temperatures along with the higher concentration of species that participate in radiation in this zone. The amount of heat transfer in total to the slabs has also increased dramatically. This would imply that the slabs can move through the furnace at a much faster rate than the baseline case. Otherwise, the firing rate should be drawn back to avoid overheating the slabs or damaging the furnace.

Table 5.2 Medium OEC heat transfer into the slabs

Zone	Zone Heat Transfer (W)	Radiation Heat Transfer (W)	Radiation HT of Zone	Zone HT of Total
Recuperative	6.35E+06	5.66E+06	89.1%	25.2%
Preheat	1.59E+07	1.50E+07	94.4%	63.1%
Total	3.01E+07	2.84E+07	94.3%	---

The heat transfer into the slab for the oxy-fuel case is shown in Fig. 5.15. The maximum heat transfer in W/m^2 has increased by over 130kW/m^2. The largest heating, similar to the medium oxygen enrichment case, is near the middle of the slab, with a small zone on the edge that also gets a larger amount of the heating comparatively. The bottom preheat zone most definitely has the largest amount of heating near the middle of the slab. Again, these trends are due to the impact of flow interaction between the top and bottom preheat zones on the flame and convection heat transfer near the edges of the slabs. Refer to the previous discussion on the heat transfer into the slab for the medium oxygen enrichment case above.

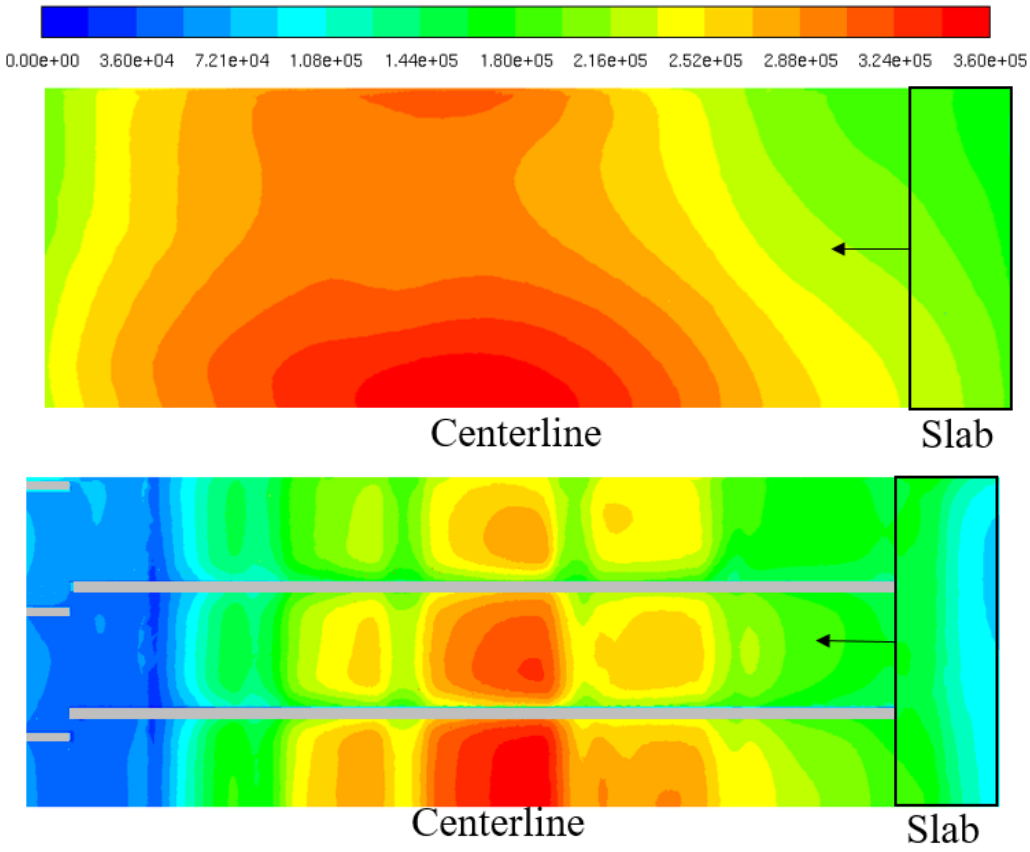

Fig. 5.15 Oxy-fuel heat fluxes into the slab for top (top) and bottom (bottom) in W/m^2

Looking at the overall amount of heating in the preheat zone for the oxy-fuel case, the heat transfer into the slab has increased by 80.8% from the baseline case. The overall amount of heat transfer in this zone compared to later zones is also substantially higher than found in the base case. The percentage of heat from radiation has also increased from the base case of 89.3% to 93.8%, which is curiously lower than that found in the medium oxygen enrichment case. As this is a

percentage of the total heat flux into the slab, it may be due to the enhanced convection from the higher velocity near the slab in the oxy-fuel case over that found in the medium oxygen enrichment case. As such, a relatively larger portion of the heat flux into the slab would then be from convection compared to both the base case and the medium oxygen enrichment case. The overall amount of radiation heat flux into the slab, however, always increases with oxygen enrichment.

Table 5.3 Oxy-fuel heat transfer into the slabs

Zone	Zone Heat Transfer (W)	Radiation Heat Transfer (W)	Radiation HT of Zone	Zone HT of Total
Recuperative	6.93E+06	6.15E+06	88.8%	27.5%
Preheat	1.97E+07	1.85E+07	93.9%	78.1%
Total	3.20E+07	3.00E+07	93.8%	

Of note is that while both cases gave a larger heat transfer into the slabs that the base case, the difference between the medium oxygen enrichment case (46 vol% O_2) and the oxy-fuel case (100 vol% O_2) is only 10.8%. As the cost of oxygen is a very large factor in the usage of oxygen enrichment, this may lead to a medium oxygen enrichment recommendation over a full oxy-fuel implementation.

5.7 Effects on Scale Formation

The scaling parameters are shown in Table 5.4 for medium oxygen enrichment and Table 5.5 for oxy-fuel. Only the recuperative and preheat zones are shown to avoid repetition. The temperatures near the slab for both cases are noticeably larger than those seen by the base case. As expected, the concentrations of oxygen, water vapor, and carbon dioxide have all increased. There is a velocity increase from the base case to the oxy-fuel case, which promotes convective heat transfer. This corroborates earlier analysis. The pressure in the oxy-fuel case is very interesting aa the pressure starts much lower and decreases to a negative value unlike both of the other cases in study here.

Table 5.4 Medium OEC scale formation parameters

Parameters	Recup	PHZ
Temperature (°C)	1029.00	1132.13
Velocity (m/s)	4.511	5.134
O_2 vol%	6.245	7.131
H_2O vol%	21.104	17.912
CO_2 vol%	10.818	9.185
Pressure (Pa)	12.444	3.74871
Density (kg/m^3)	0.26394	0.24514
Viscosity (kg/m-s)	1.72E-05	

Table 5.5 Oxy-fuel scale formation parameters

Parameters	Recup	PHZ
Temperature (°C)	1103.85	1197.95
Velocity (m/s)	5.846	7.212
O_2 vol%	8.015	7.876
H_2O vol%	23.645	19.591
CO_2 vol%	12.123	10.046
Pressure (Pa)	12.1748	-7.22093
Density (kg/m^3)	0.24891	0.23378
Viscosity (kg/m-s)	1.72E-05	

The calculated parabolic and linear rate constants for both oxygen enrichment cases are shown below in Table 5.5. As with the temperature, these rate constants are all larger than their respective counterparts for the baseline case. This is especially true for the linear rate constants in the oxy-fuel case, the largest of the three cases.

Table 5.6 Medium OEC and oxy-fuel kinetic rate constants

Case	Zone	k_p (cm^2/s)	k_l (cm/s)
Medium OEC	Recup.	2.81E-06	7.46E-05
	Preheat	6.64E-06	6.33E-05
Oxy-fuel	Recup.	5.32E-06	1.11E-04
	Preheat	1.07E-05	1.23E-04

All of the scale grown over time for the preheat zone is shown in Fig. 5.16. The baseline case is the ‘coldest’ of the three and with the highest concentration of the non-oxidizing nitrogen. For the same residence time, it makes sense that it would have the least small formation. However, the scale formation is only slightly enhanced for the medium enrichment case. The oxy-fuel case

is noticeably larger than both. With a firing rate drawback or a productivity increase, these values may change and result in less scale formation for oxygen enriched cases.

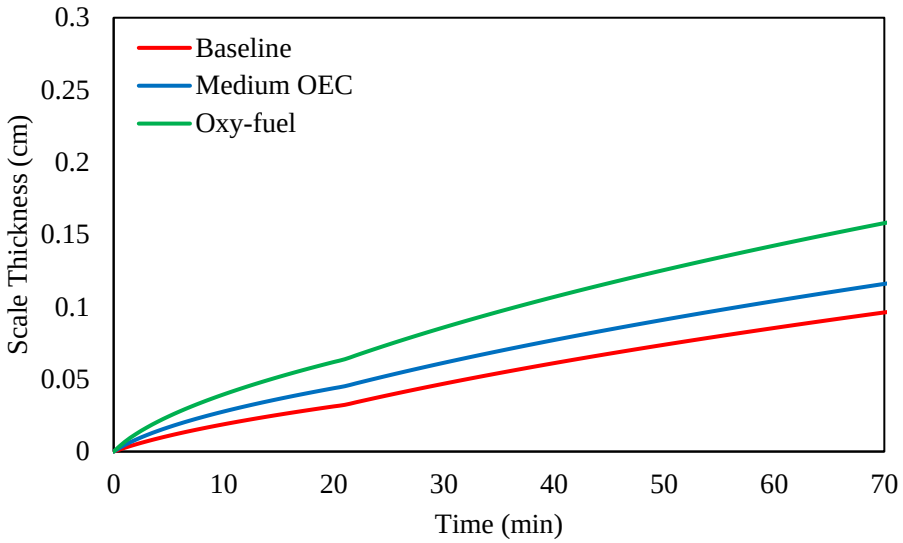

Fig. 5.16 Medium OEC heat fluxes into the slab for top (top) and bottom (bottom) in W/m^2

The final values for medium oxygen enrichment and oxy-fuel for the whole furnace were .24 cm (0.095 in) and 0.28 cm (0.111 in) respectively. These are increases from the base case of 9% and 28% respectively.

6. CONCLUSIONS

6.1 Conclusions

This work has covered the modeling of scale formation as it pertains to reheating furnace environments as well as the modeling of said environment. The scale formation model is able to incorporate into the computational fluid dynamics software ANSYS Fluent to solve a coupled steady-state and transient simulation. It is also generalized for a low-carbon steel product, so it may not be adequate to cover the effects of alloying metals on the oxidation process. The modeling of a baseline reheating furnace case was accomplished and validated against industrial furnace temperature data and data from a thermocoupled slab.

Baseline case results showed the effect of the flow on the flames and overall temperature distribution within the furnace. Centerline recirculation zones were the most developed; these zones slowly changed as they moved away from the center of the furnace. The top and bottom zones were separated by the length of the slab. Between the slab and the furnace side-walls, the top and bottom zonal flow interacted, causing the bottom flames to be pushed inward and causing the top flames to be pulled outward. This then influenced the heat transfer into the slab. Total heat transfer into the slab was around 2.52E+07 W for all zones. 91.5% of the heat transfer was from radiation heat transfer. Over half of this heat transfer occurred in the preheat zone. The baseline case was found to grow 0.22 cm of scale, or 0.087 inches of scale. This measurement, of course, is in thickness. This was found to be around 1.76% of the total slab thickness.

For the oxygen enrichment studies, all parameters in the preheat zone were changed due to the changes in boundary conditions. The maximum preheat zone temperature was higher than the base case for both oxygen enrichment cases, as was the heat transfer into the slab. The flames were also noticeably straighter as the higher velocity jets for each respective case allowed the flames to overcome the pull of the incoming flow from subsequent zones. The heat transfer for the medium oxygen enrichment case in the preheat zone increased by 70.0% from the base case, with the amount from radiative heat transfer going from 89.3% in the base case to 94.3%. For the oxy-fuel case, the heat transfer into the slab increased by 80.8% with 93.8% coming from radiation. The medium oxygen enrichment and oxy-fuel cases had 109% and 128% of the scale thickness found from the base case due to higher scaling parameters.

6.2 Recommendations

Due to the cost of oxygen and the compared benefits of medium oxygen enrichment versus the application of oxy-fuel, the former is recommended for use within industrial reheat furnaces. The oxygen lances between burners elongated the flame shape and allowed for a more uniform radiating surface of hot gases within the flame. The cost in going from medium oxygen enrichment at 46 vol% O_2 to oxy-fuel at 100 vol% O_2 may also be greater than the small increase in heat transfer between the two options. The scale formed during medium oxygen enrichment was much less compared to the oxy-fuel case. Further, to decrease the temperature within the preheat zone to better match the baseline case and to reduce NOx formation, a drawback of the total firing rate in the preheat zone is recommended, which should reduce the scale formation.

REFERENCES

[1] P. Mullinger and B. Jenkins. “Industrial and Process Furnaces: Principles, Design and Operation.” Elsevier via Butterworth-Heinemann (2008) Hungary.

[2] J. G. Lenard. “Primer on Flat Rolling.” Elsevier, 2nd ed. (2014).

[3] W. Weißbach. “Materials Science Structures, Properties, Testing.” 17th ed. (2019) p. 76.

[4] Z. Li, P. V. Barr, and J. K. Brimacombe. “Computer Simulation of the Slab Reheating Furnace.” *Canadian Metallurgical Quarterly*, vol. 27, no. 3 (1988) pp. 187-196.

[5] K. S. Chapman, S. Ramadhyani, and R. Viskanta. “Two-Dimensional Modeling and Parametric Studies of Heat Transfer in a Direct-Fired Furnace with Impinging Jets.” *Combustion Science and Technology,* vol. 97, no. 1-2 (1994) pp. 99-120.

[6] J. G. Kim, K. Y. Huh, and I. T. Kim. “Three-dimensional analysis of the walking-beam-type slab reheating furnace in hot strip mills.” *Numerical Heat Transfer: Part A: Applications,* vol. 38, no. 6 (2000) pp. 589-609.

[7] S. R. Turns. “An Introduction to Combustion: Concepts and Applications.” McGraw-Hill 3rd ed. (2012).

[8] R. Y. Chen and W. Y. D. Yuen. “Developments in high-temperature corrosion and protection of materials: Oxide scales on hot-rolled steel strips.” (ed. W. Gao and Z. Li), Cambridge: Woodhead Publishing Ltd. (2008) pp. 192-252.

[9] J. M. Casal, J. Porteiro, J. L. Miguez, and A. Vazquez. “New methodology for CFD three-dimensional simulation of a walking beam type reheating furnace in steady state.” *Applied Thermal Engineering*, vol. 86 (2015) pp. 69-80.

[10] C. E. Baukal, Jr. “Oxygen-Enhanced Combustion.” CRC Press 2nd ed. (2013).

[11] S. V. Patankar. “Numerical Heat Transfer and Fluid Flow.” CRC Press 1st ed. (1980).

[12] “Recent trends in the cost of computing.” *AI IMPACTS,* (2017) Retrieved from: https://aiimpacts.org/recent-trend-in-the-cost-of-computing/

[13] H. C. Hottel and A. F. Sarofim. “Models of Radiative Transfer in Furnaces.” *Journal of Engineering Physics*, vol. 19, no. 3 (1970) pp. 1102-1114.

[14] Y. Yang, J. Kroeze, and M. A. Reuter. “Simulation of slab movement and transient heating in a continuous steel reheat furnace.” *Progress in Computational Fluid Dynamics an International Journal*, vol. 4, no. 1 (2004) pp. 46-58.

[15] M. Huang, C. Hsieh, S. Lee, and C. Wang. “A Coupled Numerical Study of Slab Temperature and Gas Temperature in the Walking-Beam-Type Slab Reheating Furnace.” *Numerical Heat Transfer, Part A: Applications*, vol. 54, no. 6 (2008) pp. 625-646.

[16] “Overset Mesh.” *ANSYS*. (2017). Retrieved from: https://www.ansys.com/products/fluids/ansys-fluent/overset-mesh

[17] R. Prieler, B. Mayr, M. Demuth, and D. Spoljaric. “Application of the steady flamelet model on a lab-scale and an industrial furnace for different oxygen concentrations.” *Energy*, vol. 91 (2015) pp. 451-464.

[18] G. Bisio, A. Bosio, And G. Rubatto. “Thermodynamics Applied to Oxygen Enrichment of Combustion Air.” *Energy Conversion and Management*, vol. 43 (2003) pp. 2589-2600.

[19] A. Atreya. “Highly Preheated Combustion Air System With/Without Oxygen Enrichment for Metal Processing Furnaces.” *Final Progress Report For DE-FC36-02ID14348* (2007).

[20] C. Lowe, N. Brancaccio, J. Jamaluddin, J. A. Erazo, Jr., and C. E. Baukal, Jr. “Technology Assessment of Oxy-Firing of Process Heater Burners.” *Energy Procedia*, vol. 37 (2013) pp. 7793-7801.

[21] C. Sobotka, H. Antrekowitsch, and H. Schnideritsch. “The Influence of Oxygen-Enriched Burner Systems on The Scale Formation Of Steel Alloys During Heating Processes.” *AISTech 2014 Proceedings*, vol. 1 (2014) pp. 3115-3131.

[22] H. J. Karimi and M. H. Saidi. “Heat Transfer and Energy Analysis of a Pusher Type Reheating Furnace Using Oxygen Enhanced Air for Combustion.” *Journal of Iron and Steel Research International*, vol. 17, no. 4 (2010) pp. 12-17.

[23] L. Alvarez, C. Yin, J. Riaza, C. Pevida, J. J. Pis, And F. Rubiera. “Oxy-Coal Combustion in an Entrained Flow Reactor: Application of Specific Char and Volatile Combustion And Radiation Models For Oxy-Firing Conditions.” *Energy*, vol. 62 (2013) pp. 255-268.

[24] B. Mayr, R. Prieler, M. Demuth, L. Moderer, and C. Hochenauer. “CFD modeling and performance increase of a pusher type reheating furnace using oxy-fuel burners.” *Energy Procedia*, vol. 120 (2017) pp. 462-468.

[25] J. H. Jang, D. E. Lee, M. Y. Kim, and H. G. Kim. “Investigation of the slab heating characteristics in a reheating furnace with the formation and growth of scale on the slab surface.” *International Journal of Heat and Mass Transfer*, vol. 53 (2010) pp. 4326-4332.

[26] R. Y. Chen and W. Y. D. Yuen. “Review of the high-temperature oxidation of iron and carbon steels in air or oxygen.” *Oxidation of Metals*, vol. 59, no. 5-6 (2003) pp. 433-468.

[27] C. Schluckner, C. Gaber, M. Demuth, S. Forstinger, R. Prieler, and C. Hochenauer. “CFD-model to predict the local and time-dependent scale formation of steels in air- and oxygen enriched combustion atmospheres.” *Applied Thermal Engineering*, vol. 143 (2018) pp. 822-835.

[28] M. Landfahrer, C. Schluckner, R. Prieler, H. Gerhardter, T. Zmek, J. Klarner, and C. Hochenauer. “Development and application of a numerically efficient model describing a rotary hearth furnace using CFD.” *Energy*, vol. 180 (2019) pp. 79-89.

[29] “Tour of ArcelorMittal 80” Hot Strip Mill.” *Personal Tour*, (October 18, 2019).

[30] V. H. J. Lee, B. Gleeson, and D. J. Young. “Scaling of Carbon Steel in Simulated Reheat Furnace Atmospheres.” *Oxidation of Metals*, vol. 63, no. 1-2 (2005) pp. 15-31.

[31] D. J. Young, “High Temperature Oxidation and Corrosion of Metals.” Oxford: Elsevier Science, 2nd ed. (2016).

[32] O. Kubaschewski and C. B. Alcock, “Metallurgical Thermochemistry.” Oxford, New York: Pergamon Press, 5th ed. (1979).

[33] C. Wagner. "Beitrag zur theorie des anlaufvorgangs." *Zeitschrift für physikalische Chemie*, vol. 21, no. 1 (1933) pp. 25-41.

[34] K. Fueki and J. B. Wagner. "Studies of the Oxidation of Nickel in the Temperature Range of 900 to 1400 C." *Journal of the Electrochemical Society*, vol. 112, no. 4 (1965) pp. 384-388.

[35] P. Kofstad. "High-temperature oxidation of metals." New York, John Wiley and Sons, Inc. (1966).

[36] H. T. Abuluwefa, R. I. L. Guthrie, and F. Ajersch. “Oxidation of Low Carbon Steel in Multicomponent Gases: Part I. Reaction Mechanisms during Isothermal Oxidation.” *Metta. and Mats. Trans. A*, vol. 28, no. 8 (1997) pp. 1633-1641.

[37] H. T. Abuluwefa, R. I. L. Guthrie, and F. Ajersch. “Oxidation of Low Carbon Steel in Multicomponent Gases : Part II. Reaction Mechanisms during Reheating.” *Metall. Mater. Trans. A,* vol. 28, no. 8 (1997) pp. 1643–1651.

[38] R. E. Bedworth and N. B. Pilling. "The oxidation of metals at high temperatures." *J Inst Met*, vol. 29, no. 3 (1923) pp. 529-582.

[39] W. W. Smeltzer and D. J. Young. "Oxidation properties of transition metals." *Progress in Solid State Chemistry*, vol. 10 (1975) pp. 17-54.

[40] G. Tammann. “Über Anlauffarben von Metallen.” *Z. anorg. Allgem. Chem.*, vol. 111 (1920) pp. 78-89.

[41] Personal Communications with Judy Li, ArcelorMittal. (Nov. 15 2018).

[42] J. Païdassi. “The kinetics of the air oxidation of iron in the range 700-1250°C.” *Acta. Metall.*, vol. 6, no. 3 (1985) pp. 184-194.

[43] J. Akiyama, H. Ohta, R. Takahashi, T. Waseda, and J. Yagi. “Measurement and Modeling of Thermal Conductivity for Dense Iron Oxide and Porous Iron Ore Agglomerates in Stepwise Reduction.” *ISIJ Int.*, vol. 32, no. 7 (1992) pp. 829-837.

[44] W. W. Smeltzer. “The kinetics of wüstite scale formation on iron.” *Acta. Metall*., vol. 8, no. 6 (1960) pp. 377-383.

[45] H. Abuluwefa, R. I. L. Guthrie, and F. Ajersch. “The Effect of Oxygen Concentration on the Oxidation of Low-Carbon Steel in the Temperature Range 1000 to 1250°C.” *Oxid. Metals*, vol. 46, no. 5-6 (1996) pp. 423-440.

[46] K. Sachs and C. W. Tuck. “Scale Growth during Re-heating Cycles.” *Werks. Korros.*, vol. 21, no. 11 (1970) pp. 945-954.

[47] H. Selenz and F. Oeters. “A contribution to the scaling of steel in technical flue gases.” *Metallurgie*, vol. 55, no. 5 (1984) pp. 201-208.

[48] L. Himmel, R. F. Mehl, and C. E. Birchenall. "Self-diffusion of iron in iron oxides and the Wagner theory of oxidation." *JOM*, vol. 5, no. 6 (1953) pp. 827-843.

[49] J. Deich and F. Oeters. “Zur Verzunderung von Weichstahl in Stickstoff-Kohlendioxid-Gemischen mit geringen Sauerstoffzusätzen.” *Materials and Corrosion*, vol. 24, no. 5 (1973) pp. 365-371.

[50] L. S. Darken and R. W. Gurry. “The System Iron-Oxygen. I. The Wüstite Field and Related Equilibria.” *J. Am. Chem. Soc*., vol. 67, no. 8 (1945) pp. 1398-1412.

[51] B. Webler. “A Study of the Processes During High Temperature Oxidation That Control Surface Hot Shortness in Copper-Containing Low Carbon Steels.” *Doctoral Thesis*. Pittsburgh, Pennsylvania: Carnegie Mellon University (2008). Available: ProQuest.

[52] H. F. Marston, P. H. Bolt, G. Leprince, M. Roder, R. Klima, J. Niska, and M. Jarl. "Challenges in the modeling of scale formation and decarburisation of high carbon, special and general steels." *Ironmaking & steelmaking,* vol. 31, no. 1 (2004) pp. 57-65.

[53] M. Schütze and D. R. Holmes (Ed.), "Protective Oxide Scales and Their Breakdown, Series on Corrosion." Chichester, England: Institute of Corrosion and Wiley (1997).

[54] C. Upthegrove. "Scaling of Steel at Heat-Treating Temperatures." Engineering Research Bulletin, No. 25, Department of Engineering Research, University of Michigan (George Banta Publ., Menasha, WI, 1933).

[55] P. Tomaszewicz and G. R. Wallwork. "Iron-Aluminum alloys: a review of their oxidation behavior." *Rev. High-Temp. Mater,* vol. 4, no. 1 (1978) pp. 75-105.

[56] A. Rahmel. "Beitrag zur Frage des Zunderverhaltens von Kesselbaustählen." *Mitt. VGB,* vol. 74 (1961) pp. 319-332.

[57] D. Caplan and G. I. Sproule. "Effect of oxide grain structure on the high-temperature oxidation of Cr." *Oxidation of Metals,* vol. 9, no. 5 (1975) pp. 459-472.

[58] F. A. Golightly, F. H. Stott, and G. C. Wood. "The influence of yttrium additions on the oxide-scale adhesion to an iron-chromium-aluminum alloy." *Oxidation of Metals,* vol. 10, no. 3 (1976) pp. 163-187.

[59] F. H. Stott, and G. C. Wood. "The influence of oxides on the friction and wear of alloys." *Tribology International,* vol. 11, no. 4 (1978) pp. 211-218.

[60] W. Schendler. "Heat-resisting steels: Development trends in steels and their practical importance." VDI-Gesellschaft Werkstofftechnik (1981).

[61] S. Chevalier. "What did we learn on the reactive element effect in chromia scale since Pfeil's patent?" *Materials and Corrosion,* vol. 65, no. 2 (2014) pp. 109-115.

[62] Y. Tang, J. Laine, T. Fabritius, and J. Harkki. "The Modeling of the Gas Flow and Its Influence on the Scale Accumulation in the Steel Slab Pusher-type Reheating Furnace." *ISIJ International,* vol. 43, no. 9 (2003) pp. 1333-1341.

[63] X. Liu, G. Tang, A. Silaen, J. Cox, K. Johnson, and C. Zhou. "Investigation of Operational Effects on Slab Heating Characteristics in a Pusher-Type Reheat Furnace with Continuous Slab Motion." *ASME 2017 Heat Transfer Summer Conference* (2017).

[64] M. Keating. "Accelerating CFD Solutions." *ANSYS: Tips and Tricks,* vol. 5, no. 1 (2011) pp. 48-49.

[65] W. P. Jones and B. E. Launder. “The Prediction of Laminarization with a Two-Equation Model of Turbulence.” *International Journal of Heat and Mass Transfer*, vol. 15 (1972) pp. 301-314.

[66] T. Shih, W. W. Liou, A. Shabbir, Z. Yang, and J. Zhu. “A New k-ϵ Eddy Viscosity Model for High Reynolds Number Turbulent Flows.” *Computers & Fluids*, vol. 24, no. 3 (1995) pp. 227-238.

[67] ANSYS® Fluent, Release 18.2, Help System, Theory Guide, ANSYS, Inc.

[68] W. W. Kim and S. Menon. “Computations of Complex Turbulent Flows Using the Commercial Code ANSYS FLUENT.” *Technical Report AIAA-97-0210, American Institute of Aeronautics and Astronautics*, 35th Aerospace Sciences Meeting, Reno, NV, January 1997.

[69] B. E. Launder and D. B. Spalding. “The Numerical Computation of Turbulent Flows.” *Computer Methods in Applied Mechanics and Engineering*, vol. 3 (1974) pp. 269-289.

[70] M. F. Modest. “Radiative Heat Transfer.” Academic Press, 3rd ed. (2013).

[71] W. A. Fiveland. “Three-dimensional radiative heat-transfer solutions by the discrete-ordinates method.” *Journal of Thermophysics and Heat Transfer*, vol. 2, no. 4 (1988) pp. 309-316.

[72] J. S. Truelove. “Discrete-ordinate solutions of the radiation transport equation.” *ASME Journal of Heat Transfer*, vol. 109, no. 4 (1987) pp. 1048-1051.

[73] W. A. Fiveland and A. S. Jamaluddin. “Three-Dimensional Spectral Radiative Heat Transfer Solutions by the Discrete Ordinates Method.” *J. Thermophysics*, vol. 5, no. 3 (1991) pp. 43-48, 1989.

[74] E. H. Chui and G. D. Raithby. “Computation of Radiant Heat Transfer on a Non-Orthogonal Mesh Using the Finite-Volume Method.” *Numerical Heat Transfer, Part B*, vol. 23 (1993) pp. 269-288.

[75] H. C. Hottel and A. F. Sarofim. “Models of Radiative Transfer in Furnaces.” *Journal of Engineering Physics*, vol. 19, no. 3 (1970) pp. 1102-1114.

[76] A. Coppalle and P. Vervisch. “The Total Emissivities of High-Temperature Flames.” *Combustion and Flames*, vol. 49 (1983) pp. 101-108.

[77] T. F. Smith, Z. F. Shen, and J. N. Friedman. “Evaluation of Coefficients for the Weighted Sum of Gray Gases Model.” *J. Heat Transfer*, vol. 104, no. 4 (1982) pp. 602-608.

[78] W. P. Jones and J. H. Whitelaw. “Calculation Methods for Reacting Turbulent Flows: A Review.” *Combustion and Flame*, vol. 48 (1982) pp. 1-26.

[79] N. Peters. “Laminar diffusion flamelet models in non-premixed turbulent combustion.” *Progress in Energy and Combustion Science*, vol. 10, no. 3 (1984) pp. 319-339.

[80] "Chemical-Kinetic Mechanisms for Combustion Applications." *San Diego Mechanism web page*, Mechanical and Aerospace Engineering (Combustion Research), University of California at San Diego (http://combustion.ucsd.edu).

[81] A. Sayre, N. Lallement, J. Dugu, and R.Weber “Scaling Characteristics of Aerodynamics and Low-NOx Properties of Industrial Natural Gas Burners.” *The SCALING 400 Study, Part IV: The 300 KW BERL Test Results, IFRF Doc No F40/y/11*, International Flame Research Foundation, The Netherlands.

[82] G. P. Smith, D. M. Golden, M. Frenklach, N. W. Moriarty, B. Eiteneer, M. Goldenberg, C. T. Bowman, R. K. Hanson, S. Song, W. C. Gardiner, Jr., V. V. Lissianski, and Z. Qin http://www.me.berkeley.edu/gri_mech/. Accessed March 2019.

[83] C. K. Westbrook and F. L. Dryer. “Simplified Reaction Mechanisms for the Oxidation of Hydrocarbon Fuels in Flames.” *Combustion Science and Technology*, vol. 27 (1981): pp. 31-43.